The Dissertation Committee for Richard Maxwell Naething
certifies that this is the approved version of the following dissertation:

Enhanced Inverse Synthetic Aperture Radar

Committee:

Hao Ling, Supervisor

Sean Buckley, Supervisor

Alan Bovik

Armin Doerry

Brian Evans

Joydeep Ghosh

Enhanced Inverse Synthetic Aperture Radar

by

Richard Maxwell Naething, B.S., M.S.E.

DISSERTATION

Presented to the Faculty of the Graduate School of

The University of Texas at Austin

in Partial Fulfillment

of the Requirements

for the Degree of

DOCTOR OF PHILOSOPHY

THE UNIVERSITY OF TEXAS AT AUSTIN

December 2010

Dedicated to Windsor

Acknowledgments

First I would like to acknowledge my family for their support over my long academic career. My parents, Bob and Chris Naething, not only emphasized the value of education during my childhood, but encouraged my pursuit of science and engineering through a variety of hobbies.

My aunt Patty Merrill and my uncle Rick Merrill were my relatives living the closest during most of my graduate studies. They provided a place to visit on weekends and holidays, and helped me with finding and furnishing several of my apartments.

My aunt Lori Parrott and my uncle Rick Ormesher have housed me for twelve summers in Albuquerque while I interned at Sandia National Laboratories. During the summer my cousin Ryen put up with being displaced from her bedroom and my cousin Eryn with having to share her room with her sister. I am grateful to Rick for teaching me how to fly fish, but even more grateful for him answering many questions about signal processing during the past few years.

I owe a large debt of gratitude to all of the researchers who have mentored me over the past decade at Sandia National Labs. Garth Reese, Dan Seegalman, and Manoj Bhardwaj for many years when I worked with finite elements; and Dale Dubbert and Doug Bickel more recently as my research

interests shifted into radar and communications systems. Garth told me when I first started working at Sandia as a high school student that it was important to learn something new everyday, advice I have tried hard to follow.

I greatly appreciate the supervision of my adviser Sean Buckley over the past four plus years of my graduate studies. I also want to thank the faculty and staff of both the Electrical and Computer Engineering and Aerospace department for their dedication to the education of graduate students. I also would like to thank my committee, particularly Armin Doerry who agreed to fly to Austin twice to serve a committee member.

There are many graduate students that I have had the privilege to know while at UT Austin. These include but are not limited to Sri Priya Ponnapalli, Prahlad Enuganti, and Chase Krumpelman in the Electrical and Computer Engineering department; James Luck, Dochul Yang, and Vikas Gudipati from my research lab; and Jack Goetz, Jessica Williams, and Cinnamon Wright from Aerospace engineering. Priya is the first friend I made at UT Austin. We started our graduate careers at the same time, shared almost all our classes, and pulled numerous all nighters in the ECE building together trying to finish homework and projects. A few years into our graduate studies she dragged me along to a free dinner put on by the graduate student council. Several years later I found myself the president of the graduate student council. That *free* dinner has cost me dearly through countless hours of meetings and event planning.

My priest, John Newton, and the students at the Episcopal Student

Center at All Saints Church have been a large part of my life during my time in Austin. I greatly value their friendship and support. This is where I met my fiancé, Windsor Standish, whose support has been instrumental as I finalized my graduate studies. We are getting married a week after I defend.

This work was supported by the Laboratory Directed Research and Development program at Sandia National Laboratories. Sandia is a multiprogram laboratory operated by Sandia Corporation, a Lockheed Martin Company, for the United States Department of Energy's National Nuclear Security Administration under Contract DE-AC04-94AL85000. Portions of this work was supported through Sandia National Laboratories and the UT Office of Graduate Studies through the National Physical Science Consortium fellowship program.

Enhanced Inverse Synthetic Aperture Radar

Publication No. _____

Richard Maxwell Naething, Ph.D.
The University of Texas at Austin, 2010

Supervisors: Hao Ling
Sean Buckley

Synthetic aperture radar (SAR) is an imaging technique based on the radio reflectivity of the target being imaged. SAR instruments offer many advantages over optical imaging due to the ability to form coherent images in inclement weather, at night, and through ground cover. High resolution is achieved in azimuth through a synthesized aperture much larger than the physical antenna of the imaging device. Consequently, proper focusing requires accurate information about the relative motion between the antenna phase center and the scene. Any unknown target velocity, acceleration, rotation, or vibration will introduce errors in the image.

This work addresses a novel method of focusing a moving target in a SAR image through the estimation of various motion parameters. The target azimuth position is determined through monopulse radar, at which point range velocity and acceleration are estimated across a series of overlapping sub-apertures. Cross-range velocity is then estimated through a search to optimize

an image quality metric such as entropy or contrast. A final focused image is then generated based on this velocity vector. Methods of extending this work for a single phase center system are considered.

This technique is demonstrated with real radar data from an experimental system, and the performance of this technique is compared both subjectively and with a variety of image metrics to the MITRE keystone technique. Finally, extensions to this current line of research are considered.

Table of Contents

Acknowledgments **v**

Abstract **viii**

List of Tables **xiii**

List of Figures **xiv**

Chapter 1. Introduction **1**

1.1 Related work 2

1.2 Thesis Outline and Contributions 6

1.2.1 Chapter 2: Development of a mathematical framework for moving targets in SAR 6

1.2.2 Chapter 3: A novel method to focus, locate, and estimate velocity for a moving target 7

1.2.3 Chapter 4: Detection of a moving target using a single phase center 7

1.2.4 Chapter 5: Knowledge-based focusing of a moving target 8

1.2.5 Chapter 6: Summary and future work 8

Chapter 2. Development of a mathematical framework for moving targets in SAR **9**

2.1 Radar Targets 10

2.2 SAR Fundamentals 12

2.3 Definition of a SAR Geometry 14

2.3.1 Approximation of range to target 15

2.3.2 Approximation of target phase 16

2.4 The effects of motion on SAR images 16

2.4.1 Range Velocity Phase 18

2.4.2 Cross-range velocity phase 20

2.4.3 Range acceleration phase 21
2.4.4 Cross-range acceleration and other motion errors 22
2.5 The MITRE keystone technique 22
2.5.1 Range velocity phase 25
2.5.2 Cross-range velocity phase 26
2.5.3 Range acceleration phase 27
2.6 Conclusion 27

Chapter 3. A novel method to focus, locate, and estimate velocity for a moving target 32
3.1 Estimating true azimuth position through monopulse 34
3.2 Determining range velocity and acceleration through target shift 35
3.3 Azimuth velocity via search 38
3.4 Results 40
3.5 Conclusion 44

Chapter 4. Detection of a moving target using a single phase center 54
4.1 Background and Related Work 55
4.2 Proposed method 58
4.2.1 Sharpness Metrics 61
4.3 Simulation 63
4.3.1 Performance improvement of the modified technique . . 63
4.3.2 Minimum detectable azimuth velocity 65
4.3.3 Multiple target detection example 73
4.4 Conclusion 86

Chapter 5. Knowledge-based focusing of a moving target 87
5.1 Geometric dilution of precision 88
5.2 Knowledge of road systems 93
5.3 Target knowledge 95
5.4 A fully processed target 97
5.5 Conclusion 101

Chapter 6. Summary and Future Work **107**

Appendices **110**

Appendix A. Return from a Point Target **111**

Bibliography **116**

Vita **124**

List of Tables

3.1 Estimated target velocities 45
3.2 Image Metrics for Moving Targets 46

4.1 Radar parameters: synthetic data 64

List of Figures

2.1 A typical spotlight mode SAR image collect 13

2.2 Vector definition of target geometry 14

2.3 A full polar formated SAR scene with a simulated moving point target. The target is initially located at the origin with a range velocity of 5 m/s. 29

2.4 An endo-clutter SAR scene with a simulated moving point target. The target is initially located 20m in cross-range (azimuth) from the origin with a cross-range velocity of 5 m/s. 30

2.5 An endo-clutter SAR scene with a simulated moving point target. The target is initially located 40m in cross-range (azimuth) from the origin with a range acceleration of 0.653 m/s^2. 30

2.6 An endo-clutter SAR scene with a simulated moving point target. The target is initially located at the origin with a cross-range acceleration of 1 m/s^2. 31

2.7 An endo-clutter SAR scene with a simulated moving point target. The target is initially located at the origin with a range jerk of 0.0333 m/s^3. 31

3.1 Range velocity estimates for sub-apertures for a water truck moving at 8.9m/s (20 mi/h) 37

3.2 A search over azimuth velocity for maximum contrast using the C_2 (standard deviation over the mean of intensity) image quality metric 39

3.3 An unfocused pickup truck moving at 2.2 m/s (5mi/h). The image is displayed as the square root of magnitude. 47

3.4 A pickup truck moving at 2.2 m/s (5mi/h) focused with the MITRE keystone technique. The images is displayed as the square root of magnitude. 48

3.5 A pickup truck moving at 2.2 m/s (5mi/h) focused and located with the new proposed method. The images is displayed as the square root of magnitude. 48

3.6 An unfocused water truck moving at 2.2 m/s (5mi/h). The image is displayed as the square root of magnitude. 49

3.7 A water truck moving at 2.2 m/s (5mi/h) focused with the MITRE keystone technique. The images is displayed as the square root of magnitude. 49
3.8 A water truck moving at 2.2 m/s (5mi/h) focused and located with the new proposed method. The images is displayed as the square root of magnitude. 50
3.9 An unfocused pickup truck moving at 8.9 m/s (20mi/h). The image is displayed as the square root of magnitude. 50
3.10 A pickup truck moving at 8.9 m/s (20mi/h) focused with the MITRE keystone technique. The images is displayed as the square root of magnitude. 51
3.11 A pickup truck moving at 8.9 m/s (20mi/h) focused and located with the new proposed method. The images is displayed as the square root of magnitude. 51
3.12 An unfocused water truck moving at 8.9 m/s (20mi/h). The image is displayed as the square root of magnitude. 52
3.13 A water truck moving at 8.9 m/s (20mi/h) focused with the MITRE keystone technique. The images is displayed as the square root of magnitude. 52
3.14 A water truck moving at 8.9 m/s (20mi/h) focused and located with the new proposed method. The images is displayed as the square root of magnitude. 53

4.1 Segmented patches of a SAR image. 62
4.2 The f_4 sharpness metric for an unalised point target at the scene center with various simulated clutter levels versus azimuth velocity (-5 m/s to 5 m/s). 67
4.3 The f_4 sharpness metric for an unalised point target at the scene center with various simulated clutter levels versus azimuth velocity (-30 m/s to 30 m/s). 68
4.4 The f_4 sharpness metric for an aliased point target at the scene center with various simulated clutter levels versus azimuth velocity (-5 m/s to 5 m/s). 69
4.5 The f_4 sharpness metric for an aliased point target at the scene center with various simulated clutter levels versus azimuth velocity (-30 m/s to 30 m/s). 70
4.6 The f_4 sharpness metric for a twice aliased point target at the scene center with various simulated clutter levels versus azimuth velocity (-5 m/s to 5 m/s). 71

4.7 The f_4 sharpness metric for a twice aliased point target at the scene center with various simulated clutter levels versus azimuth velocity (-30 m/s to 30 m/s). 72
4.8 This diagram shows the position and velocities for point targets used in the multiple target detection simulation. Targets 1–3 are endo-clutter targets, while the parameters for target 4 were selected to cause the target energy to shift into the exo-clutter region. 74
4.9 The full SAR scene focused the MITRE keystone method using a fold factor of -2. The image is displayed as the square root of magnitude. 75
4.10 The endo-clutter SAR scene focused the MITRE keystone method using a fold factor of -2. The image is displayed as the square root of magnitude. 76
4.11 Detection results for endo-clutter targets using a fold factor of -2. 76
4.12 The full SAR scene focused the MITRE keystone method using a fold factor of -1. The image is displayed as the square root of magnitude. 77
4.13 The endo-clutter SAR scene focused the MITRE keystone method using a fold factor of -1. The image is displayed as the square root of magnitude. 78
4.14 Detection results for endo-clutter targets using a fold factor of -1. 78
4.15 The full SAR scene focused the MITRE keystone method. The image is displayed as the square root of magnitude. 79
4.16 The endo-clutter SAR scene focused the MITRE keystone method. The image is displayed as the square root of magnitude. 80
4.17 Detection results for endo-clutter targets. 80
4.18 The full SAR scene focused the MITRE keystone method using a fold factor of 1. The image is displayed as the square root of magnitude. 81
4.19 The endo-clutter SAR scene focused the MITRE keystone method using a fold factor of 1. The image is displayed as the square root of magnitude. 82
4.20 Detection results for endo-clutter targets using a fold factor of 1. 82
4.21 The full SAR scene focused the MITRE keystone method using a fold factor of 2. The image is displayed as the square root of magnitude. 83
4.22 The endo-clutter SAR scene focused the MITRE keystone method using a fold factor of 2. The image is displayed as the square root of magnitude. 84

4.23 Detection results for endo-clutter targets using a fold factor of 2. 84
4.24 A detected moving target (target 1) located 40m in range from the scene center moving 1 m/s in azimuth. 85
4.25 A detected moving target (target 2) located 20m in range from the scene center moving at -17 m/s in range and -2 m/s in azimuth. 85
4.26 A detected moving target (target 3) located -20m in range from the scene center moving at 35 m/s in range and 4 m/s in azimuth. 85
4.27 A detected moving target (target 4) located -40m in range from the scene center moving at 5 m/s in range and 1 m/s in azimuth. 85

5.1 The position uncertainty of a target being positioned with two sensors depends not only on the error of the sensors but also on the geometry. If two ranging sensors are orthogonal there is a low position uncertainty, but as they move further away from being orthogonal the uncertainty increases. Here an example of this effect is seen which is known as *geometric dilution of precision*. 90
5.2 This figure shows typical lines of constant range and constant Doppler from a antenna phase center mounted on an aircraft. The lines of constant range and constant Doppler are orthogonal at at squint angle of 90° (broadside), but parallel at 0°. 91
5.3 Typical fields of regard for SAR imaging and GTMI modes on an aircraft mounted SAR sensor. While GMTI modes can be operated at any squint angle, SAR operation typically requires a squint angle between 45° and 135° 92
5.4 Probability density function of a moving target with a single radar phase center - azimuth position is unknown as the target range velocity has caused a shift in the azimuth position of the target energy. 94
5.5 An example of a probability density function from a road positioned along azimuth. This road is known as example road one. The probability is characterized by a uniform distribution as the target center is assumed to be anywhere within two lanes of traffic. 95
5.6 An example of a probability density function from a road that runs at thirty degrees from the flight path of the radar. This road is known as example road two. The probability is characterized by a uniform distribution as the target center is assumed to be anywhere within two lanes of traffic. 96
5.7 A probability density function of the position of a moving target obtained by direct sensing with a radar with *a priori* knowledge that the target is on the example road one. 97

5.8 A probability density function of the position of a moving target obtained by direct sensing with a radar with *a priori* knowledge that the target is on the example road two. 98

5.9 The frequency of micro-Doppler is dependent on vehicle velocity. 99

5.10 There are two sets of micro-Doppler from the truck that appear to correspond to the two axles and sets of wheels. This can be used to determine vehicle orientation. 100

5.11 The full polar formatted SAR scene. The moving target is aliased and not visible above the clutter. The image is displayed as the square root of magnitude. 102

5.12 The endo-clutter region of the polar formatted SAR scene. The moving target is aliased and not visible above the clutter. The image is displayed as the square root of magnitude. 103

5.13 Detection results showing the detected endo-clutter target. . . 103

5.14 A detected moving target located 24m in range from the scene center moving at 17 m/s in range and -1 m/s in azimuth with -0.05 m/s^2 range acceleration. 104

5.15 The full polar formatted SAR scene. The moving target is focused, however the clutter is now aliased. The image is displayed as the square root of magnitude. 105

5.16 The endo-clutter region of the polar formatted SAR scene. The moving target is focused, however the clutter is now aliased. The image is displayed as the square root of magnitude. 106

Chapter 1

Introduction

SAR imaging technology has many advantages over conventional optical imaging. However, SAR imaging techniques rely on accurate information about the relative motion between the sensor and the object being imaged. SAR imaging techniques perform poorly in the presence of moving targets as the relative motion between the sensor and target is unknown.

Not all radar techniques share this shortfall. Research in the monitoring of enemy ground force movement through ground moving target indicator (GMTI) radar has been ongoing since at least as early as 1958 (i.e. Project Peek [19]). This research continues through such programs as the Joint Surveillance and Target Attack System (JointSTARS) [16] and General Atomic's Lynx radar (designed by Sandia National Labs) [48]. GMTI systems employ automated algorithms that can determine a ground moving target's location, velocity, and, through radar cross section (RCS), target type. Many radars offer joint SAR and GMTI modes, and can overlay target information on a high resolution SAR image through the use of interleaved SAR and GMTI collections. However, traditional GMTI lacks the ability to provide a focused image of a moving target.

An area of active interest is the development of algorithms that can detect moving targets, extract target motion information, and focus and locate a target in a high resolution image without a priori knowledge of target motion (for instance, without the aid of a separate GMTI mode). This is typically referred to as inverse SAR or SAR-GMTI. A successful SAR-GMTI algorithm would have several benefits over interleaved SAR and GMTI collections - it would provide a focused image as well as a target velocity vector, and would simplify radar design and operation by allowing one mode of operation.

This research aims to develop enhanced ISAR moving target algorithms that can focus and locate one or more moving targets over a stationary background.

1.1 Related work

The effects of target motion on SAR imagery, along with two methods to detect moving targets, were first discussed by Raney [35]. There are a number of techniques in the literature that attempt to detect, focus, or locate moving targets.

Werness *et al.* [50, 51] describes a method for focusing moving targets in SAR images given the presence of a suitable number of prominent points. Similar prominent point processing methods had previously been applied to ISAR images [43]. By tracking these points across the aperture of the SAR collection, estimates of the various error-movements of the target (including translational, rotational) can be generated. The prominent points are tracked

across an aperture in the range-compressed domain. This is a multiple stage algorithm: in the first stage the first prominent point is used to estimate translational motion. A correction is applied to the image, and the second prominent point is used to estimate any non-uniform rotation of the target. Finally, a third prominent point is used to estimate the rotational scale factor.

While this approach has admirable results for simulated multi-point targets, there are several clear limitations. The primary limitation is its dependence on prominent points. These prominent points have to be separable from other prominent points, other energy returned from the target, and background clutter across the entire image. Wernes *et al.* outline a method of space-invariant pre-focusing that enhances the signal-to-background ratio. As the tracks of prominent points will cross in even simple target examples, it is necessary to have a human operator separate out the points using interactive graphics routines.

A second class of techniques is based upon joint time-frequency transforms. In traditional synthetic aperture radar imaging, the phase history collected from the target returns, although indexed in slow and fast time, are simply samples of the target's spatial reflectivity in the frequency domain. The target is localized in the time (spatial) domain, and spread out in the frequency domain. In moving targets this is no longer true – targets are not localized in the spatial domain but rather have energy that is spread out in both the spatial and frequency domains.

In recent years a number of joint time–frequency distributions have

been developed in an attempt to improve the analysis of signals that, like moving targets in SAR images, have energy that is not localized in either time or frequency but may be localized in a combination of both [10, 24]. These include the Short Time Fourier Transform (STFT), the Gabor Transform, and the Wigner-Ville Transform/Distribution (WVD). The STFT and the Gabor transform (which is essentially a windowed STFT) are limited by the uncertainty principle, which states that a signal cannot be localized in both time and frequency simultaneously. The WVD transform provides optimal signal localization but is bilinear – meaning that multiple signals will result in cross-terms. This characteristic is detrimental to its ability to handle multiple moving targets.

Barbarossa and Farina first proposed using the Wigner–Ville distribution to examine moving targets in SAR images [2]. One of their chief observations was that while a moving target may have a large bandwidth when examined over the entirety of the collection, its instantaneous bandwidth is proportional to object size. Subsequently, this technique has been adopted by a number of researchers and well covered in the literature [3, 8]. Chen and Ling's book [9] provides an overview of time-frequency transforms and their application to radar, including ISAR and moving targets in SAR.

While this approach is very promising, there are several practical issues with the implementation of most joint time-frequency techniques including having to deal with cross terms. In several of these techniques the Wigner-Ville distribution is performed only on the range bin with the highest overall

energy from the target return. A typical moving target may encompass many range bins, and thus only a small portion of the overall target energy will be used in the estimation of target motion.

One recent technique, MITRE keystone remapping, can remove the effects of linear range migration through a scaling of slow time [34]. The keystone remapping technique is innovative in that it does not require the estimation of target motion parameters nor the tracking of individual targets during a collection; but rather simply applying a correction to the image that is based entirely on known parameters of the radar collection. The effects of additional components of motion are not addressed, and further processing is required to detect, fully focus, and localize moving targets in a scene. An extension of the MITRE keystone technique that uses multiple centers to localize targets has been developed [37]. This technique can be used to increase target SNR before detection prior to applying a different SAR-GMTI method.

In both the prominent point and joint time-frequency methods there is no attempt to locate the target in the scene. Neither the prominent point, joint time-frequency, or the MITRE keystone methods provide an estimate of the target's velocity vector. The prominent point and MITRE keystone processing technique both introduce skewing of the moving target.

The approach presented is unique as it treats target focusing and localization as coupled problems. It focuses, locates, and provides a velocity vector for each target. This technique does not rely on specific target features such as prominent points that may not exist on realistic targets. It is not

seriously affected by cross terms that occur between multiple targets. It also does not neglect range acceleration, a term which is shown to be a significant contributor to phase error.

1.2 Thesis Outline and Contributions

The primary contribution of this thesis is the development of a novel method to focus, locate, and estimate velocity for a moving target. This method is demonstrated with real SAR data collected from an experimental Ka-band system and simulated X-band SAR data.

1.2.1 Chapter 2: Development of a mathematical framework for moving targets in SAR

The general effects of linear components of velocity on target motion are well known. However, the literature does not provide a model with enough detail to estimate components of velocity from measured phase errors. In order to use these effects of motion to estimate, a more detailed model of phase errors needs to be developed. A vector model of SAR geometry is developed and the effects of various components of velocity, including non-linear effects of motion, is derived for both traditional polar formatted SAR images and MITRE keystone formatted images.

1.2.2 Chapter 3: A novel method to focus, locate, and estimate velocity for a moving target

The derivation in chapter 2 provided a key insight into phase error induced by SAR motion: there are two sets of coupled terms in a moving target. The first is azimuth position and range velocity, and the second azimuth velocity and range acceleration. This novel technique uses the true azimuth position of the target from monopulse to determine the amount of range velocity induced azimuth shift and estimate range velocity. A series of overlapping sub-apertures is used to estimate range acceleration, at which point the azimuth velocity can be estimated through a search to maximum contrast. The approximations for motion induced phase error are most accurate near the scene center. Because of this range velocity is estimated iteratively until the target position converges to the scene center. The proposed method is demonstrated using aliased and non-aliased targets from an experimental Ka-Band system.

1.2.3 Chapter 4: Detection of a moving target using a single phase center

Traditionally, most detection techniques for moving targets have relied on information from multiple phase centers. Many techniques to detect moving targets using only one phase center focus on targets that have shifted into the exo-clutter region of the image. There are also a variety of techniques that rely on an exhaustive search of target position and velocity. These methods are typically restricted to targets with linear motion as the state space of

possible velocities otherwise becomes too large to be practically searched. A different set of techniques measures phase error. The problem with these techniques is that a uniform background can generate a large phase error. Fienup [18] proposed a method that detect targets by their induced phase error but requires an increase in sharpness. This chapter presents an extension of his technique that uses the MITRE keystone method to improve performance and allows the detection of targets in both endo and exo-clutter as well as targets that have aliased. The proposed technique is demonstrated with simulated radar data.

1.2.4 Chapter 5: Knowledge-based focusing of a moving target

This chapter describes the azimuth position uncertainty problem, the inability to determine the true azimuth position of a moving target with a single phase center. The use of *a priori* knowledge of the scene and target can be used to determine its position. The use of micro-Doppler to determine target orientation is also discussed. A synthetic moving target is focused using knowledge of the road system.

1.2.5 Chapter 6: Summary and future work

The important findings of the thesis are highlighted, and possibilities for future research are discussed. Methods to further validate the method using additional radar collections are reviewed.

Chapter 2

Development of a mathematical framework for moving targets in SAR

Synthetic aperture radar (SAR) is a technique that forms coherent images of objects based on their radio reflectivity. Fine resolution is achieved in range through signal bandwidth (most often through the use of a chirped pulse), and in azimuth through the synthesis of a synthetic aperture much larger than the physical antenna of the imaging device. For background the reader is referred to one of many descriptions of SAR in the open literature [7, 47] where the governing equations are derived in detail.

However, in this chapter several of the fundamental equations of SAR are reviewed in order to examine the changes introduced by the presence of moving targets. Several aspects of moving targets are made more clear through a re–factoring of the traditional derivation of SAR.

First, a simplified vector geometry is assumed based on a broadside collection. The target is assumed to be located near the scene center and motion terms that do not fall in the slant plane are ignored. The phase error terms that are caused by range velocity, range acceleration, and azimuth velocity are then examined. Range acceleration is considered while azimuth acceleration

is ignored as the SAR instrument is much more sensitive to motion in range.

Successful formation of a SAR image of a moving target involves detecting, focusing, and localization of a target within a stationary SAR scene. Current research in target tracking and motion estimation, as well as existing techniques for performing SAR imaging of moving targets, are reviewed.

2.1 Radar Targets

Complex radar objects such as a typical ground vehicle are composed of many individual elemental scatterers whose returns are interfering constructively and destructively. The radar returns of these complex objects thus vary with the aspect ratio between the target and the antenna phase center. This behavior is also seen when imaging rough surfaces where it is known as *speckle*. It is common to describe these targets in terms of their probability density function (PDF) of their radar cross section σ. This σ can vary, or fluctuate, rapidly as the aspect ratio between the target and the antenna phase center changes (as a result of motion from either the antenna phase center or motion from the target itself.

Peter Swerling of the RAND Corporation first characterized complex targets in terms of a statistical scattering model in the early 1950s [44–46]. Swerling described four cases of fluctuating targets which are now commonly known as model Swerling I-Swerling IV. Their distributions can be described

by the *chi-square* PDF given by Levanon [27] as:

$$p(\sigma) = \frac{k}{(k-1)!\bar{\sigma}} \left(\frac{k\sigma}{\bar{\sigma}} \right)^{k-1} \exp \frac{-k\sigma}{\bar{\sigma}}, 0 \leq \sigma \tag{2.1}$$

Setting $k = 1$ reduces (2.1) to a Rayleigh or exponential PDF. This is the model used for Swerling I and Swerling II targets. Swerling I targets fluctuate scan-to-scan but are constant from pulse-to-pulse. Swerling II models fluctuate pulse-to-pulse. A target with a dominant constant component and a Rayleigh-distributed random component is modeled by setting $k = 2$. This distribution is used for Swerling III and Swerling IV targets. Swerling III targets fluctuate scan-to-scan but are constant from pulse-to-pulse. Swerling IV models fluctuate pulse-to-pulse.

There are a variety of other PDFs that can be used to describe the returns from complex targets. For a moving target the model will probably be somewhere between a Swerling III and a Swerling IV. The return from the target may not vary with every pulse, but will change over the course of the coherent processing interval. The specific PDF used to model a moving target is not as important as the concept that the return will change over the collection. The probability of detection will be less for a fluctuating target than that of a non-fluctuating target with the same average power. This behavior is known as *fluctuation loss*.

Radar cross section σ distributions from ground moving targets is a common area of research. Palubinskas *et. al* recently published a series of studies examining σ from passenger vehicles given a variety of radar look direc-

tions, incidence angles, and vehicle orientations from an X-band experimental airborne SAR system [32, 33].

2.2 SAR Fundamentals

A typical spotlight mode SAR flight geometry is shown in figure 2.1. A SAR instrument is mounted on an aircraft that is flying along a straight path. The SAR antenna is pointed at an area to the right of the flight path on the ground plane. As the aircraft flies along its flight path the SAR antenna is steered to keep it pointing at the same target patch. During this time the SAR instrument periodically sends out radio–frequency (RF) pulses that illuminate the target patch and are reflected back to the SAR instrument where they are sampled.

In SAR processing it is typical to distinguish between fast time t (the time within a single radar pulse) and slow time τ (time within the entire synthetic aperture). For the purpose of these derivations, the positions of both the target and of the antenna phase centers are considered to be fixed within a single transmitted pulse. This requires that the velocities of either will not be great enough to move the target a significant portion of a wavelength in range ($\lambda/10$) over the duration of the transmitted pulse. This is often, but not always, the case for moving targets; and if this restraint is violated it will induce additional errors in the SAR image that will need to be compensated for.

Most SAR image formation algorithms can be thought of as performing

a matched filter operation to positions in the scene image. All efficient image formation algorithms depend on approximations of the SAR governing equations. The quality of the final image will be dependent on the accuracy of the approximation. Many of the assumptions made for processing stationary backgrounds are not applicable for the imaging of moving targets, and because of this is it necessary to reexamine the underlying equations and approximations.

For the purpose of this work, moving targets are assumed to be rigid bodies that are composed of a large number of elemental point scatterers. Here a framework for understanding the SAR imaging process is developed starting from equations describing the return from a single elemental scatterer and continuing through the 2D imaging process.

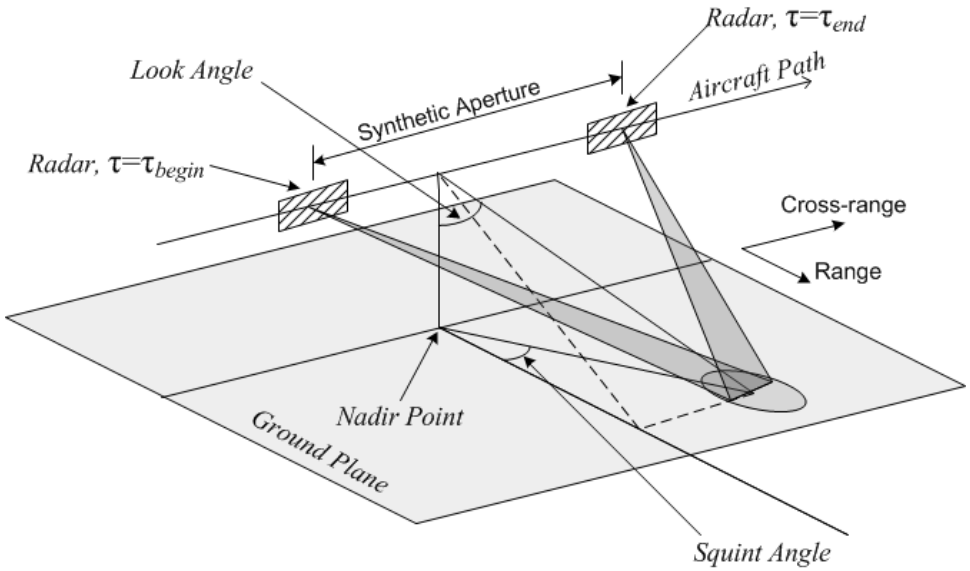

Figure 2.1: A typical spotlight mode SAR image collect

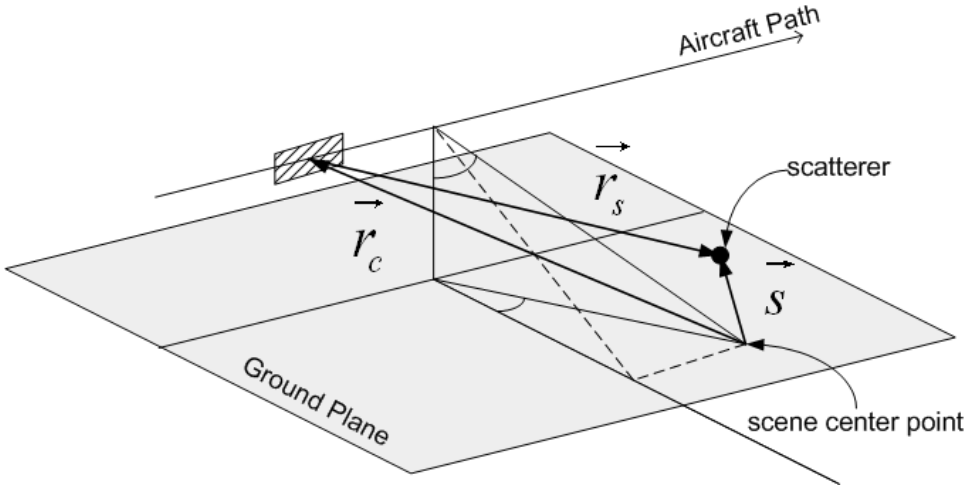

Figure 2.2: Vector definition of target geometry

2.3 Definition of a SAR Geometry

Figure 2.3 shows a model for a Spotlight mode SAR collection. The geometry is defined based on a scene center point – this is the point at which the imaging device remains focused for the duration of the radar flight. The location of the antenna phase center with respect to this scene center point is defined as the vector $\vec{r}_c = r_{c,x}\hat{x} + r_{c,y}\hat{y} + r_{c,z}\hat{z}$. The location of the moving target with respect to the scene center point is defined as $\vec{s} = s_x\hat{x} + s_y\hat{y} + s_z\hat{z}$. Finally, the location of the moving target with respect to the antenna phase center is defined as $\vec{r}_s = \vec{s} - \vec{r}_c$.

2.3.1 Approximation of range to target

The range to the target from the phase center of the antenna is given as:

$$\begin{aligned} r_s &= \sqrt{\vec{r_s}\vec{r_s}} \\ &= \sqrt{\left(\vec{s}-\vec{r_c}\right)\left(\vec{s}-\vec{r_c}\right)} \\ &= r_c\left(1-2\frac{\vec{s}}{r_c}\frac{\vec{r_c}}{r_c}+\frac{s^2}{r^2}\right)^{1/2} \\ &= r_c\left(1-2\left[\frac{\vec{s}\hat{r_c}}{r_c}+\frac{s^2}{2r^2}\right]\right)^{1/2} \end{aligned} \tag{2.2}$$

Using a binomial expansion this can be expanded as:

$$\begin{aligned} r_s &= r_c\left(1-2\left[\frac{\vec{s}\hat{r_c}}{r_c}+\frac{s^2}{2r^2}\right]\right)^{1/2} \\ &= r_c\left(1-2\alpha\right)^{1/2} \\ &= r_c\left\{1-\alpha-\frac{1}{2}\alpha^2-\frac{1}{2}\alpha^3\ldots\right\} \\ &= r_c\left\{1-\left[\frac{\vec{s}\hat{r_c}}{r_c}+\frac{s^2}{2r^2}\right]-\frac{1}{2}\left[\frac{\vec{s}\hat{r_c}}{r_c}+\frac{s^2}{2r^2}\right]^2-\frac{1}{2}\left[\frac{\vec{s}\hat{r_c}}{r_c}+\frac{s^2}{2r^2}\right]^3\ldots\right\} \end{aligned} \tag{2.3}$$

From the assumption that $s \ll r_c$ it follows that $s/r_c \ll 1$ and ${s^2}/{r_c}^2$ and higher terms can be ignored. This leaves the approximation:

$$\begin{aligned} r_s &= r_c\left(1-\frac{\vec{s}\hat{r_c}}{r_c}\right) \\ &= r_c-\vec{s}\hat{r_c} \\ &= r_c-proj_{\vec{r_c}}\left(\vec{s}\right) \end{aligned} \tag{2.4}$$

2.3.2 Approximation of target phase

Equation (2.4) and (A.10) can be combined to get an approximation of the target phase after the deramping.

$$\begin{aligned}\Delta_r &= r_c - r_s \\ &= r_c - [r_c - \vec{s}\hat{r_c}] \\ &= \vec{s}\hat{r_c}\end{aligned} \tag{2.5}$$

$$\begin{aligned}\Phi_{deramp}(t) &= -2k\Delta_r \\ &= -2k\vec{s}\hat{r_c}\end{aligned} \tag{2.6}$$

The effects of motion in SAR images can now be derived from the approximation given in equation 2.6.

2.4 The effects of motion on SAR images

For a broadside geometry the dot product 2.5 can be written as:

$$\vec{s}\hat{r_c} = \sqrt{(r_{c,y}\hat{y})^2 - v_p\tau^2} - \sqrt{(s_x\vec{x} + v_a t - v_p\tau)^2 + \left(r_{c,y}\vec{y} + s_y\vec{y} + v_r\tau + \frac{1}{2}a_r\tau^2\right)^2} \tag{2.7}$$

This can be simplified via a Taylor expansion about $\tau = 0$:

$$\vec{s}\hat{r_c} = \vec{s}\hat{r_c}|_{\tau=0} + \tau\frac{\partial}{\partial\tau}\vec{s}\hat{r_c}|_{\tau=0} + \tau^2\frac{\partial^2}{\partial\tau^2}\vec{s}\hat{r_c}|_{\tau=0} + H.O.T. \tag{2.8}$$

where:

$$\vec{s}\hat{r_c}|_{\tau=0} = r_{c,y}\hat{y} - \sqrt{(r_{c,y} + s_y\hat{y})^2 + s_x\vec{x}^2} \tag{2.9}$$

$$\frac{\partial}{\partial\tau}\vec{s}\hat{r}_c|_{\tau=0} = \frac{(v_p - v_a)\, s_x\hat{x} + (r_{c,y} + s_y\hat{y})\, v_r}{\sqrt{(r_{c,y} + s_y\hat{y}) + s_x\hat{x}^2}} \tag{2.10}$$

$$\begin{aligned}\frac{\partial^2}{\partial\tau^2}\ \vec{s}\hat{r}_c|_{\tau=0} = &-\frac{v_p}{r_{c,y}\hat{y}} - \frac{v_r^2 + (v_p - v_a)^2 + (r_{c,y} + s_y\hat{y})\, a_r}{\sqrt{(r_{c,y} + s_y\hat{y}) + s_x\hat{x}^2}} \\ &+ \frac{\left[(v_p - v_a)\, s_x\hat{x} + (r_{c,y} + s_y\hat{y})\, v_r\right]^2}{\left[(r_{c,y} + s_y\hat{y}) + s_x\hat{x}^2\right]^{3/2}}\end{aligned} \tag{2.11}$$

The $\sqrt{(r_{c,y} + s_y\hat{y}) + s_x\hat{x}^2}$ term is the range to the target at the center of the aperture. This can be approximated with a binomial expansion as:

$$\sqrt{(r_{c,y} + s_y\hat{y}) + s_x\hat{x}^2} \approx r_{c,y}\hat{y} + s_y\hat{y} \tag{2.12}$$

Applying this simplification to the Taylor series terms yields:

$$\begin{aligned}\vec{s}\hat{r}_c|_{\tau=0} &= r_{c,y}\hat{y} - r_{c,y}\hat{y} + s_y\hat{y} \\ &\approx s_y\hat{y}\end{aligned} \tag{2.13}$$

$$\begin{aligned}\frac{\partial}{\partial\tau}\vec{s}\hat{r}_c|_{\tau=0} &= \frac{(v_p - v_a)\, s_x\hat{x} + (r_{c,y} + s_y\hat{y})\, v_r}{r_{c,y}\hat{y} + s_y\hat{y}} \\ &\approx \frac{(v_p - v_a)\, s_x\hat{x}}{(r_{c,y}\hat{y} + s_y\hat{y})} + v_r\end{aligned} \tag{2.14}$$

$$\begin{aligned}\frac{\partial^2}{\partial\tau^2}\vec{s}\hat{r}_c|_{\tau=0} = &-\frac{v_p}{r_{c,y}\hat{y}} - \frac{v_r^2 + (v_p - v_a)^2 + (r_{c,y} + s_y\hat{y})\, a_r}{\sqrt{(r_{c,y} + s_y\hat{y}) + s_x\hat{x}^2}} \\ &+ \frac{\left[(v_p - v_a)\, s_x\hat{x} + (r_{c,y} + s_y\hat{y})\, v_r\right]^2}{\left[(r_{c,y} + s_y\hat{y}) + s_x\hat{x}^2\right]^{3/2}} \\ \approx &\frac{v_p}{r_{c,y}\hat{y}} - \frac{v_r^2 + (v_p - v_a)^2}{(r_{c,y}\hat{y}s_y\hat{y})} - a_r\end{aligned} \tag{2.15}$$

This yields an approximation of $\vec{s}\hat{r_c}$ as:

$$\vec{s}\hat{r_c} = s_y\hat{y} \ + \frac{(v_p - v_a)\, s_x\hat{x}}{(r_{c,y}\hat{y} + s_y\hat{y})}\tau \ + v_r\tau - \frac{v_p}{2r_{c,y}\hat{y}}\tau^2 \ - \frac{v_r^2}{2\,(r_{c,y}\hat{y} + s_y\hat{y})}\tau^2 \\ - \frac{v_p^2}{2\,(r_{c,y}\hat{y} + s_y\hat{y})}\tau^2 \ - \frac{(v_a^2 + 2v_a v_p)}{2\,(r_{c,y}\hat{y} + s_y\hat{y})}\tau^2 \ - a_r\tau \tag{2.16}$$

At this point the effect of the various components of velocity can be considered. Here it is useful to use the following conversion as given in Fienup [18]:

$$2k = \frac{4\pi}{\lambda_0}\left(1 + \frac{f}{f_0}\right) \tag{2.17}$$

where $\lambda_0 = \frac{f_0}{c}$.

2.4.1 Range Velocity Phase

The phase component due to range velocity is found to be:

$$\begin{aligned}\phi\,(f + f_0, \tau)_{vr} &= -2k\left[v_r\tau - \frac{v_r^2}{2\,(r_{c,y}\hat{y} + s_y\hat{y})}\tau^2\right] \\ &= \frac{4\pi}{\lambda_0}\left(1 + \frac{f}{f_0}\right)\left[v_r\tau - \frac{v_r^2}{2\,(r_{c,y}\hat{y} + s_y\hat{y})}\tau^2\right]\end{aligned} \tag{2.18}$$

The primary effect of range velocity is a shift in the target's azimuth position (Fig. 2.3):

$$\phi\,(f + f_0, \tau) = -2kv_r\tau \tag{2.19}$$

If the range velocity is sufficiently enough, the shift in the target energy will cause the target energy to alias. The velocity at which the target will alias depends on the pulse repetition frequency of the radar.

$$V_{alias} = \frac{PRF}{4}\lambda \tag{2.20}$$

If the pulse repetition frequency is increased beyond what is required for a normal SAR collection, a portion of the range-Doppler domain will be clutter free. This is known as the exo-clutter region, while the portion of the range-Doppler domain containing returns from ground clutter is known as the endo-clutter region. It is desirable to have a radar collection where there is a large exo-clutter region as this will increase the chance that a target is detected and its phase separated from background. The minimum range velocity required to shift a moving target into the exo-clutter region is the V_{alias} velocity with the PRF set to the minimum required to sample the return from the ground clutter. From the Nyquist sampling theorem this minimum sampling frequency must be twice the significant azimuth signal bandwidth. Assuming uniform illumination of the scene this is given as [11]:

$$PRF > \Delta f_{dop} = \frac{2v_p \cos\theta_s}{\lambda}\theta_{BW} \tag{2.21}$$

$$\theta_{BW} = 0.886\lambda/L_a \tag{2.22}$$

where θ_s is the squint angle, θ_{BW} is the 3-dB width of the radar beam, and L_a is the length of the antenna. As Δf_{dop} is the $3dB$ bandwidth there will be some significant clutter energy that extends past this point. The factor by which the clutter extends beyond the 3-dB point is known as $K_{exoclutter}$ and is typically around 3 [14]. The minimum range velocity that will shift a moving target into the exo-clutter region is given as:

$$V_{exoclutter} = \frac{v_p \cos\theta_s}{2K_{exoclutter}}\theta_{BW} \tag{2.23}$$

Combing this constraint and (2.20) means that the target range velocity must fit the following constraint to fall in the exo-clutter region of the image:

$$V_{exoclutter} < (v_r \bmod V_{alias}) < V_{alias} \tag{2.24}$$

There is also a quadratic phase component:

$$\phi\left(f + f_0, \tau\right) = \frac{4\pi}{\lambda_0}\left[\frac{v_r^2}{2\left(r_{c,y}\hat{y} + s_y\hat{y}\right)}\tau^2\right] \tag{2.25}$$

as well as a range walk component:

$$\phi\left(f + f_0, \tau\right) = \frac{4\pi}{\lambda_0}\left(\frac{f}{f_0}\right)\left[\frac{v_r^2}{2\left(r_{c,y}\hat{y} + s_y\hat{y}\right)}\tau^2\right] \tag{2.26}$$

2.4.2 Cross-range velocity phase

Cross-range (or azimuth) velocity primarily causes a quadratic phase error (Fig. 2.4). The phase component due to cross-range velocity is:

$$\phi\left(f + f_0, \tau\right)_{vr} = -2k\left[\frac{\left(v_p - v_a\right)s_x\hat{x}}{\left(r_{c,y}\hat{y} + s_y\hat{y}\right)}\tau - \frac{\left(v_a^2 - 2v_a v_p\right)}{2\left(r_{c,y}\hat{y} + s_y\hat{y}\right)}\tau^2\right] \tag{2.27}$$

Near the scene center $s_x\hat{x} \ll \left(r_{c,y}\hat{y} + s_y\hat{y}\right)$ and this can be approximated as:

$$\begin{aligned}\phi\left(f + f_0, \tau\right)_{va} &= 2k\left[\frac{\left(v_a^2 - 2v_a v_p\right)}{2\left(r_{c,y}\hat{y} + s_y\hat{y}\right)}\tau^2\right] \\ &= \frac{4\pi}{\lambda_0}\left(1 + \frac{f}{f_0}\right)\left[\frac{\left(v_a^2 - 2v_a v_p\right)}{2\left(r_{c,y}\hat{y} + s_y\hat{y}\right)}\tau^2\right]\end{aligned} \tag{2.28}$$

This has a quadratic phase component:

$$\phi\left(f + f_0, \tau\right) = \frac{4\pi}{\lambda_0}\left[\frac{\left(v_a^2 - 2v_a v_p\right)}{2\left(r_{c,y}\hat{y} + s_y\hat{y}\right)}\tau^2\right] \tag{2.29}$$

as well as a range walk component:

$$\phi\left(f + f_0, \tau\right)_{va} = \frac{4\pi}{\lambda_0}\left(\frac{f}{f_0}\right)\left[\frac{\left(v_a^2 - 2v_a v_p\right)}{2\left(r_{c,y}\hat{y} + s_y\hat{y}\right)}\tau^2\right] \tag{2.30}$$

2.4.3 Range acceleration phase

Range acceleration, like cross-range velocity, mainly causes a quadratic phase error. The phase component due to range acceleration is:

$$\begin{aligned}\phi\left(f+f_0,\tau\right)_{va} &= 2ka_r\tau^2 \\ &= \frac{4\pi}{\lambda_0}\left(1+\frac{f}{f_0}\right)\frac{1}{2}a_r\tau^2\end{aligned} \tag{2.31}$$

As with cross-range velocity this has a quadratic phase component:

$$\phi\left(f+f_0,\tau\right) = \frac{4\pi}{\lambda_0}\frac{1}{2}a_r\tau^2 \tag{2.32}$$

As well as a range walk component:

$$\phi\left(f+f_0,\tau\right) = \frac{4\pi}{\lambda_0}\left(\frac{f}{f_0}\right)\frac{1}{2}a_r\tau^2 \tag{2.33}$$

At this point it is useful to consider the relationship between phase error induced by azimuth velocity and that introduced through range acceleration. By examination these will be equal when:

$$a_r = \frac{(v_a^2 - 2v_a v_p)}{r_{c,y}+s_y} \tag{2.34}$$

For the real SAR data used in this thesis $v_p = 48.3m/s$ and $r_{c,y}+s_y \approx 3800m$. A range acceleration of only $0.0252m/s^2$ will have the same phase error as $1m/s$ of azimuth velocity. For the simulated data used in this thesis $v_p = 500m/s$ and $r_{c,y}+s_y \approx 30000m$. A range acceleration of $0.653m/s^2$ (Fig. 2.5) will have approximately the same phase error as $20m/s$ of azimuth velocity (Fig. 2.4).

An accurate velocity vector can not be estimated if range acceleration is ignored.

2.4.4 Cross-range acceleration and other motion errors

It is common in SAR-GMTI to assume linear target motion [29, 54]. A linear motion model is not adequate as the phase error due to range acceleration can be a significant. The motion model used here, while it does not encompass all possible target motion, appears to be detailed enough to estimate target location and velocity as seen in chapter 3. There are additional motion components that may contribute to phase error. One such component is cross-range acceleration, although it is not nearly as significant as the terms previously considered (Fig. 2.6). In general there is a trend that can be observed between range and cross range phase contributions. Range velocity and cross-range position, range acceleration and cross-range velocity, and range jerk and cross-range acceleration (Fig. 2.6 and 2.7) cause similar motion errors. Vibration and rotation can also cause significant phase errors. Rotation can be thought of as half of the target moving toward the antenna phase center while the other half moves away, while vibration causes the target to alternatively accelerate toward and away from the antenna phase center.

2.5 The MITRE keystone technique

Perry *et al.* developed a method known as *keystone remapping* that can be used to partially focus moving targets by decoupling linear range migration [34] from slow time. It is based on the observation that Doppler scales with frequency [15]. This technique is innovative in that it does not require the estimation of target motion parameters nor the tracking of individual targets

during a collection; but rather simply applying a correction to the image that is based entirely on known parameters of the radar collection. By decoupling linear range from slow time this technique removes a moving target's range migration and the blurring caused by this motion. Further processing is clearly required to detect, fully focus, and localize moving targets in a scene; however this technique can make this process more feasible as partially focusing a target will increase its signal to clutter ratio.

Their keystone method is derived here based on the nomenclature developed above. This derivation is based on phase returns not motion compensated to a point to aid in the clarity of the presentation, however, this technique is typically applied to deramped data.

First, the equation for a target return developed in (A.11) is down converted:

$$\begin{aligned} s(\tau,t)\exp(-j\omega_0 t) &= C\exp\left\{j\left[\omega_0\left(t-\frac{d(\tau)}{c}\right)+\gamma\left(t-\frac{d(\tau)}{c}\right)^2\right]\right\}\exp(-j\omega_0 t) \\ &= C\exp\left\{j\left[\omega_0\left(-\frac{d(\tau)}{c}\right)+\gamma\left(t-\frac{d(\tau)}{c}\right)^2\right]\right\} \end{aligned} \tag{2.35}$$

Next, a fourier transform in fast time t is performed on the down converted signal:

$$\begin{aligned} S(\tau,f) &= C\mathcal{F}\left\{exp\left\{j\left[\omega_0\left(-\frac{d(\tau)}{c}\right)+\gamma\left(t-\frac{d(\tau)}{c}\right)^2\right]\right\}\right\} \\ &= Cexp\left(-j\omega_0\frac{d(t)}{c}\right)exp\left(-j2\pi f\frac{d(t)}{c}\right)\mathcal{F}\left\{exp\left(j\gamma t^2\right)\right\} \end{aligned} \tag{2.36}$$

Now by defining the function $p(t)$ as:

$$p(t) = exp\big(j\gamma t^2\big) \tag{2.37}$$

Equation (2.36) can be rewritten as:

$$\begin{aligned} S(\tau, f) &= CP(f)\, exp\left(-j\omega_0 \frac{d(t)}{c}\right) exp\left(-j2\pi f \frac{d(t)}{c}\right) \\ &= CP(f)\, exp\left[-j\frac{2\pi}{c}(f_0 + f)\, d(\tau)\right] \end{aligned} \tag{2.38}$$

Performing a MacLaurin expansion on $d(\tau)$ yields:

$$d(\tau) = d(0) + \dot{d}(0)\,\tau + \phi \tag{2.39}$$

$$\phi(\tau) = \ddot{d}(0)\,\tau^2 + \dddot{d}(0)\,\tau^3 + \cdots \tag{2.40}$$

Substituting (2.39) in (2.38) yields

$$S(t, f) \;=\; CP(f)\, exp\left[-j\frac{2\pi}{c}(f_0 + f)\left(d(0) + \dot{d}(0)\,\tau + \phi\right)\right] \tag{2.41}$$

Now, a transformation of slowtime is introduced:

$$\tau = \frac{f_0}{f + f_0}\tau' \tag{2.42}$$

substituting (2.42) into (2.41) yields a phase return with linear range decoupled from slow time:

$$\begin{aligned} &S(\acute{\tau}, f) = \\ &\quad CP(f)\, exp\left\{-j\frac{2\pi}{c}\left[(f_0 + f)\, d(0) + \dot{d}(0)\, f_0\acute{\tau} + (f + f_0)\phi\left(\frac{f_0\acute{\tau}}{f + f_0}\right)\phi\right]\right\} \end{aligned} \tag{2.43}$$

Through the application of a Taylor series expansion the transformation of slow time (2.42) can be refactored as:

$$\begin{aligned}
\frac{f_0}{f_0+f} &= f_0\left(\frac{1}{1+\frac{f}{f_0}}\right) \\
&= f_0\sum_{n=0}^{\infty}\left(-\frac{f}{f_0}\right)^n, && \text{as } \left|\frac{f}{f_0}\right| < 1 \\
&= f_0\left(1-\frac{f}{f_0}+\frac{f^2}{f_0^2}-\dots\right) \\
&= f_0 - f
\end{aligned} \tag{2.44}$$

This approximation can be used to examine the effects of the MITRE keystone technique on phase errors induced on various components of velocity.

2.5.1 Range velocity phase

The phase component due to range velocity is:

$$\begin{aligned}
\phi\left(f+f_0,\acute{\tau}\right)_{vr} &= -2k\left[v_r\tau - \frac{v_r^2}{2\left(r_{c,y}\hat{y}+s_y\hat{y}\right)}\tau^2\right] \\
&= -\frac{4\pi}{c}\left(f_0+f\right)v_r\tau + \frac{4\pi}{c}\left(f_0+f\right)\frac{v_r^2}{2\left(r_{c,y}\hat{y}+s_y\hat{y}\right)}\tau^2 \\
&= -\frac{4\pi}{c}f_0 v_r\acute{\tau} + \frac{4\pi}{c}f_0\frac{f_0}{f_0+f}\frac{v_r^2}{2\left(r_{c,y}\hat{y}+s_y\hat{y}\right)}\acute{\tau}^2 && \text{let } \tau = \frac{f_0}{f+f_0}\acute{\tau} \\
&= -\frac{4\pi}{c}f_0 v_r\acute{\tau} + \frac{4\pi}{c}f_0\left(f_0-f\right)\frac{v_r^2}{2\left(r_{c,y}\hat{y}+s_y\hat{y}\right)}\acute{\tau}^2 && \text{by (2.44)}
\end{aligned} \tag{2.45}$$

As with polar formatting, the primary effect of range velocity is a shift in the azimuth position of the target:

$$\phi\left(f+f_0,\acute{\tau}\right) = -2k_0 v_r\acute{\tau} \tag{2.46}$$

along with a quadratic phase component:

$$\phi\left(f+f_0,\tau\right)=\frac{4\pi}{\lambda_0}f_0\left[\frac{v_r^2}{2\left(\left(r_{c,y}\hat{y}+s_y\hat{y}\right)\right.}\acute{\tau}^2\right] \tag{2.47}$$

and a range walk component:

$$\phi\left(f+f_0,\acute{\tau}\right)=-\frac{4\pi}{\lambda_0}f\left[\frac{v_r^2}{2\left(r_{c,y}\hat{y}+s_y\hat{y}\right)}\acute{\tau}^2\right] \tag{2.48}$$

2.5.2 Cross-range velocity phase

The phase component due to cross-range velocity phase near the scene center is:

$$\begin{aligned}
\phi\left(f+f_0,\acute{\tau}\right)_{va} &= 2k\left[\frac{\left(v_a^2-2v_av_p\right)}{2\left(r_{c,y}\hat{y}+s_y\hat{y}\right)}\tau^2\right] \\
&= \frac{4\pi}{c}\left(f_0+f\right)\frac{\left(v_a^2-2v_av_p\right)}{2\left(r_{c,y}\hat{y}+s_y\hat{y}\right)}\tau^2 \\
&= \frac{4\pi}{c}f_0\left(\frac{f_0}{f_0+f}\right)\frac{\left(v_a^2-2v_av_p\right)}{2\left(r_{c,y}\hat{y}+s_y\hat{y}\right)}\acute{\tau}^2 \qquad \text{let } \tau=\frac{f_0}{f+f_0}\acute{\tau} \\
&= \frac{4\pi}{\lambda_0}\left(f_0-f\right)\frac{\left(v_a^2-2v_av_p\right)}{2\left(r_{c,y}\hat{y}+s_y\hat{y}\right)}\acute{\tau}^2 \qquad \text{by (2.44)}
\end{aligned} \tag{2.49}$$

This has a quadratic phase component:

$$\phi\left(f+f_0,\acute{\tau}\right)=\frac{4\pi}{\lambda_0}f_0\left[\frac{\left(v_a^2-2v_av_p\right)}{2\left(r_{c,y}\hat{y}+s_y\hat{y}\right)}\acute{\tau}^2\right] \tag{2.50}$$

as well as a range walk component:

$$\phi\left(f+f_0,\acute{\tau}\right)_{va}=\frac{4\pi}{\lambda_0}f\left[\frac{\left(v_a^2-2v_av_p\right)}{2\left(r_{c,y}\hat{y}+s_y\hat{y}\right)}\acute{\tau}^2\right] \tag{2.51}$$

2.5.3 Range acceleration phase

Range acceleration induced phase is given as:

$$\begin{aligned}
\phi\left(f+f_0,\acute{\tau}\right)_{va} &= 2ka_r\tau^2 \\
&= \frac{4\pi}{c}\left(f_0+f\right)\frac{1}{2}a_r\tau^2 \\
&= \frac{4\pi}{c}f_0\left(\frac{f_0}{f_0+f}\right)\frac{1}{2}a_r\acute{\tau}^2 \qquad \text{let } \tau=\frac{f_0}{f+f_0}\acute{\tau} \\
&= \frac{4\pi}{c}f_0\left(f_0-f\right)\frac{1}{2}a_r\acute{\tau}^2 \qquad \text{by (2.44)}
\end{aligned} \tag{2.52}$$

again this has a quadratic phase component:

$$\phi\left(f+f_0,\acute{\tau}\right)=\frac{4\pi}{\lambda_0}f_0\frac{1}{2}a_r\acute{\tau}^2 \tag{2.53}$$

as well as a range walk component:

$$\phi\left(f+f_0,\acute{\tau}\right)=\frac{4\pi}{\lambda_0}\left(f\right)\frac{1}{2}a_r\acute{\tau}^2 \tag{2.54}$$

2.6 Conclusion

This chapter reviewed several fundamental principles of SAR related to imaging a moving target. The phase errors induced by various components of target motion were derived for both polar formatted and MITRE keystone formatted data. It was shown that the primary contribution of range velocity is a shift in the cross-range or azimuth position of a target. The primary contribution of cross-range velocity was shown to be a quadratic phase error along with range walk. Range acceleration was similarly shown to induce quadratic phase error and range walk. It was shown that the MITRE keystone

method removes the effects of linear range motion. The exact amount of cross-range shift induced by range velocity for a target located near the scene center was quantified. The next chapter will build upon the derivations from this chapter to develop a novel method to focus, locate, and estimate velocity vectors for a moving target.

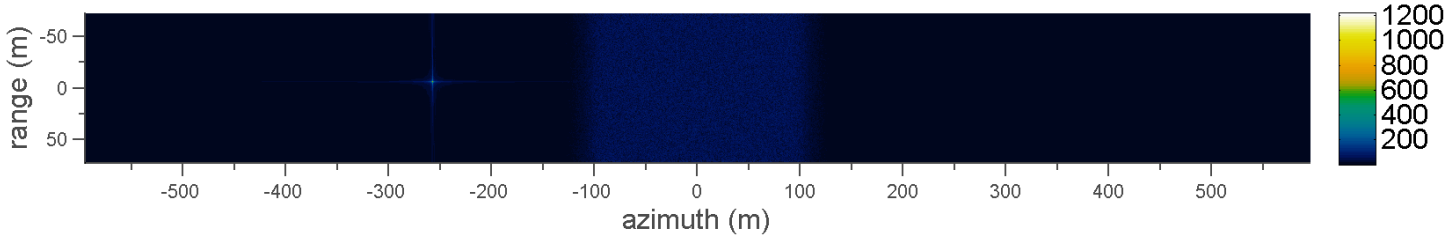

Figure 2.3: A full polar formated SAR scene with a simulated moving point target. The target is initially located at the origin with a range velocity of 5 m/s.

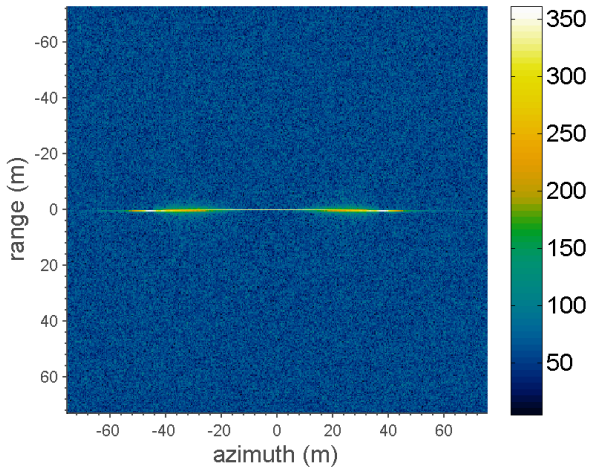

Figure 2.4: An endo-clutter SAR scene with a simulated moving point target. The target is initially located 20m in cross-range (azimuth) from the origin with a cross-range velocity of 5 m/s.

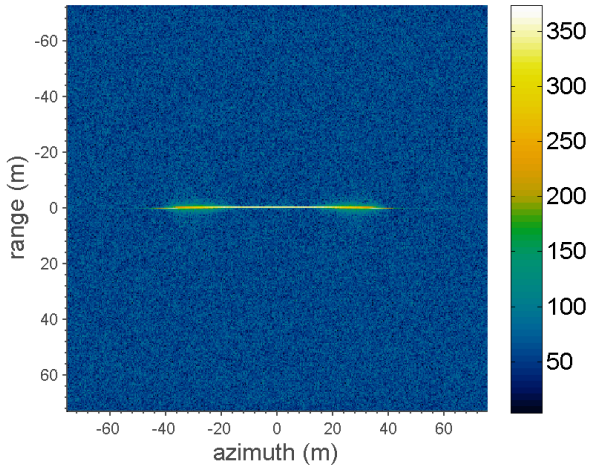

Figure 2.5: An endo-clutter SAR scene with a simulated moving point target. The target is initially located 40m in cross-range (azimuth) from the origin with a range acceleration of 0.653 m/s^2.

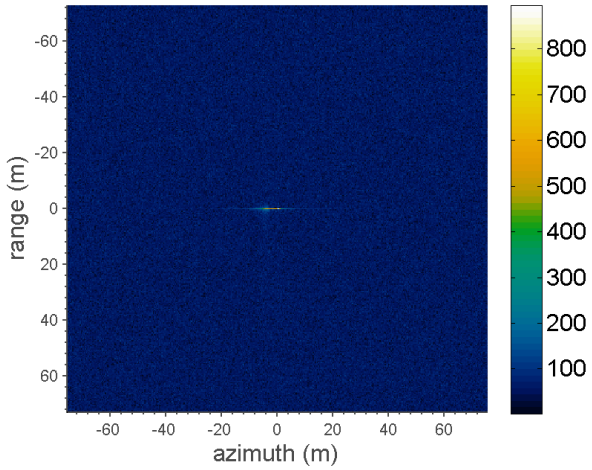

Figure 2.6: An endo-clutter SAR scene with a simulated moving point target. The target is initially located at the origin with a cross-range acceleration of 1 m/s^2.

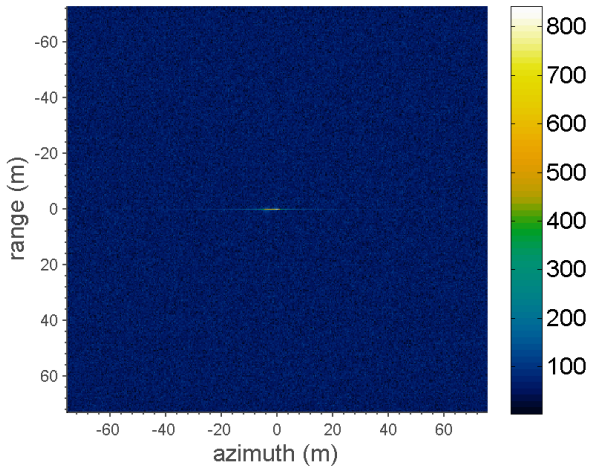

Figure 2.7: An endo-clutter SAR scene with a simulated moving point target. The target is initially located at the origin with a range jerk of 0.0333 m/s^3.

Chapter 3

A novel method to focus, locate, and estimate velocity for a moving target

Target motion causes both blurring of the target and a displacement of the target energy in a focused SAR image. The true location of targets can be estimated through angle-of-arrival measurements (using either along track interferometry or monopulse). This approach begins with a thorough re–examination of the effects of target motion on SAR imaging to determine what information can be gained by treating focusing and localization as coupled problems.

This approach is not limited to broadside mode collections or to focusing and locating targets near the scene center. Non-broadside collections can be converted to a broadside near equivalent through the application of the appropriate phase correction and targets are motion compensated to the scene center before estimates of target motion are made.

The three major errors that need to be corrected in a SAR image of a moving target have been shown to be translation due to range velocity, quadratic phase error due to azimuth velocity, and quadratic phase error due to range acceleration. Range velocity induced quadratic phase error also becomes

significant if v_r is not significantly less than v_p. All three components of velocity introduce a range walk, however, for a typical SAR geometry and vehicle velocities this will not be significant.

This approach was motivated by the observation that there are two major challenges in focusing a moving target in a SAR image. The first is decoupling the phase contributions caused by the target azimuth position from those induced by the target range velocity. This is accomplished by locating a target position in azimuth through the use of multiple phase centers. Here monopulse is used, however, this would also be possible through along–track interferometry. The second is decoupling the phase contributions from a target range acceleration and azimuth velocity. This is done by estimating target range velocity along a series of overlapping sub-apertures and then using linear least squared estimation to determine the target range acceleration. The phase errors remaining (at least those remaining from the translational motion of the target) are a result of the target azimuth velocity. This is determined by performing a search over possible azimuth velocities and evaluating target focus via an image quality metric.

First, a SAR image is formed of the scene containing moving targets. Possible targets identified through a combination of amplitude thresholding and deviation in the monopulse ratio. If the targets fall in the exo-clutter region of the image this detection is trivial. If targets are in the endo-clutter region some form of clutter cancellation might need to be applied prior to detection. There are other potential methods of identifying moving targets such

as through focusing [34]. A high false alarm rate in this initial identification is acceptable as one benefit of this new method is the ability to screen out false positives; if there is not a sufficient improvement in focus after processing it is unlikely to be a moving target.

3.1 Estimating true azimuth position through monopulse

Monopulse, as defined in the IEEE Standard on Radar Definitions, is "a radar technique in which information concerning the angular location of a source or target is obtained by comparison of signals received in two or more simultaneous antenna beams" [22]. An excellent treatise on the theory and history of monopulse radars is available in the book from Sherman [38]. There are two types of monopulse systems: amplitude-comparison monopulse, where multiple horn antennas are bundled in a parabolic reflector, and phase-comparison monopulse, where multiple antennas are separated by a baseline [36]. The separate channels in a monopulse system are not sampled directly. Instead a single sum signal (Σ) composed of the combined returns from all channels, and multiple difference signals (Δ) are sampled. The number of difference signals will vary with the number of phase channels in the monopulse system. The system used here has two phase centers and a single Δ channel. The monopulse ratio MPR is defined as:

$$MPR = \frac{\Delta}{\Sigma} = \frac{|\Delta|}{|\Sigma|} \exp j\left(\phi_{\Delta} - \phi_{\Sigma}\right) \tag{3.1}$$

The monopulse ratio varies with angle of arrival to target. For this

approach the ratio is calculated directly from the data for each coherent processing interval. The monopulse ratio is first measured over a 100 range bin segment of the image. This measured monopulse ratio is modeled with a 5th degree polynomial. A monopulse ratio for each target is then calculated from the mean of the monopulse ratio of each target pixel. This target MPR is mapped unto angle of arrival through the MPR polynomial, yielding an estimate of the actual azimuth position of the target.

3.2 Determining range velocity and acceleration through target shift

An approximate location of the moving target in the image is found through the detection process. The position of the target energy is estimated in the SAR image through a center of mass calculation on image intensity. This yields an estimate of the range position of the target and an azimuth position that is a result of both the actual azimuth position of the target and a shift caused by the target range velocity. This is combined with the estimate of the actual azimuth position from monopulse to yield an estimate of the target range velocity.

The target is focused using the MITRE keystone algorithm with different fold factors as the target range velocity may have been sufficient to cause the target energy to alias. The target focus with each fold factor is measured with an image quality metric (the C_2 measure of contrast shown in (3.4) is used). This provides an estimate of target range velocity to within a range of

$\pm PRF\left(\lambda\right)/4$.

The target range velocity is estimated across a series of overlapped sub-apertures. A range of sub-aperture sizes and number of total sub-apertures were tried before settling on a sub-aperture size of 500 with 50 overlapping sub-apertures. The optimal number and size of sub-apertures will vary with the radar collection parameters.

Each sub-aperture is seeded with the range velocity estimate from the previous sub-aperture (the initial sub-aperture is seeded with the range velocity estimate from the overall SAR image). A phase correction is then applied to motion compensate the target to the scene center based on the estimated position and range velocity of the target. An image is formed of the target with a 2D FFT. The center of mass of the pixel intensity in the scene center is calculated, a residual velocity error is determined, and the process is repeated until the calculated center of mass is less than a predetermined epsilon from the scene center. An epsilon of several thousandths of a pixel was found to work well, and the target center of mass was found to converge within a few iterations.

After the shift is measured over the series of overlapping sub-apertures, a first (velocity and acceleration) or second (velocity, acceleration, and jerk) order model is fitted to the measured velocities with linear least squared estimation (Fig. 3.1). The differential GPS data used for target velocity was not sufficient to measure target acceleration. The only way to validate a measure of range acceleration is by examining target focus and the accuracy of

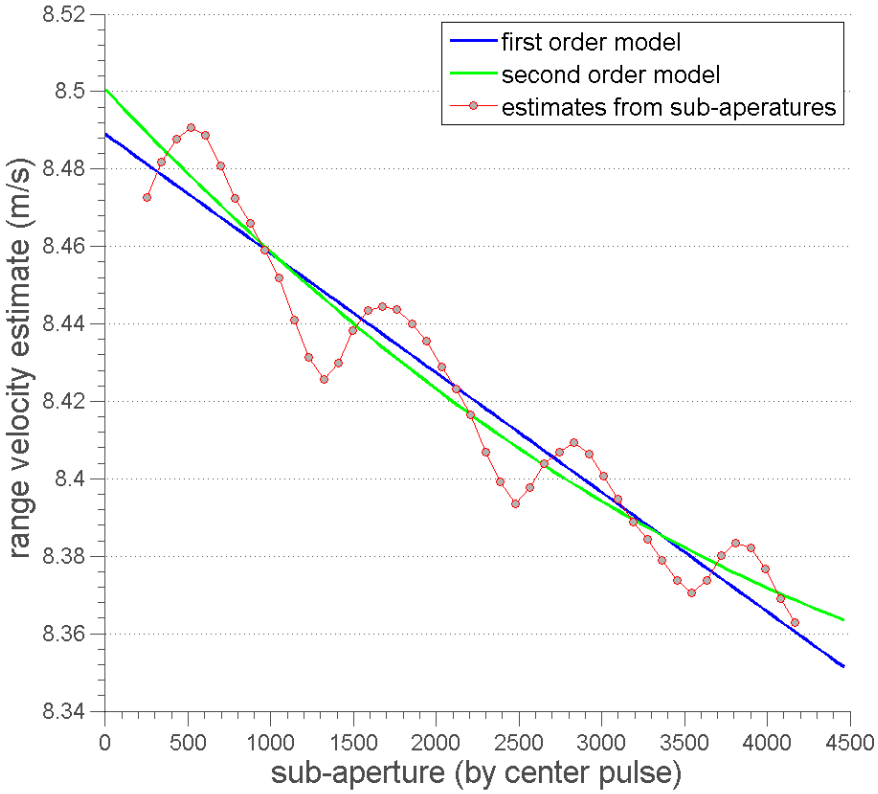

Figure 3.1: Range velocity estimates for sub-apertures for a water truck moving at 8.9m/s (20 mi/h)

the azimuth velocity with and without compensating for range acceleration. The estimates of azimuth velocity were improved when range acceleration was modeled (Table 3.1).

3.3 Azimuth velocity via search

Azimuth velocity is estimated by searching over possible azimuth velocities and measuring focus using an image metric. There are several image metrics that are well suited for determining the focus of a SAR target. Image metrics such as entropy [53] and contrast [5] have been widely used in autofocus techniques, including those for ISAR imaging [5]. The first metric considered is entropy, using the standard definition as follows [25].

$$S = -\sum_{i} P(i) \ln P(i) \tag{3.2}$$

where $P(\cdot)$ is the power density function of the signal. To calculate this in an image, the image is first scaled to L levels (0 to $L-1$). The PDF of the signal can be found by taking the L level histogram of the image and scaling it by the pixel count.

The next metric considered is contrast. Two different measurements of contrast were used from Berizzi and Corsini [5]. The first is the ratio of the standard deviation to the mean of the amplitude:

$$C_1 = \frac{\sqrt{\langle I(i,j) - \langle I(i,j)\rangle\rangle}}{\langle I(i,j)\rangle} \tag{3.3}$$

And the second is the ratio of the standard deviation to the mean of the intensity:

$$C_2 = \frac{\sqrt{\langle I^2(i,j) - \langle I^2(i,j)\rangle\rangle}}{\langle I^2(i,j)\rangle} \tag{3.4}$$

Finally, a measure of SNR defined as as the ratio of the amplitude of the peak target pixel to the average amplitude of a segment of noise pixels in the image was used:

$$SNR_{dB} = 20log10\frac{peak\,(I(i,j))}{\langle noisepixels \rangle} \tag{3.5}$$

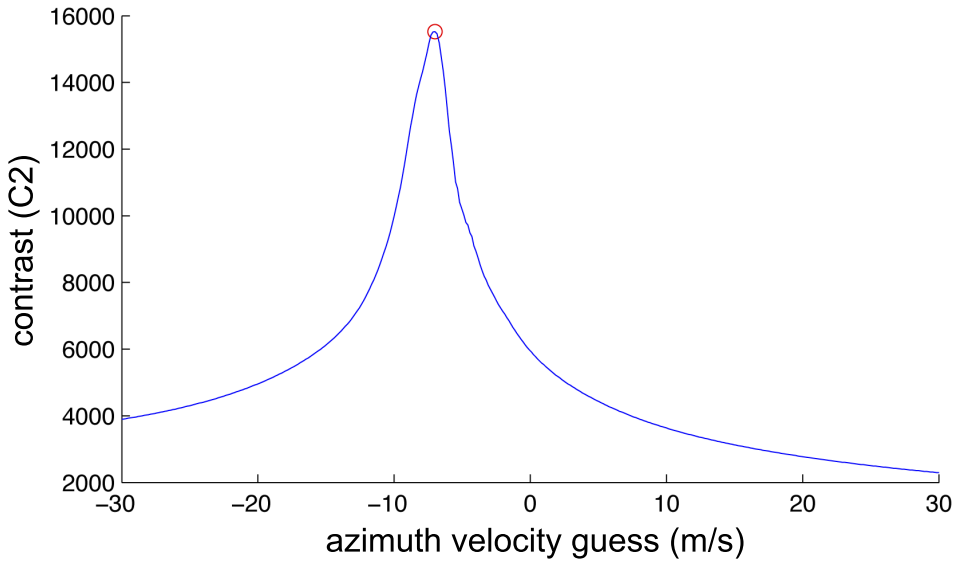

Figure 3.2: A search over azimuth velocity for maximum contrast using the C_2 (standard deviation over the mean of intensity) image quality metric

Searches using any of these four methods of image quality were successful. The metrics were well behaved over the search domain and there was no issue in converging to a specific velocity estimate (Fig. 3.2). The various image metrics converge to slightly different velocity estimates on some targets, however, the differences were small enough as to be insignificant. The C_2

measure of contrast was picked as the function is typically slightly smoother over the search domain than the other mentioned measures of image quality. The C_2 measure operates on image intensity rather than image amplitude and as such is biased toward bright pixels. It is anticipated that this will yield a better result as bright scatterers on the moving target, with higher SNR, are emphasized.

After estimating azimuth velocity a polar formatted image is formed with the position and a velocity vector estimate of the moving target.

3.4 Results

This technique was demonstrated with focused images of moving targets having both non-aliasing (2.2 m/s (5mi/h)) and aliasing (8.9 m/s (20mi/h)) velocities. Radar data was collected with two moving targets: a pickup truck and a water truck. Images from both vehicles were presented at both velocities using both the MITRE keystone technique and this new approach. The data is from a development radar system at Sandia. The image resolution was limited to 12 inches. The MITRE keystone images are not localized and in the focused images the targets appear at their original location in the scene. All targets were motion compensated with this new method to the scene center (that is, were motion compensated based on a new scene center point - the estimated position of the target) and so these targets appear at the origin.

This technique was expected to have noticeably improved results over the MITRE keystone technique in scenes where the target experiences sig-

nificant azimuth velocity or range acceleration. This is because these two components of motion are addressed while the MITRE technique only addresses linear range migration. This expected improvement was seen in the pickup truck moving at 2.2 m/s (5mi/h). The most noticeable attribute of the pickup truck is the bright return caused by the truck bed acting as a corner reflector (Fig. 3.5 and 3.11). The second attribute is the two sets of distinct micro-Doppler, corresponding to the two axles of the truck. These micro-Doppler returns are expected to be in focus when the target is in focus. The micro-Doppler is blurred but still distinct in the unfocused image of the pickup truck moving at 2.2 m/s (5mi/h) (Fig. 3.3). However, it is not visible in the unfocused image of the pickup truck moving at 8.9 m/s (20mi/h) (Fig. 3.9). Despite this the micro-Doppler is well focused in the MITRE keystone focused pickup truck moving at 8.9 m/s (20mi/h) (Fig. 3.10), but blurred in the MITRE keystone image of the pickup truck moving at 2.2 m/s (5mi/h) (Fig. 3.4). The pickup truck at 2.2 m/s (5mi/h) has both a lower range and azimuth velocity. This demonstrates the impact that range acceleration has on focusing. The micro-Doppler is well focused in the images of the pickup truck from the proposed method at both 2.2 m/s (5mi/h) (Fig. 3.5) and 8.9 m/s (20mi/h) (Fig. 3.11). As expected the period of the micro-Doppler is approximately four times greater at the higher velocity.

This technique has the ability to separate range acceleration from azimuth velocity through the use of overlapping sub-apertures. The rate and accuracy of the DGPS data used was not sufficient to provide target accelera-

tion. Improved focus and increased accuracy of azimuth velocities are needed to determine the legitimacy of the range acceleration estimates. Range acceleration was noticed to have an impact on azimuth velocity estimates when examining the images of the pickup truck. For the 2.2 m/s (5mi/h) case neglecting range acceleration yields around 5 m/s of error in the azimuth velocity estimate (Table 3.1). While estimating range acceleration consistently yields a better estimate of azimuth velocity, there is still some residual error in estimates of azimuth velocity that can be reduced with future improvements.

This new method is not dependent on specific target attributes such as prominent points to focus an image. This technique is demonstrated on a target (a water truck) lacking features that would enable focusing based on prominent points. The primary physical attribute of the water truck is a large metal cylinder. The water truck does not focus as well as the pickup truck due to the scattering properties of this cylinder . However, the focused image of the water truck was consistent between imaged scenes (Fig. 3.8 and 3.14). The velocity estimates were as accurate as those found from the pickup truck. This demonstrates the applicability of this method to targets with diverse scattering characteristics. The velocity of the water truck moving at 2.2 m/s (5 mi/h) is almost entirely in range. This causes a noticeable shift in target location, but relatively little blurring (Fig. 3.6). The range velocity of the water truck moving at 8.9 m/s (20 mi/h) shifted the target return close to the edge of the exo-clutter region of the image (Fig. 3.12). The MITRE keystone focused image of this target has an artifact that has occurred due to aliasing

from the slow time re-sampling and the proximity of the target to the scene edge (Fig. 3.13).

This proposed method outperforms the MITRE keystone technique both subjectively and when measured with a variety of image metrics (entropy, peak signal strength, two measures of contrast, and SNR) for all four example targets (Table 3.2). The difference in performance is most noticeable when the target has additional components of motion beyond linear range velocity. When motion is limited to linear range velocity, such as the water truck moving at 2.2m/s (5mi/h), the performance of the two techniques is similar. A velocity vector is also provided for each target. The estimated velocity and direction of vehicle motion corresponds well to measurements of vehicle motion from differential GPS (Table 3.1).

The final azimuth velocity estimates for many of the targets appear to be off by several meters per second. An examination of the estimated range velocity versus sub-aperture for both the pickup and water truck across different coherent processing intervals show a sinusoidal pattern of approximately 3Hz (Fig. 3.1). The period for both vehicles is different but appears to be fairly consistent across coherent processing intervals and independent of vehicle velocity. The observed periods correspond well to the expected resonant frequency of modern motor vehicles (1-5Hz, [23]) which indicates that this sinusoid may be the result of vehicle suspension system response to the road surface. In many of these intervals the sinusoid introduces a clear bias in the range acceleration estimate. It is possible that a more complex model of vehi-

cle motion or tracking the vehicle across multiple coherent processing intervals may improve the accuracy of range acceleration estimates. However, this vibration is more than a potential source for estimation error. The resonant frequency of a vehicle is dependent on the design of its suspension system, the age and condition of its shocks, and the weight of its cargo [23, 52]. If the resonant frequency can be measured accurately, this information may enable a radar system to distinguish between two vehicles of the same type with identical radar scattering properties. Further investigation is needed to determine if this periodic signal is due to vehicle vibration and if so, how that information can be exploited. Additional testing of this method is proposed using vehicles that are instrumented with strap down inertial measurement units. Having complete motion information for targets would provide further verification of this method, and allow for the extension of this work to additional forms of motion such as vibration and rotation.

3.5 Conclusion

This chapter presented a novel method to focus, locate, and estimate velocity for a moving target. The key insight of this technique is that the errors in the estimates of range velocity induced azimuth shift are lowest near the scene center. This method iteratively motion compensates, focuses, and measures shift for a moving target. Because this method does not neglect range acceleration, it is able to generate an estimate of azimuth velocity for real targets that are not constrained to linear motion. This method, as presented

Table 3.1: Estimated target velocities

Vehicle	Est. Order	Range Vel. (m/s)	Az. Vel. (m/s)
Pickup, 2.2 m/s (5mi/h)	DGPS	1.93	-0.35
	Zero	2.37	5.70
	First	2.47	-2.55
	Second	2.49	-0.49
Water Truck, 2.2 m/s (5mi/h)	DGPS	1.89	-0.37
	Zero	2.51	0.24
	First	2.52	-0.07
	Second	2.53	0.10
Pickup, 8.9 m/s (20mi/h)	DGPS	8.20	-1.92
	Zero	8.56	0.75
	First	8.56	0.33
	Second	8.56	0.36
Water Truck, 8.9 m/s (20mi/h)	DGPS	8.00	-1.91
	Zero	8.42	3.69
	First	8.49	-0.32
	Second	8.50	-0.59

Table 3.2: Image Metrics for Moving Targets

		Entropy	Peak Signal	C_1	C_2	SNR
Pickup, 2.2 m/s (5mi/h)	unfocused	3.70	5.35×10^8	773	5383	49.59
	keystone	3.77	4.39×10^8	770	5151	49.42
	new method	2.59	1.11×10^9	905	12096	56.89
Water Truck, 2.2 m/s (5mi/h)	unfocused	3.44	5.69×10^8	726	5434	50.40
	keystone	3.45	4.92×10^8	723	5328	50.50
	new method	3.43	5.73×10^8	726	5610	50.34
Pickup, 8.9 m/s (20mi/h)	unfocused	5.81	1.62×10^8	471	972	34.67
	keystone	2.40	6.83×10^8	1055	10674	53.44
	new method	2.05	2.16×10^9	1068	11656	57.34
Water Truck, 8.9 m/s (20mi/h)	unfocused	5.77	1.53×10^8	471	1168	35.64
	keystone	4.67	1.49×10^8	632	2493	40.90
	new method	3.41	9.48×10^8	747	3896	49.72

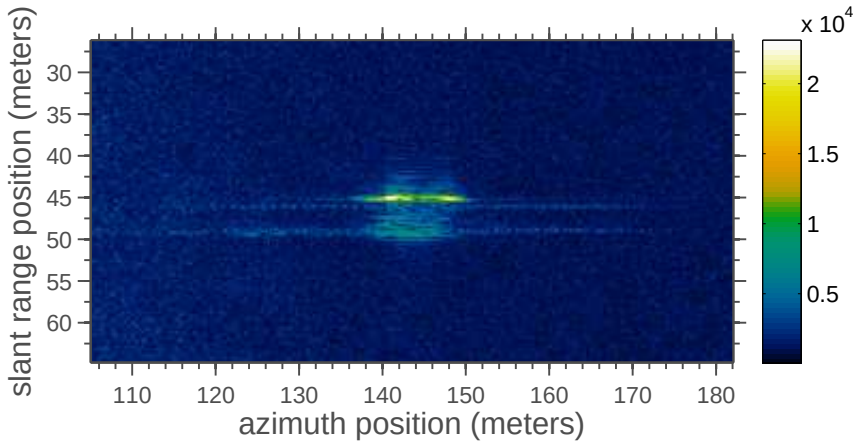

Figure 3.3: An unfocused pickup truck moving at 2.2 m/s (5mi/h). The image is displayed as the square root of magnitude.

here, relies upon the use of multiple phase centers to detect a target and estimate the true azimuth position of the target. Chapters 4 and 5 address these limitations.

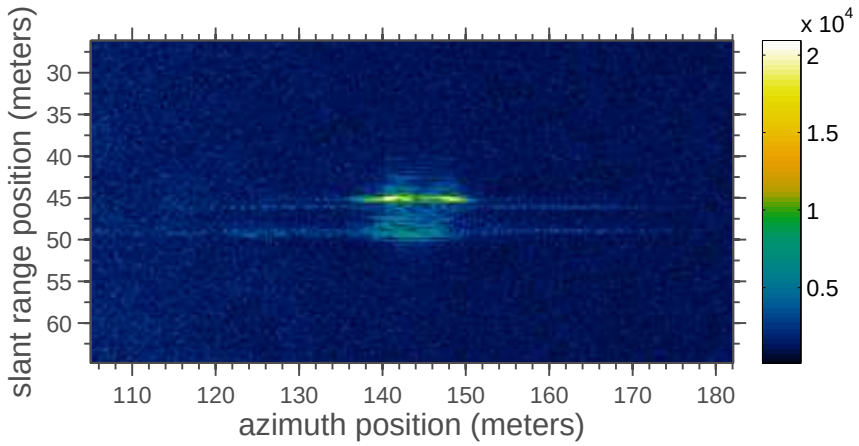

Figure 3.4: A pickup truck moving at 2.2 m/s (5mi/h) focused with the MITRE keystone technique. The images is displayed as the square root of magnitude.

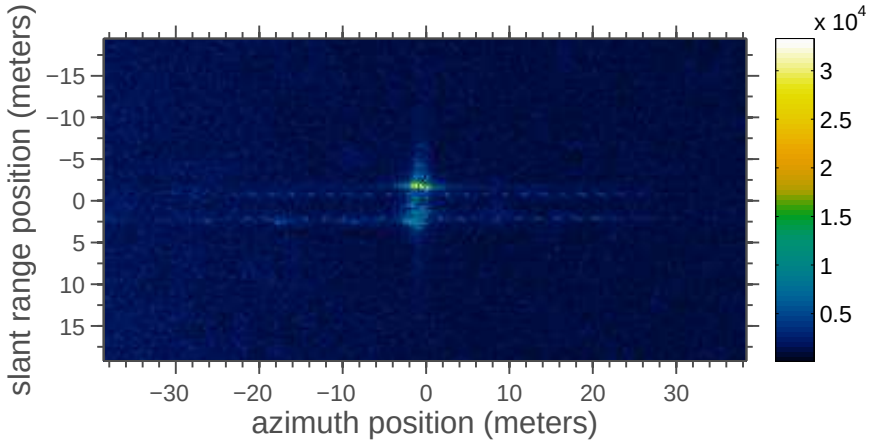

Figure 3.5: A pickup truck moving at 2.2 m/s (5mi/h) focused and located with the new proposed method. The images is displayed as the square root of magnitude.

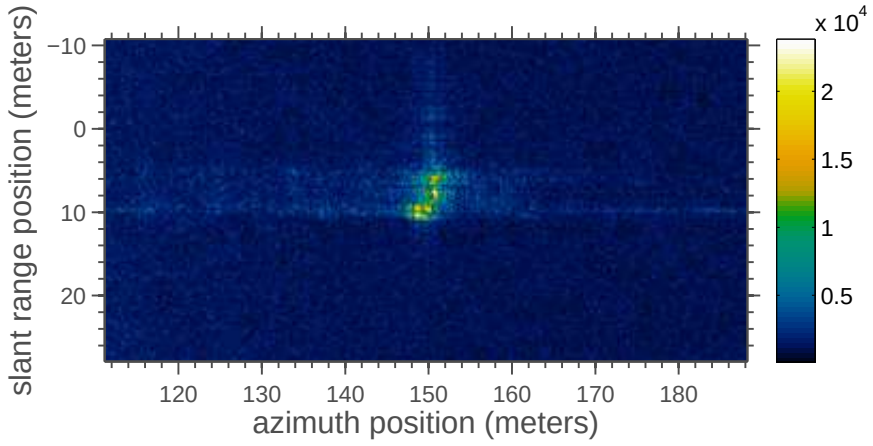

Figure 3.6: An unfocused water truck moving at 2.2 m/s (5mi/h). The image is displayed as the square root of magnitude.

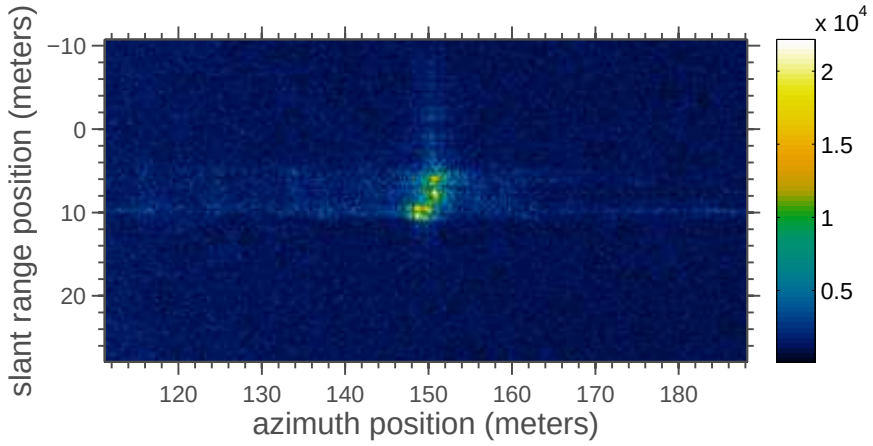

Figure 3.7: A water truck moving at 2.2 m/s (5mi/h) focused with the MITRE keystone technique. The images is displayed as the square root of magnitude.

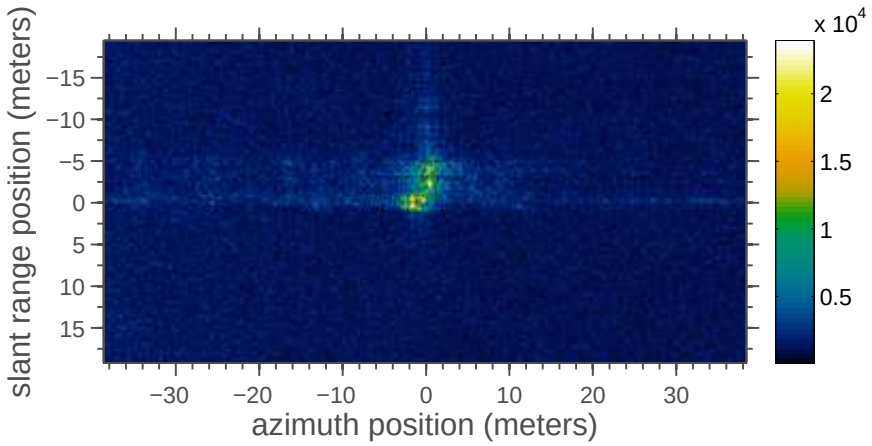

Figure 3.8: A water truck moving at 2.2 m/s (5mi/h) focused and located with the new proposed method. The images is displayed as the square root of magnitude.

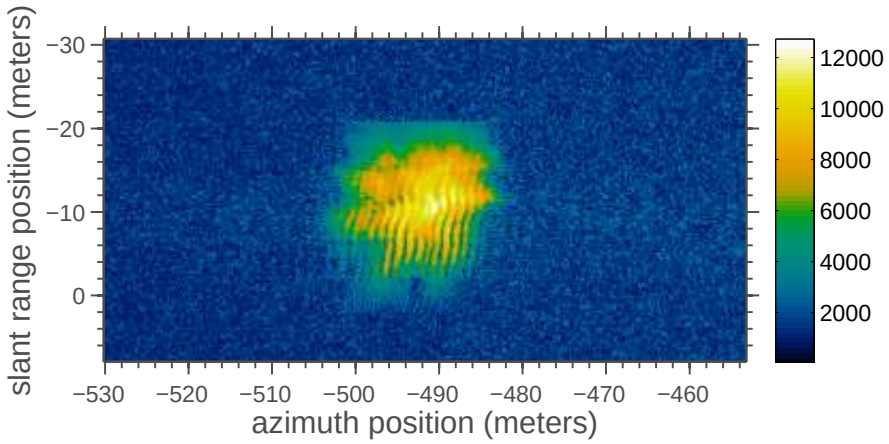

Figure 3.9: An unfocused pickup truck moving at 8.9 m/s (20mi/h). The image is displayed as the square root of magnitude.

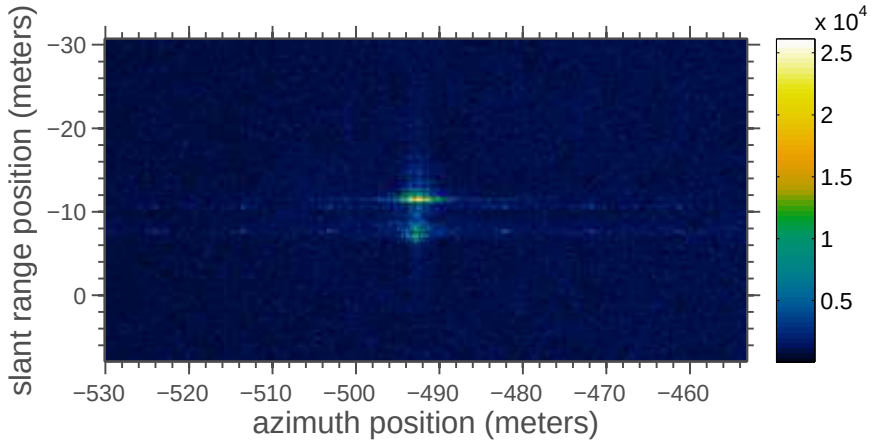

Figure 3.10: A pickup truck moving at 8.9 m/s (20mi/h) focused with the MITRE keystone technique. The images is displayed as the square root of magnitude.

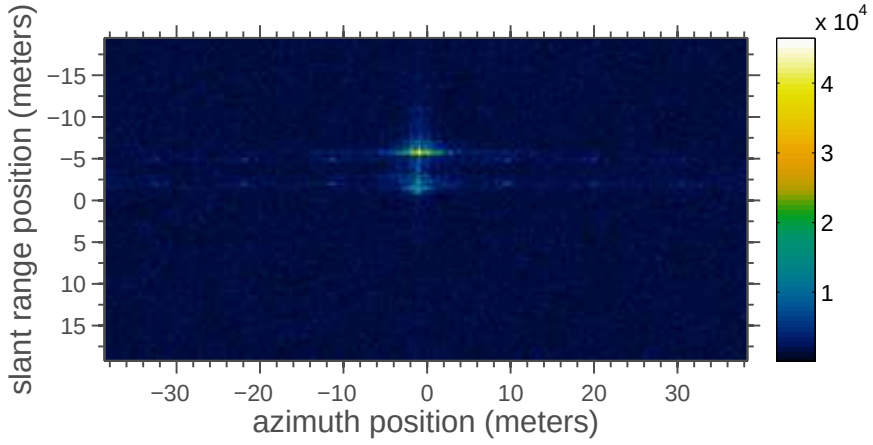

Figure 3.11: A pickup truck moving at 8.9 m/s (20mi/h) focused and located with the new proposed method. The images is displayed as the square root of magnitude.

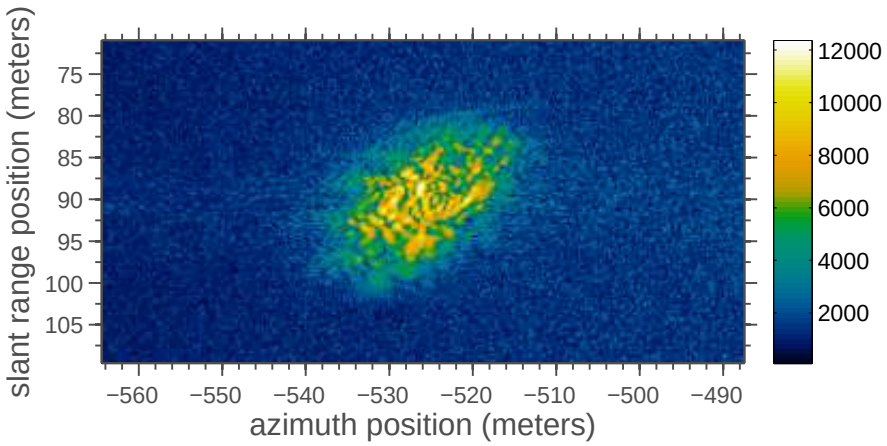

Figure 3.12: An unfocused water truck moving at 8.9 m/s (20mi/h). The image is displayed as the square root of magnitude.

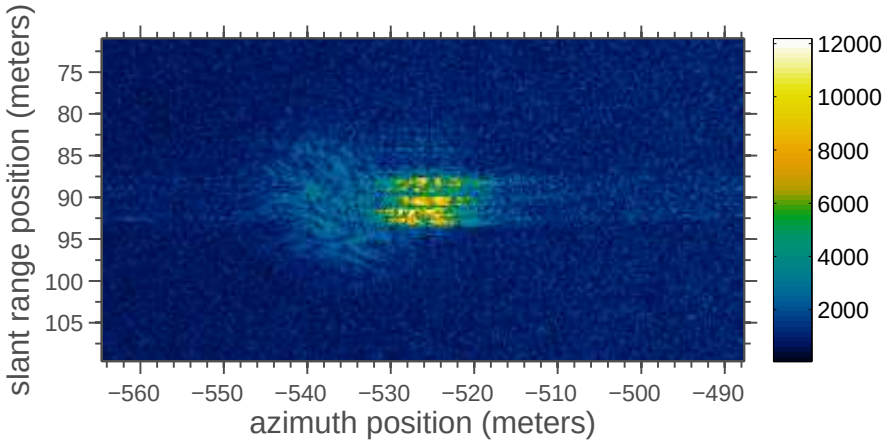

Figure 3.13: A water truck moving at 8.9 m/s (20mi/h) focused with the MITRE keystone technique. The images is displayed as the square root of magnitude.

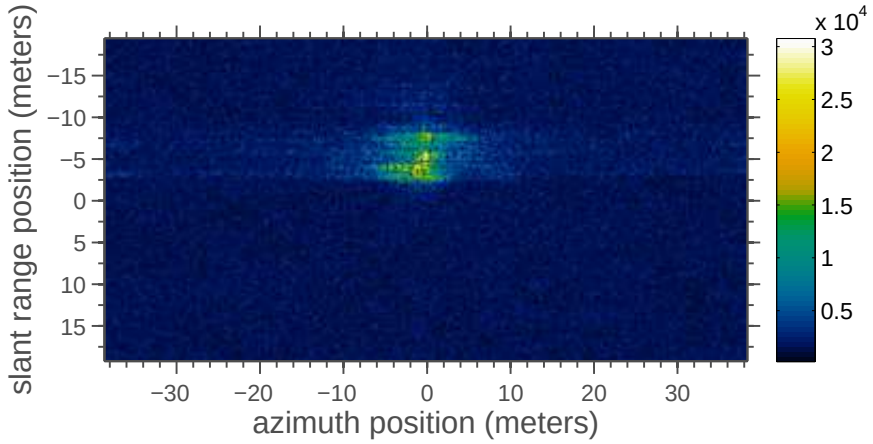

Figure 3.14: A water truck moving at 8.9 m/s (20mi/h) focused and located with the new proposed method. The images is displayed as the square root of magnitude.

Chapter 4

Detection of a moving target using a single phase center

The previous chapter presented a novel method to locate, focus, and estimate velocity vectors for moving targets in a SAR scene. However, this method assumes the presence of a radar system with multiple phase centers (either monopulse or along-track interferometry). The information provided by having multiple phase centers is used both to detect a target and to determine angle of arrival information that can be used to locate the target in azimuth. This chapter presents a method to detect an endo-clutter target with a single phase center.

This detection method is an extension of a method first proposed by Fienup [18] that detects targets through the quadratic and higher order phase errors generated by target motion (in particular, azimuth velocity and range acceleration). The method is made more robust through the application of the MITRE keystone remapping technique prior to detection, and is extended to handle detection of endo and exo-clutter targets as well as targets whose range velocity has caused the target energy to alias. First, theoretical performance of this detection technique is examined. The performance of the extended method

is then compared to the original technique as proposed by Fienup. Finally, the minimum detectable velocity for aliased and unaliased endo-clutter targets in a variety of clutter levels is examined.

4.1 Background and Related Work

Traditionally, moving target indication (MTI) has been performed using radar systems with multiple phase centers. However, there are several distinct advantages in being able to use a SAR-GMTI based system including the ability to use existing sensors and simplified modes of operation. Traditional GMTI systems can only identify targets moving faster than the minimum detectable velocity. A combination SAR-GMTI system would be able to overcome that limitation by having the ability to image targets that are stationary or moving below the minimum detectable velocity. Ideally, a SAR-GMTI approach would be able to work with a single phase SAR system. This is both because many existing SAR systems contain only a single phase center and the cost of developing and deploying a single phase center SAR system is significantly reduced from the cost of a multi-channel system. In a single phase center system there is no need to calibrate the returns from multiple phase centers, and the ease of processing is likewise reduced.

Kirscht [26] proposes a technique that forms a sequence of images centered at different times along a SAR collection. In these images the SAR ground clutter remains stationary, but the position of the moving targets change. He detects this change, estimates the velocity of the moving targets,

applies a correction, and then verifies that the detection was truly a moving target.

Minardi *et. al* [29] describe a method which uses a concept called a SAR-MTI detection cube. First, they refactor the standard SAR geometry so that targets can be uniquely identified and focused by three parameters: the range at the point of closest approach (R_{pca}), the time at the point of closest approach (T_{pca}), and the magnitude of the relative velocity between the mover and the sensor ($v_{relative}$). Images, which are slices of the SAR-MTI detection cube, are then formed along fixed $v_{relative}$. This is similar to the formulation described by Soumekh in several of his papers and books [40–42]. Targets will be focused in the image with the correct $v_{relative}$ and can be detected by examining the various slides of the SAR-MTI detection cube. There are several issues related to this approach. One large issue is that this technique can not solve the issue typically described as the azimuth ambiguity problem [28, 39]. That is, multiple targets can share a T_{pca}, R_{pca}, and $v_{relative}$ triplet - nothing in this approach prevents a collision. Furthermore, even if a target has a unique triplet there is no means to determine its true velocity vector. This approach also relies on the assumption that the target motion is linear. It was shown in 2.4.3 that depending on geometry, a very small amount of non-linear motion (range acceleration) can cause the equivalent blurring of a large amount of linear motion (azimuth velocity). Finally, even if the assumption of purely linear motion holds true, it is not readily apparent how the position of an unfocused target in an uncompensated SAR image can be determined.

This position is necessary to apply further processing such as the technique developed in chapter 3.

Fienup [18] describes a method to identify moving targets in a SAR scene based on the effects of azimuth velocity and range acceleration. His technique works by segmenting the SAR system into a number of small patches. He uses an autofocus technique - shear averaging - to correct for phase errors in each small patch. He then compares the focused patch to the patch before focusing through the use of a sharpness metric. The main limitation of this approach is that it fails to identify targets whose motion is constrained to linear range migration. Here I present an overview of his method, followed by an extension that exploits the ability of the MITRE keystone technique to compensate for linear range migration to improve the detection of targets with arbitrary velocity vectors.

The detection method through focusing proposed by Fienup has several distinct advantages. Unlike other detection techniques, the focusing method does not perform a search over a large state space of possible velocities. Because the state space of possible target positions and velocities can become very large many detection methods neglect the possibility of non-linear motion. However, non-linear motion (particularly range acceleration) actually increases the performance of the focusing method because this non-linear motion causes phase errors that decrease sharpness. The focusing algorithm must be capable of detecting and correcting for higher order phase errors. This necessitates the use of a modern autofocus technique (shear averaging or phase

gradient autofocus) rather than an older autofocus technique such as map-drift that assumes the error is quadratic [4, 6].

There are several limitations in the focusing technique as described by Fienup. He does not address exo-clutter targets nor the application of the focusing technique to targets that have aliased. The example data used in his paper was 708 pulses collected over 0.472 seconds from the MIT Lincoln Laboratory ADTS Ka-Band (33.56 GHz) SAR [21, 30]. Those specifications yield a PRF of 1500Hz and a wavelength $\lambda = 8.9mm$. This means that the minimum aliasing velocity $V_{alias} = 3.35$ m/s (7.5 mi/h) (2.20). A target at the scene center with a range component of velocity greater than v_{alias} will alias and be undetectable. The other limitation is that most autofocus techniques are designed to handle phase errors that are constrained to a single range bin. Azimuth velocity or range acceleration cause range walk which spreads the target energy in multiple range bins and can interfere with proper autofocus behavior 2.5. Finally, Fienup does not attempt to locate a target in a patch once the patch has been flagged as containing a target.

4.2 Proposed method

Fienup forms a SAR image by simply performing an azimuth Fourier transform on range-compressed pulses. This is a good approximation for a matched filter near the scene center, depending on the type of motion compensation that has been applied to the data, but the image will be increasingly smeared as the distance from the center increases. The amount of smearing

caused by a simple Fourier transform versus performing polar formatting will depend on specifics of the SAR collection parameters, and is perfectly acceptable in some cases (as shown by the results obtained by Fienup). Jakowatz [47] gives the maximum patch size D_{max} that can be processed by a direct 2-D Fourier transformation as:

$$D_{max} \leq 4\frac{\rho_x \rho_y}{\lambda} \tag{4.1}$$

where ρ_x and ρ_y are the azimuth and range resolutions of the scene, respectively. In cases where this patch size limit is exceeded the technique can be applied to data processed with a more sophisticated technique such as polar re-formatting. However, I instead propose the use of the MITRE keystone technique. The MITRE keystone technique, in addition to correcting for linear range migration, also removes the effects of range walk caused by range acceleration and azimuth velocity (Section 2.5). In addition, it is possible to focus aliased targets with the keystone method through the use of a fold factor [18].

Furthermore, I propose using an increased PRF and the use of thresholding to detect exo-clutter targets while simultaneously using focusing of MITRE keystone formatted patches to detect endo-clutter targets. The keystone technique is performed with multiple fold factors to handle targets with a range velocity greater than V_{alias}. The position of targets that are detected in exo-clutter is determined with a center of mass calculation on image intensity. For unaliased targets in endo-clutter I take advantage of the high PRF

and form a multi-look image to drive down clutter before attempting to locate the target using a center of mass calculation. Once the correction factor has been applied to a target that had previously been aliased, the clutter is instead aliased and smeared out. This provides an advantage to detection of the target position.

The SAR image is first segmented in a set of patches. Each patch is processed with auto-focus to attempt to focus any potential moving targets in the image. The sharpness of the patch pre and post-autofocus is compared to determine if the sharpness of the patch has increased after this focus attempt. Fienup used an autofocus technique (shear averaging [17]) to correct for motion induced errors. The simulation performed here uses a similar autofocus technique known as phase gradient autofocus [49]. For an optimal increase in sharpness, the patch size should just encompass the moving target. As the moving target will primarily be smeared in azimuth, the patch size in range should be just larger than the anticipated size of the focused target. However, the number of range lines should be sufficient to allow proper operation of the autofocus algorithm. The optimal azimuth patch size will be dependent on the azimuth velocity of the moving target. Here I use a patch size of 16 pixels in range by 128 pixels in azimuth. Special care must be taken to handle targets that are smeared across multiple patches and targets that are located at or near the edge of patches. As discussed in Fienup [18] the SAR scene can be processed multiple times with varying azimuth patch lengths or patches that overlap in azimuth to increase the likelihood of detection. There is also a

possibility of false alarms from objects that have phase responses that appear similar to a smeared moving target. If the energy in the patch is dominated by an object that is constrained in range but spread out in azimuth the autofocus algorithm may erroneously collapse the energy from that object to a single azimuth pixel. The return from a curb near the side of a road, railroad tracks, or the edge of a building are all targets that may cause false alarms if oriented appropriately.

4.2.1 Sharpness Metrics

Fienup [18] defines two sharpness metrics. The first metric used to estimate the magnitude of the phase-error is its standard deviation which he defines as:

$$f_1 = \sigma_{rms} = \sqrt{M^{-1} \sum_m \sigma^2 (m) - \left(M^{-1} \sum_m \sigma (m) \right)^2} \tag{4.2}$$

Where $\sigma(m)$ is the phase-error estimate for the image patch for the mth azimuth sample after subtracting the linear component of the phase-error estimate. He also defines a sharpness ratio based on the first of the Muller-Buffington image-sharpness metrics ($\mathbb{S}_1$) [31] which is given as:

$$\mathbb{S}_1 = \int I^2 (x, y) \, dxdy \tag{4.3}$$

where I(x,y) is the image irradiance and x,y are coordinates in the image plane. In SAR the irradiance can be considered to be image intensity, and this

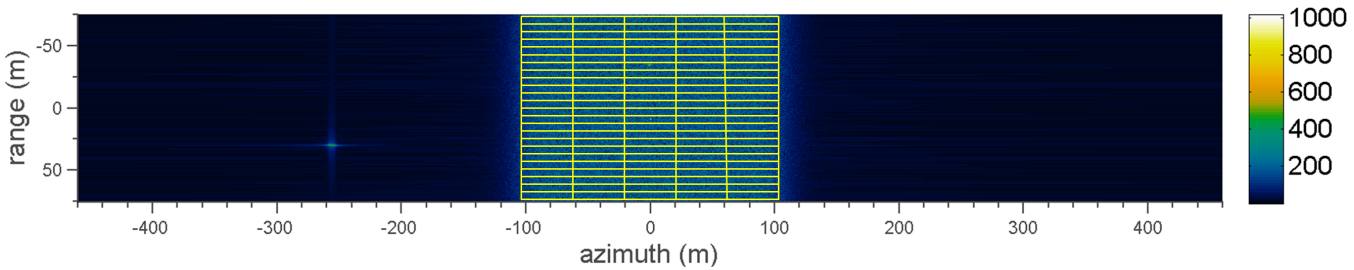

Figure 4.1: Segmented patches of a SAR image.

equation can be rewritten as:

$$\mathbb{S}_1 = \sum_{x,y} |I(x,y)|^4 \tag{4.4}$$

From definition of $\mathbb{S}_1$ the sharpness ratio is then defined as:

$$f_4 = \frac{\mathbb{S}_1(corrected)}{\mathbb{S}_1(uncorrected)} = \frac{\sum_{x,y} |I_{corrected}(x,y)|^4}{\sum_{x,y} |I_{uncorrected}(x,y)|^4} \tag{4.5}$$

where $I_{uncorrected}$ is the complex image before phase-error correction and $I_{corrected}$ is the complex image afterwords. Fienup [18] found experimentally that a f_4 sharpness metric of greater than 2 was a reliable indication of a moving target. This f_4 threshold was also observed in these simulated results.

4.3 Simulation

Spotlight mode synthetic radar data was generated based on the parameters suggested in Jakowatz [47]. These parameters represent an X-band radar system (10GHz) with range and azimuth resolutions of approximately 0.375m. The pulse repetition frequency was modified from the suggested 163.5 Hz to 1000Hz to provide an exo-clutter region for the detection of moving targets (Table 4.1). Zero mean gaussian clutter, band-limited to the endo-clutter region, was applied to the simulated targets.

4.3.1 Performance improvement of the modified technique

A monte carlo simulation of 500 point targets with random initial positions and range and azimuth velocities was performed. The focusing technique

Table 4.1: Radar parameters: synthetic data

Phase center velocity	500 m/s
Phase center elevation	15000 m
Slant plane squint angle	-1.17 to 1.17 deg.
Depression angle	30 deg.
Radar center frequency	10 GHz
Radar BW	401.50 MHz
Linear FM chirp rate	1.0×10^{12} Hz/s
PRF	1000 Hz
Sample rate	1 GHz
Range	30000 m
Flight distance	1225.1 m
Number of pulses	2450
Number of samples per pulse	400

was applied using both polar formatting and the keystone technique. The initial positions and range velocities were selected to avoid target aliasing. The target positions were selected from -20 to 20m in range and -70m to 70m in azimuth. The range velocities were selected between -5 m/s and 5 m/s, and the target azimuth positions were selected from between 0.5m/s and 20m/s. The targets were detectable by both techniques in all cases. The new technique showed a modest average improvement in the f_4 metric of 5.2% over the method as proposed by Fienup.

4.3.2 Minimum detectable azimuth velocity

Azimuth velocity induced quadratic phase error results in the target energy being spread roughly equally over $2v_a\tau\rho_a$ where ρ_a is the azimuth resolution of the focused scene (Section 2.4.2). The optimum increase in sharpness will be equal to the number of pixels over which the energy is spread. This means that the minimum detectable azimuth velocity m_v can be found as:

$$m_v = \frac{T\rho_a}{2\tau} \tag{4.6}$$

where T is the threshold used to indicate a mover. With a reasonable value of $T = 2$ the minimum detectable azimuth velocity for this simulated data should be 0.1513 m/s. However, this minimum detectable velocity will be increased by the presence of noise.

Point targets were simulated moving in azimuth from -30 to 30 m/s (-67 to 67mi/h) in 0.5 m/s increments and from -5 to 5 m/s (-11.2 to 11.2 mi/h) in 0.1 m/s increments to determine a more reasonable minimum velocity. These targets were placed over uniform clutter with target/background ratios of 0.05, 0.1, 0.5, 2, and 10 (-26, -20, -6, 6, and 20dB respectively). With the parameters used for this simulation a perfectly focused point target would receive an increase a final signal-to-clutter ratio (SCR) of approximately 52dB greater than the initial target/background ratio due to the gain from SAR processing. Targets were simulated with no range velocity and with range velocities of 17m/s and 35m/s (aliased completely into the endo-clutter region once and twice respectively).

The induced quadratic phase increases as the azimuth velocity increases. This means that the number of pixels over which the target energy is spread out also increases. If the focusing algorithm works perfectly all this energy will be put into a single pixel after the phase correction is applied. Thus, in the absence of clutter, a higher velocity will cause a higher f_4 sharpness metric. However, as the quadratic phase increases the initial target to clutter ratio before focusing decreases. The clutter will then contribute more to the phase-error estimate generated by the auto-focus routine. When these two effects are combined the f_4 ratio should initially increase as azimuth velocity increases, but will start to decrease as the target energy becomes more spread out and is overcome by the clutter power.

The minimum detectable velocity for the unaliased target was 0.3 m/s with all SCR levels (Fig. 4.2). However, as the velocity increased above 5 m/s for a -26dB SCR and 15 m/s for a -20dB SCR the target was not constantly detected. The target was constantly detected for all other SCR at any azimuth velocity greater than 0.3 m/s.

The performance of the algorithm was slightly degraded when the target was aliased completely once. A slightly higher minimum velocity of 0.6 m/s was required for reliable detection (Fig. 4.4). The target was not constantly detected with -26dB SCR. The target was not consistently detected above 18 m/s with a -20dB SCR (Fig 4.5). The target was again constantly detected for all other SCR at any azimuth velocity greater than 0.6 m/s.

The twice aliased target required a substantially higher minimum az-

imuth velocity to be reliably detected of approximately 3 m/s (Fig. 4.6). The targets with -26 and -20dB SCR levels were not reliably detected (Fig. 4.7). The target was consistently detected for all other SCR with an azimuth velocity greater than 3 m/s.

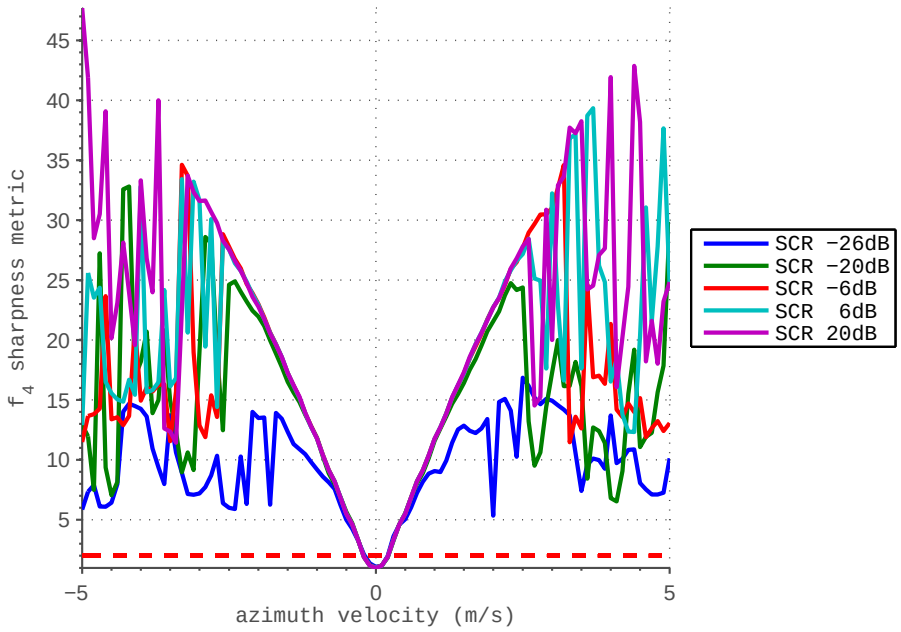

Figure 4.2: The f_4 sharpness metric for an unalised point target at the scene center with various simulated clutter levels versus azimuth velocity (-5 m/s to 5 m/s).

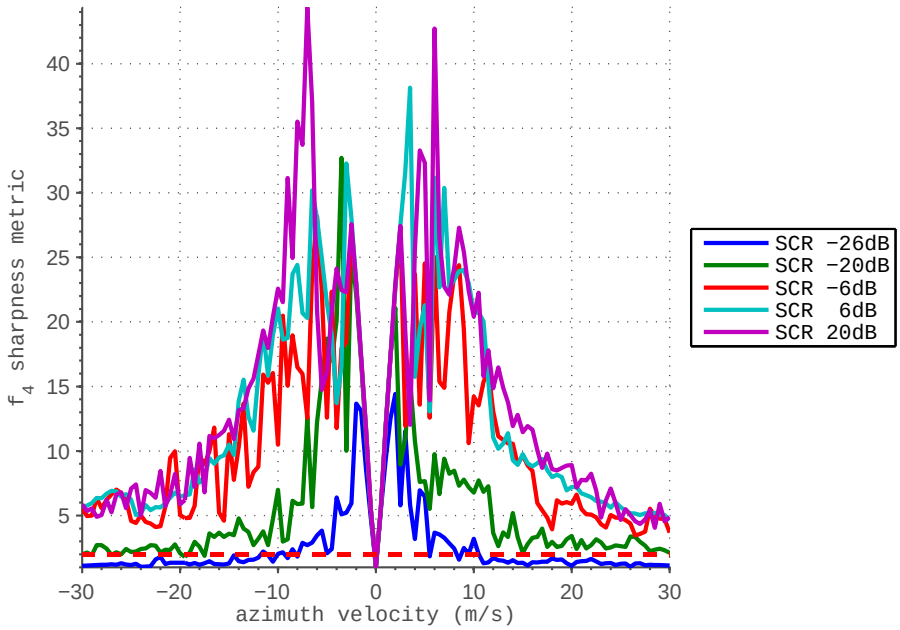

Figure 4.3: The f_4 sharpness metric for an unalised point target at the scene center with various simulated clutter levels versus azimuth velocity (-30 m/s to 30 m/s).

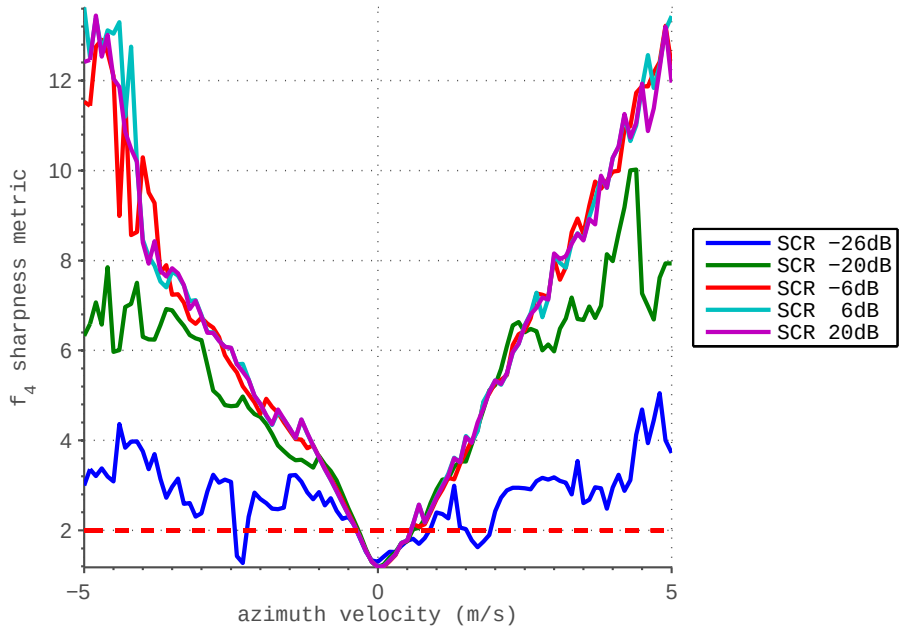

Figure 4.4: The f_4 sharpness metric for an aliased point target at the scene center with various simulated clutter levels versus azimuth velocity (-5 m/s to 5 m/s).

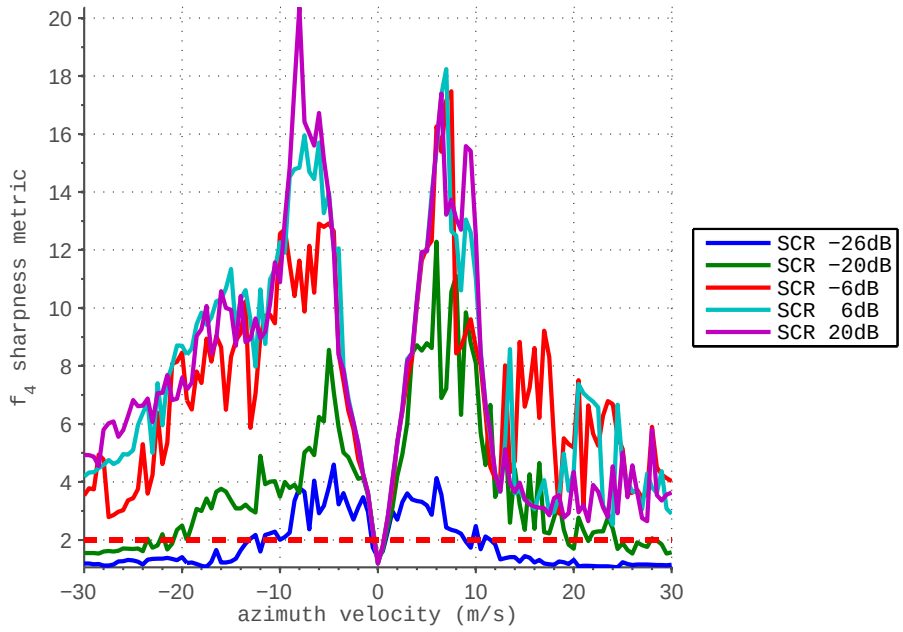

Figure 4.5: The f_4 sharpness metric for an aliased point target at the scene center with various simulated clutter levels versus azimuth velocity (-30 m/s to 30 m/s).

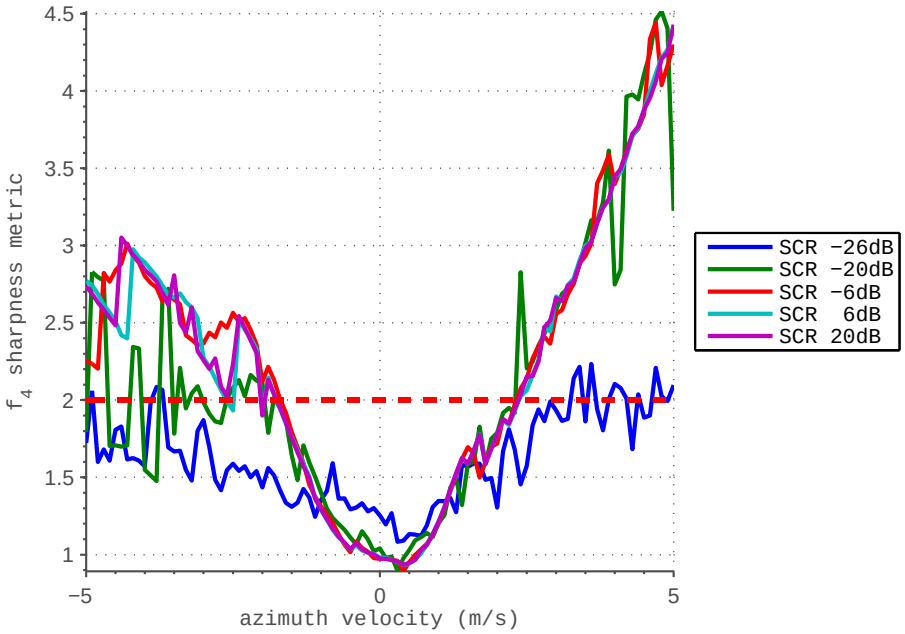

Figure 4.6: The f_4 sharpness metric for a twice aliased point target at the scene center with various simulated clutter levels versus azimuth velocity (-5 m/s to 5 m/s).

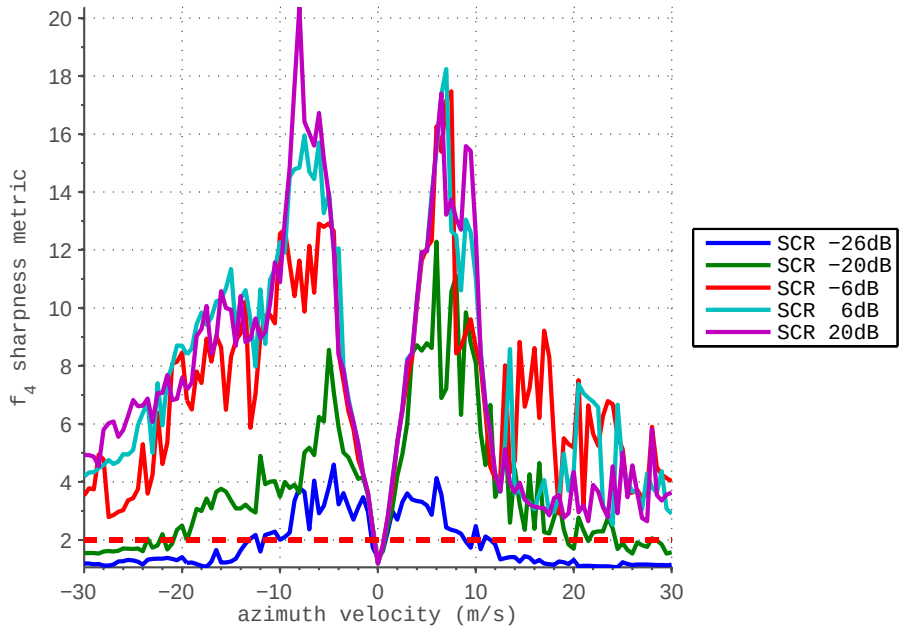

Figure 4.7: The f_4 sharpness metric for a twice aliased point target at the scene center with various simulated clutter levels versus azimuth velocity (-30 m/s to 30 m/s).

4.3.3 Multiple target detection example

A simulated SAR scene with multiple point targets was generated to fully demonstrate the application of this detection technique. The scene consists of three endo-clutter targets and one exo-clutter target (Fig. 4.8). The target velocities were selected so that the endo-clutter targets would be unaliased, aliased once, and aliased twice respectively. The exo-clutter target is not aliased. Another way to consider these aliased targets are as targets that would be exo-clutter targets if the PRF of the scene was sufficiently high. Images of the full SAR scene (Fig. 4.9,4.12,4.15,4.18, and 4.21) and endo-clutter only portions of the SAR scene (Fig. 4.10,4.13,4.16,4.19, and 4.22) were generated with MITRE keystone remapping applied with a fold factor of -2, -1, 0, 1, and 2 (to correct for targets that had aliased). Detection results were also generated for all five cases (Fig. 4.11,4.14,4.17,4.20, and 4.23). All four targets were successfully detected and image patches showing the target were created (Fig. 4.24,4.25,4.26, and 4.27). The fourth target was detected using amplitude threshold as the target was located in the exo-clutter region (Fig. 4.27). The clutter level was set to provide a signal to clutter level of -23dB for a single point target (29dB signal to noise ratio for a fully focused point target). However, the aliased targets also contributed to the noise levels of other targets.

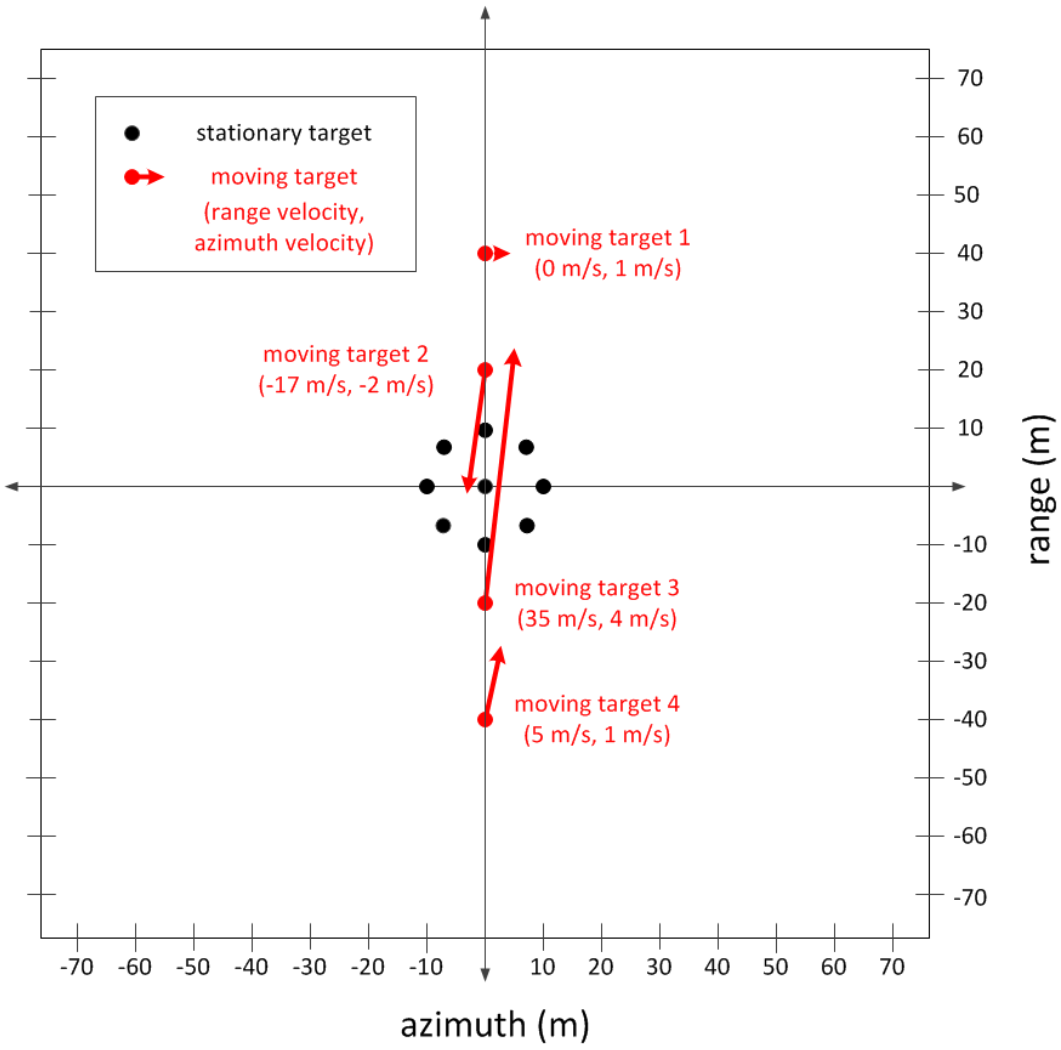

Figure 4.8: This diagram shows the position and velocities for point targets used in the multiple target detection simulation. Targets 1–3 are endo-clutter targets, while the parameters for target 4 were selected to cause the target energy to shift into the exo-clutter region.

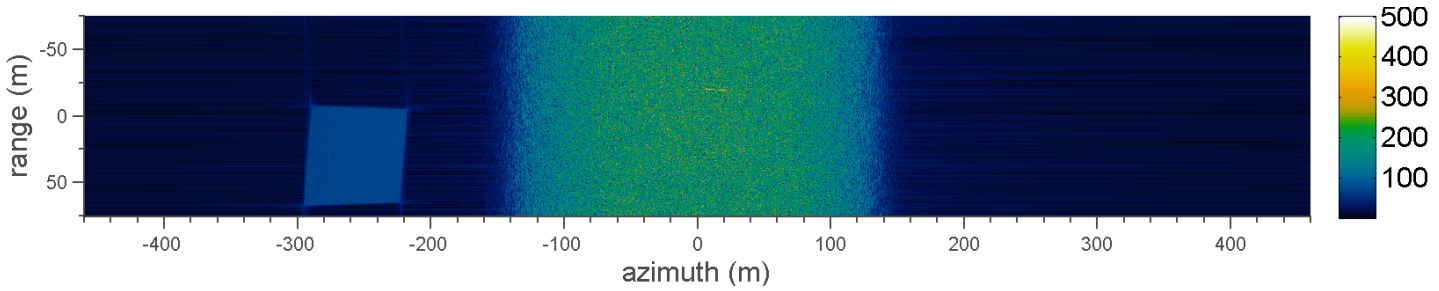

Figure 4.9: The full SAR scene focused the MITRE keystone method using a fold factor of -2. The image is displayed as the square root of magnitude.

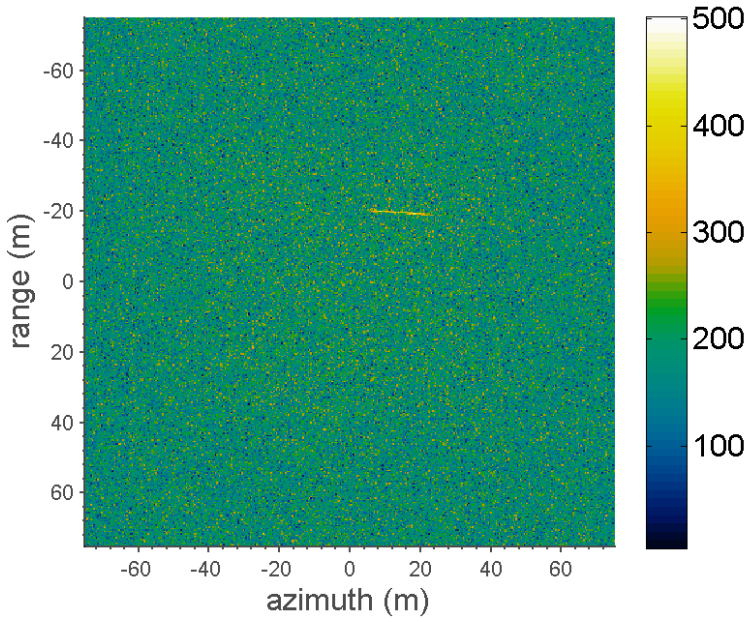

Figure 4.10: The endo-clutter SAR scene focused the MITRE keystone method using a fold factor of -2. The image is displayed as the square root of magnitude.

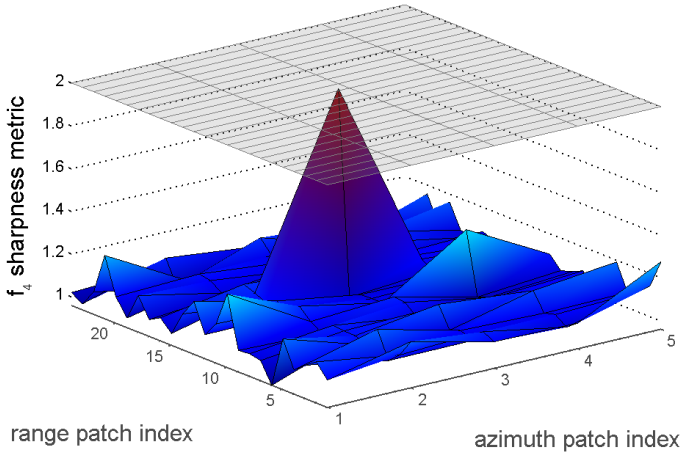

Figure 4.11: Detection results for endo-clutter targets using a fold factor of -2.

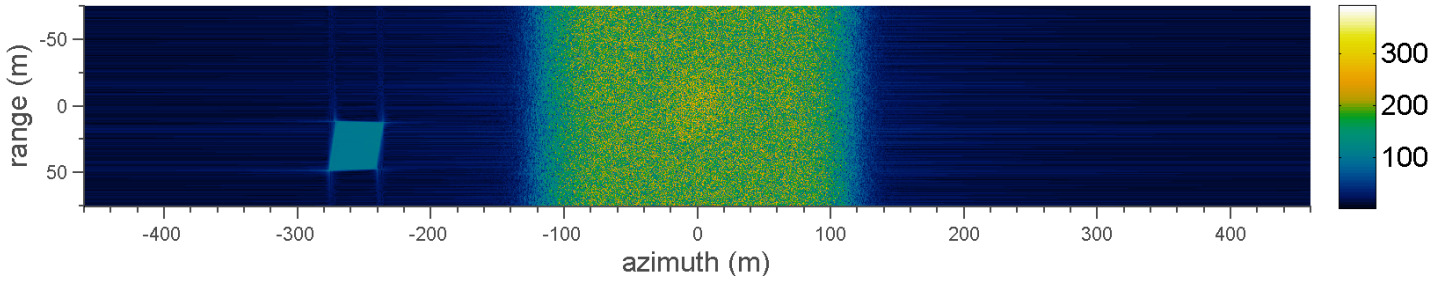

Figure 4.12: The full SAR scene focused the MITRE keystone method using a fold factor of -1. The image is displayed as the square root of magnitude.

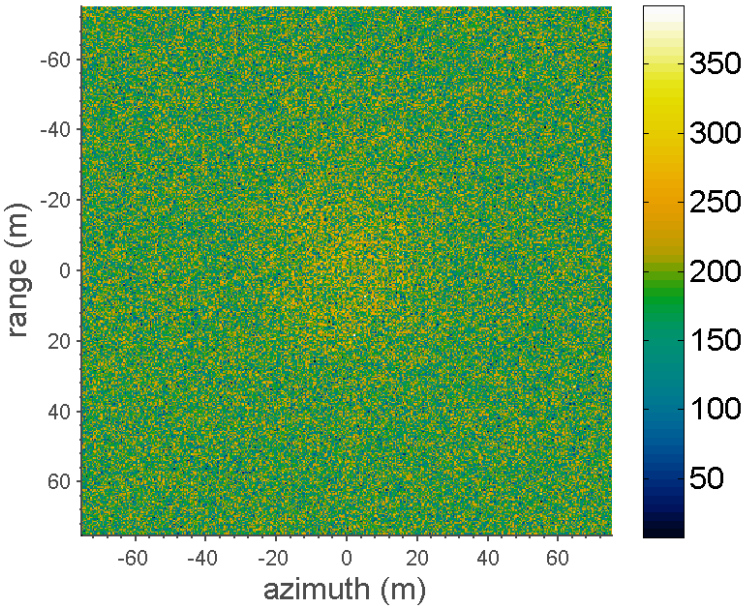

Figure 4.13: The endo-clutter SAR scene focused the MITRE keystone method using a fold factor of -1. The image is displayed as the square root of magnitude.

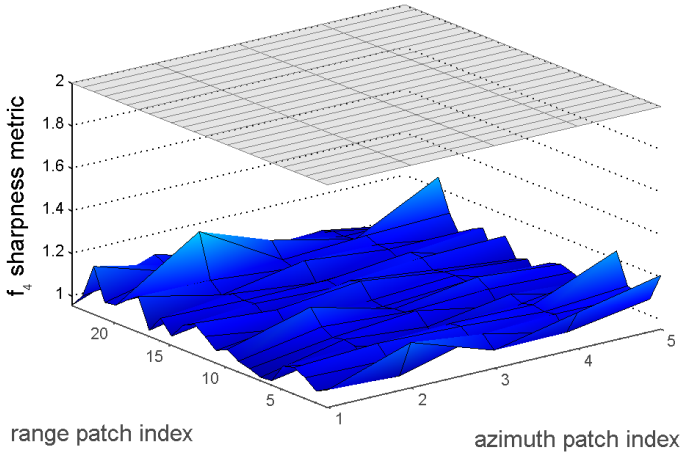

Figure 4.14: Detection results for endo-clutter targets using a fold factor of -1.

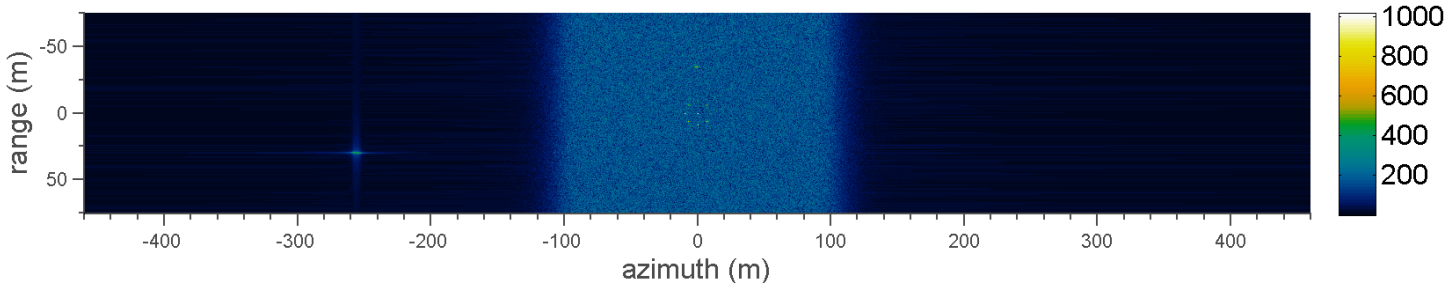

Figure 4.15: The full SAR scene focused the MITRE keystone method. The image is displayed as the square root of magnitude.

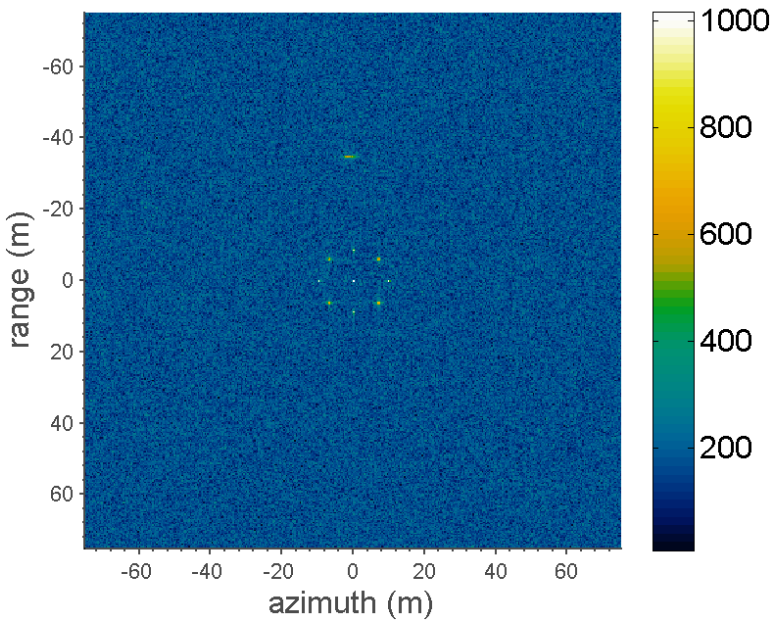

Figure 4.16: The endo-clutter SAR scene focused the MITRE keystone method. The image is displayed as the square root of magnitude.

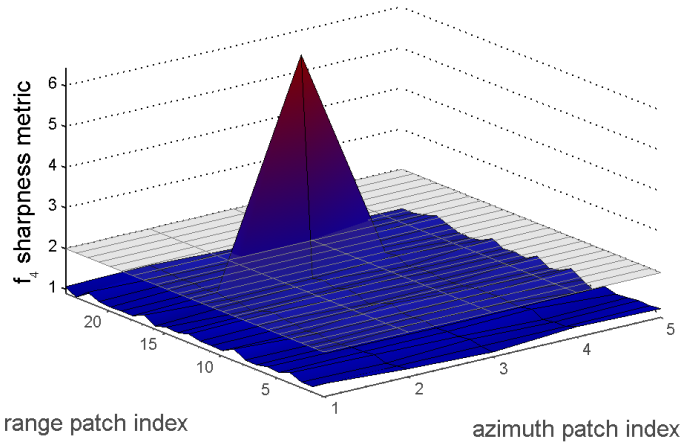

Figure 4.17: Detection results for endo-clutter targets.

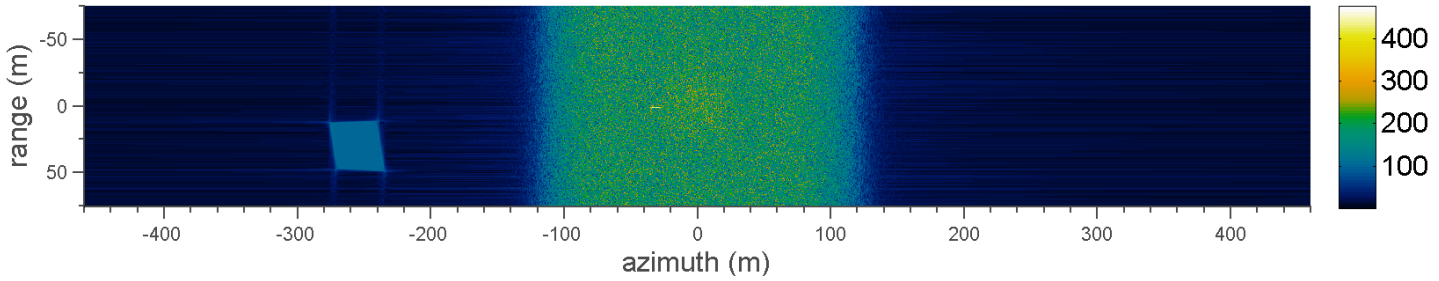

Figure 4.18: The full SAR scene focused the MITRE keystone method using a fold factor of 1. The image is displayed as the square root of magnitude.

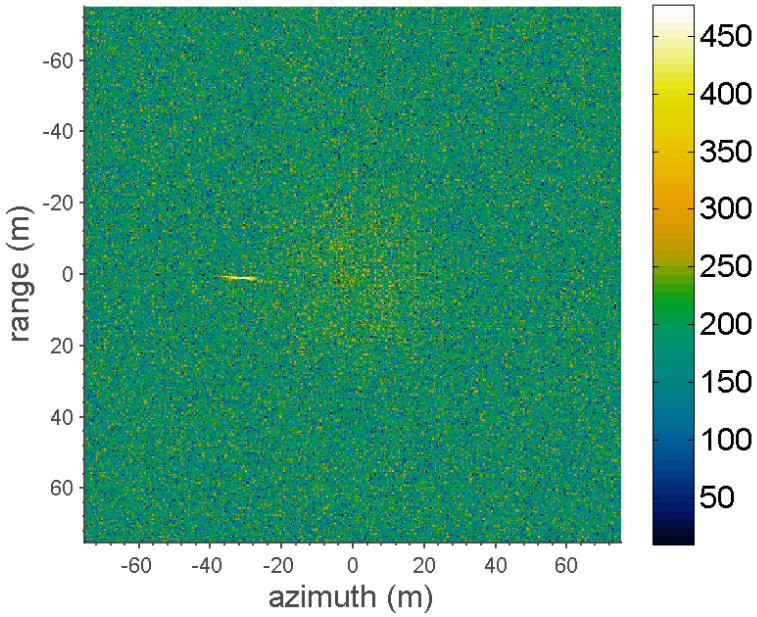

Figure 4.19: The endo-clutter SAR scene focused the MITRE keystone method using a fold factor of 1. The image is displayed as the square root of magnitude.

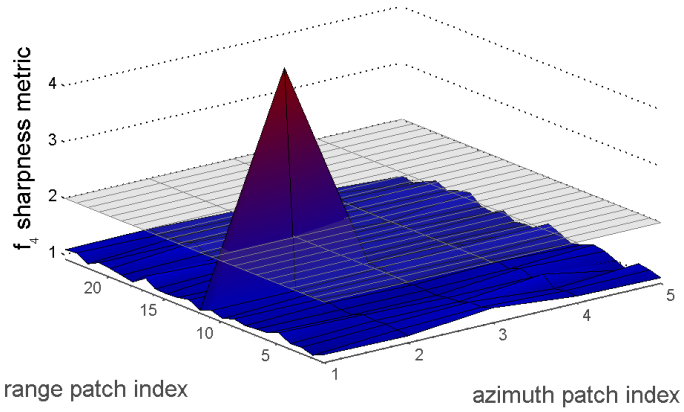

Figure 4.20: Detection results for endo-clutter targets using a fold factor of 1.

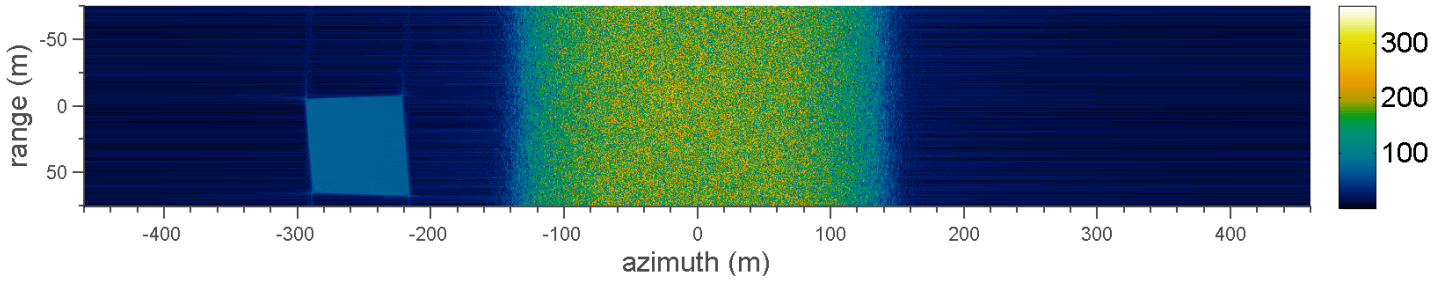

Figure 4.21: The full SAR scene focused the MITRE keystone method using a fold factor of 2. The image is displayed as the square root of magnitude.

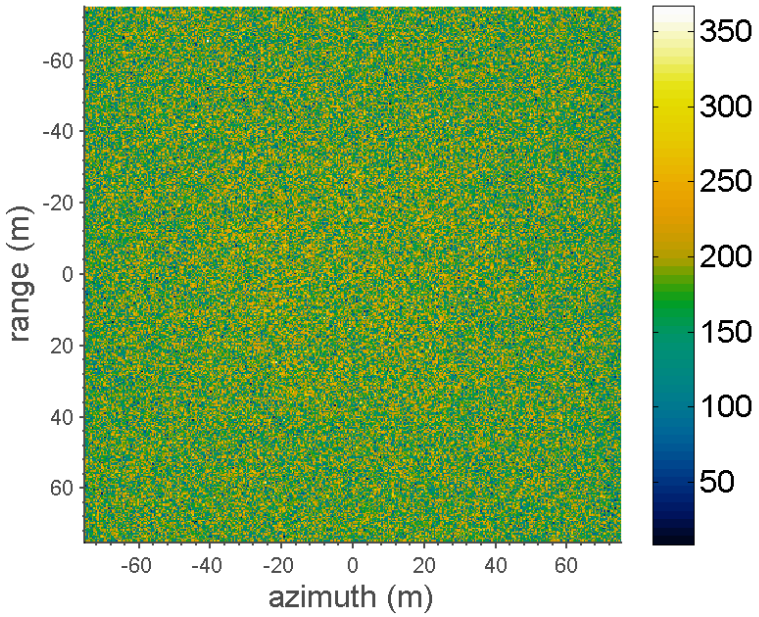

Figure 4.22: The endo-clutter SAR scene focused the MITRE keystone method using a fold factor of 2. The image is displayed as the square root of magnitude.

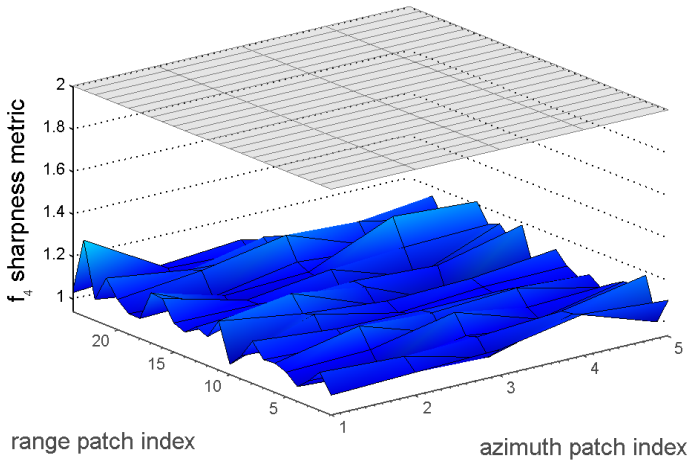

Figure 4.23: Detection results for endo-clutter targets using a fold factor of 2.

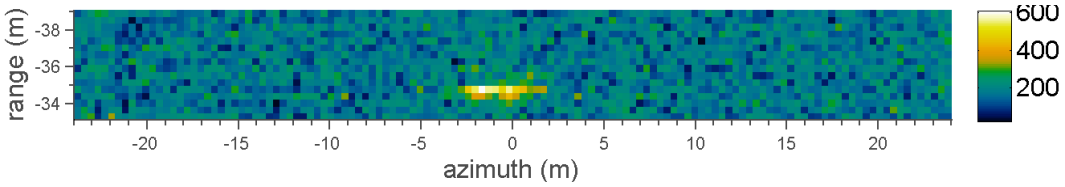

Figure 4.24: A detected moving target (target 1) located 40m in range from the scene center moving 1 m/s in azimuth.

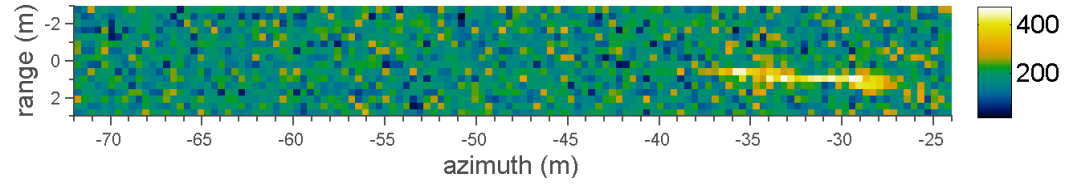

Figure 4.25: A detected moving target (target 2) located 20m in range from the scene center moving at -17 m/s in range and -2 m/s in azimuth.

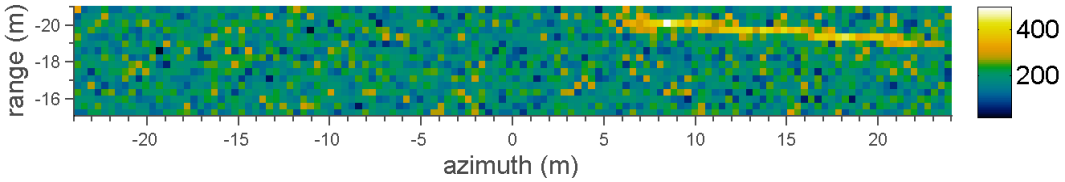

Figure 4.26: A detected moving target (target 3) located -20m in range from the scene center moving at 35 m/s in range and 4 m/s in azimuth.

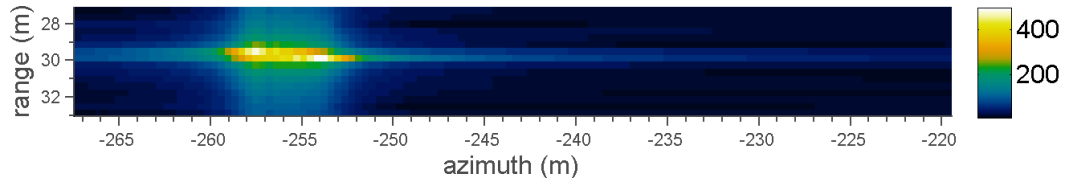

Figure 4.27: A detected moving target (target 4) located -40m in range from the scene center moving at 5 m/s in range and 1 m/s in azimuth.

4.4 Conclusion

This chapter demonstrated a technique to locate targets using a single phase center antenna. This technique does not rely on searching through a large state space of possible target velocities. This technique is more robust than those relying simply on estimated phase-errors as the f_4 sharpness metric used measures increased sharpness. As demonstrated here, this modified focusing technique can handle both endo and exo-clutter targets including those that have aliased. In combination with this detection method, the only additional information needed to perform the novel technique for locating, focusing, and estimating velocity for a moving target discussed in chapter 3 is the true azimuth position of a moving target. The next chapter will discuss using *a priori* knowledge of the radar scene to determine the true azimuth position of the target.

Chapter 5

Knowledge-based focusing of a moving target

The previous chapter presented a method to detect a moving target in a SAR scene generated from a single phase center. A target detected with this method can still not be processed with the method developed in chapter 3 as that method also requires information about the true azimuth location of the target. It is generally believed that information about the true azimuth location of the target cannot be determined for a moving target in a SAR image using a single phase center. Barbarossa refers to this as the *azimuth position uncertainty problem* [1] whereas Soumekh refers to this ambiguity as the *blind angle* [39, 41]. Dias and Marques claim to be able to solve the azimuth position uncertainty problem, at least for stripmap SAR, through knowledge of the antenna radiation pattern [12]. It appears that their technique is an attempt to perform monopulse processing with a single phase center. It is unclear to this author how their proposed technique would perform on real data, but in any event does not appear to be readily extendable to spotlight mode data.

This chapter reviews sources of *a priori* knowledge about the SAR scene that can be used to solve for the true azimuth position of a moving

target. The primary method covered is the use of road knowledge to locate a target. However, given *a priori* information about the nature of a target, micro-Doppler and target orientation in a semi-focused target may also be used to locate a target. The azimuth position uncertainty problem can be thought of as an inability to determine the true azimuth position of a target, but it is equally valid to consider the problem as an inability to determine the true range velocity of the target. This is because the position of the target energy in a scene is dependent on both true azimuth position and range velocity. Once either parameter is determined the other can be calculated as well.

5.1 Geometric dilution of precision

Geometric dilution of precision (GDOP) is a term typically seen in discussions on global positioning satellite (GPS) systems. In GPS systems GDOP is a quantity that is calculated to characterizes the uncertainty caused by a specific satellite geometry [55]. Here I abuse notation slightly by using GDOP to refer to the general description of how the position uncertainty of a target that is being located with multiple ranging sensors depends not only on the accuracy of the sensors but also on their geometry. If the sensors are orthogonal there is a low position uncertainty, but as they move further away from being orthogonal the uncertainty increases (Fig. 5.1).

The concept of GDOP comes into play for SAR imaging when considering the possible squint angles used in a collection. The allowable squint angles for specific radar system are typically known as the *field of regard*. These ac-

ceptable squint angles are typically between 45° and 135° (or −45° and −135°) for SAR imaging modes (Fig. 5.2). For GMTI modes, determining the precise azimuth position of a target is often not as important as the ability to detect the target. If the antenna phase center is oriented along the flight path of the aircraft straight ahead (0°), or behind (180°) the Doppler frequency response for the clutter (the endo-clutter region of the range-Doppler map) will collapse approximately to the vertical axis. In practice, there will be a slight slope to the expected clutter line as the grating angle for far targets is shallower than that of near targets and thus the rate of approach is greater for far targets. The range-Doppler map can be normalized with respect to grating angle to make the expected clutter line vertical. The properties of GMTI clutter has been covered by Doerry at length ([13, 14]). Any deviation from the expected clutter line will be a result of target motion. This is one method of solving the azimuth position uncertainty problem, but at the expense of removing the ability to simultaneously form a SAR image. However, by tracking a target across several coherent processing intervals it is possible to detect a target at a squint angle that orients the antenna phase center along the flight path and determine its range velocity before changing the squint angle to one more conducive for SAR imaging - assuming the target maintains approximate course and speed.

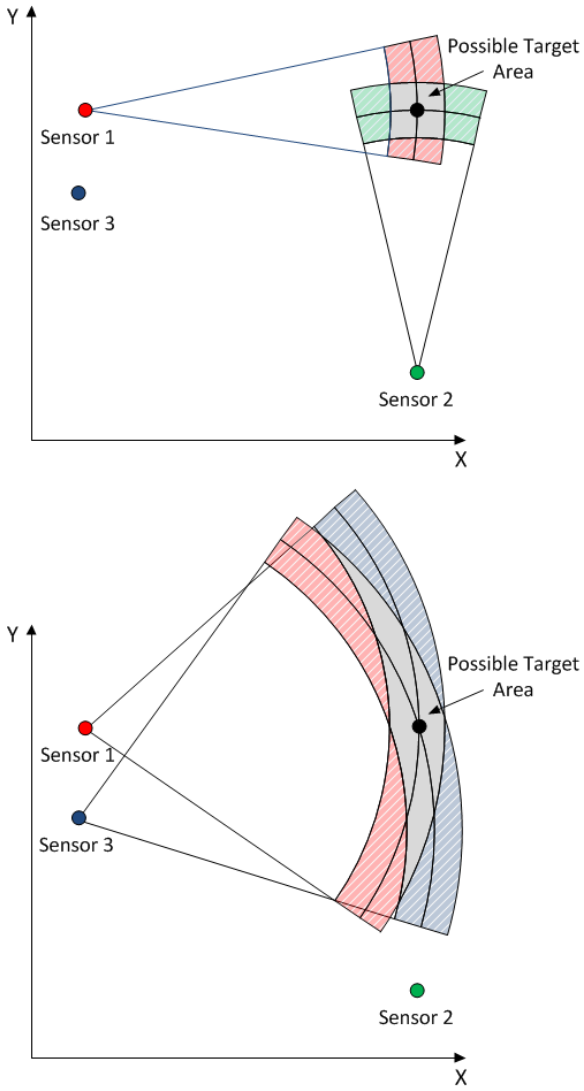

Figure 5.1: The position uncertainty of a target being positioned with two sensors depends not only on the error of the sensors but also on the geometry. If two ranging sensors are orthogonal there is a low position uncertainty, but as they move further away from being orthogonal the uncertainty increases. Here an example of this effect is seen which is known as *geometric dilution of precision*.

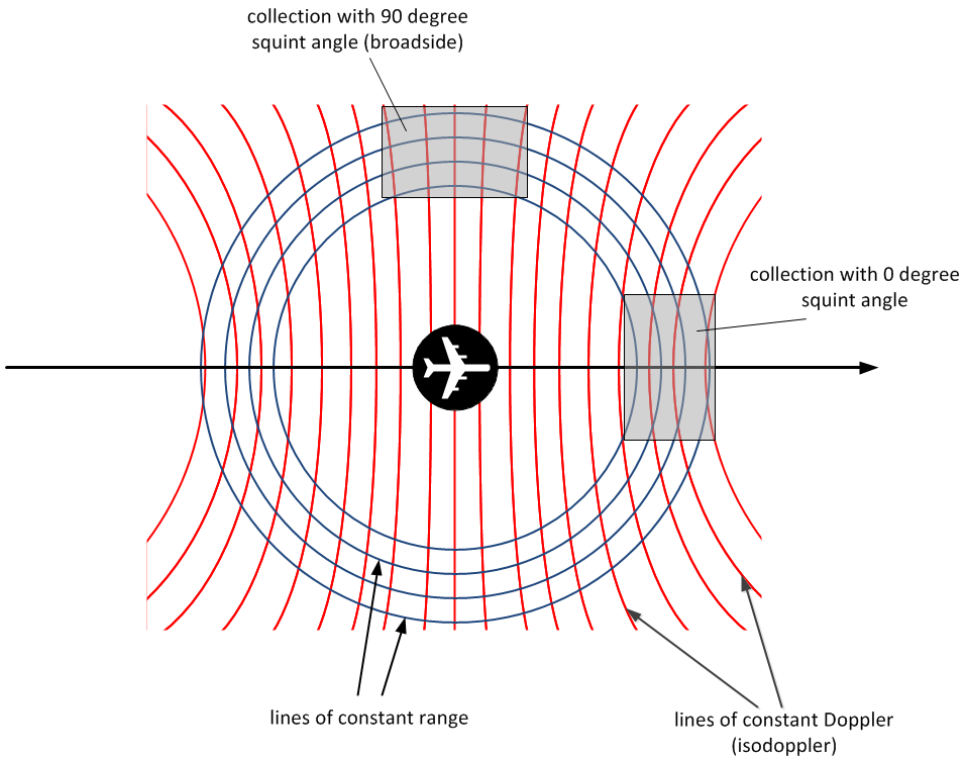

Figure 5.2: This figure shows typical lines of constant range and constant Doppler from a antenna phase center mounted on an aircraft. The lines of constant range and constant Doppler are orthogonal at at squint angle of 90° (broadside), but parallel at 0°.

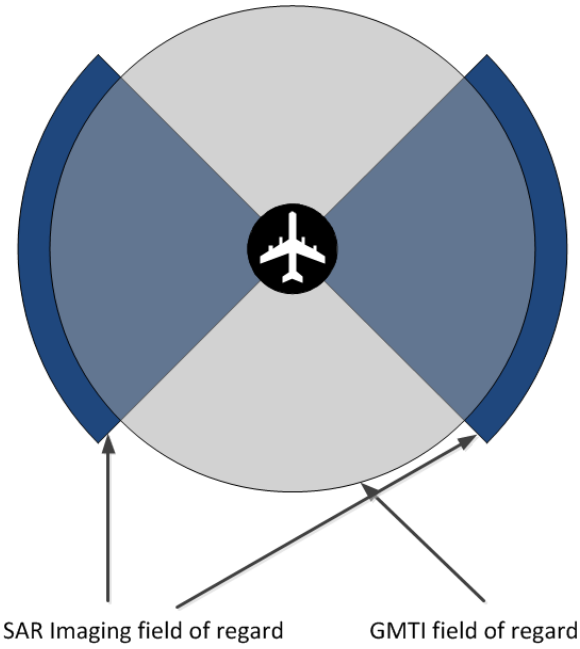

Figure 5.3: Typical fields of regard for SAR imaging and GTMI modes on an aircraft mounted SAR sensor. While GMTI modes can be operated at any squint angle, SAR operation typically requires a squint angle between 45° and 135°

5.2 Knowledge of road systems

One way to break the azimuth ambiguity problem is through knowledge of road systems in the scene of interest. There are several commercially available databases of road location from companies specializing in geographic information systems data. These include NAVTEQ and Tele Atlas. Road data from these system are typically stored as vectors positioned along the centerline of the road position. The ability to register the SAR scene with the road database will also add an error source. It is possible to register the SAR scene to within several meters.

The knowledge that the moving target is on a road can be used to focus a target. However, this does require an assumption that the moving target is actually on a road and that the road is in a database that is accessible by the radar system. Further assumptions can be made based on knowledge of the specific road system and local traffic patterns. For instance, traffic on a two lane highway in the United States is very likely to be traveling along the center of the right lane. For the purposes of this example it is assumed that the vehicle is on the road assumptions are not made about the specific location on the road. A typical highway traffic lane in the United States is 3.7m wide [20]. This means that given the knowledge that a vehicle is driving on a two lane road the probability density function of target position in the dimension orthogonal to the road is a uniform distribution 7.4m wide (Fig. 5.5 and 5.6). Knowledge that the target is on the road does not help place the target along the length of the road. The ambiguity function of a SAR radar system will

depend on the chirp, but a typical PDF of a moving target position given its detection in a SAR scene is a gaussian distribution in range extending the entire length of the scene in azimuth (Fig. 5.4).

The ability to use road knowledge to determine target position depends on the aspect angle of the road and the flight path. If the road and the radar flight patch are orthogonal then the position uncertainty of the target will be low (Fig. 5.7). However, as the road orientation moves further away from becoming orthogonal with the flight path there is a problem with GDOP and the position uncertainty of the target increases (Fig. 5.8).

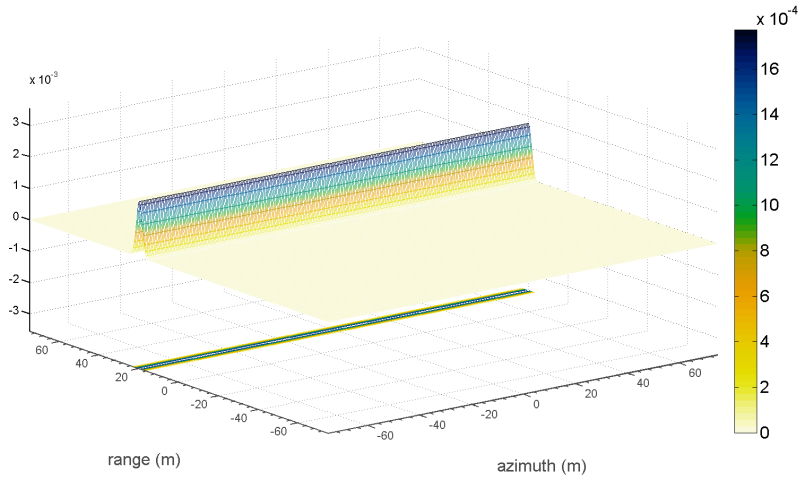

Figure 5.4: Probability density function of a moving target with a single radar phase center - azimuth position is unknown as the target range velocity has caused a shift in the azimuth position of the target energy.

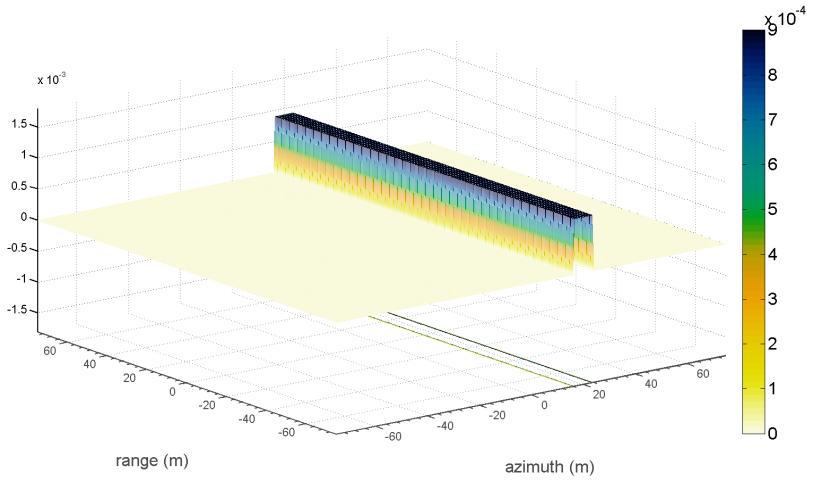

Figure 5.5: An example of a probability density function from a road positioned along azimuth. This road is known as example road one. The probability is characterized by a uniform distribution as the target center is assumed to be anywhere within two lanes of traffic.

5.3 Target knowledge

If a moving target has well defined micro-Doppler this can be used in the focusing process. Micro-Doppler can be observed in partially focused moving targets. One method of obtaining micro-Doppler to aid in focusing is the application of the MITRE keystone method to a target followed by an autofocus technique. Micro-Doppler caused by wheel rotation is dependent on vehicle velocity. The SAR images of the pickup truck formed from the simulated Ka-Band SAR data show this clearly. The separation of the points on the two sets of micro-Doppler varies as expected with the velocity of truck (Fig 5.9).

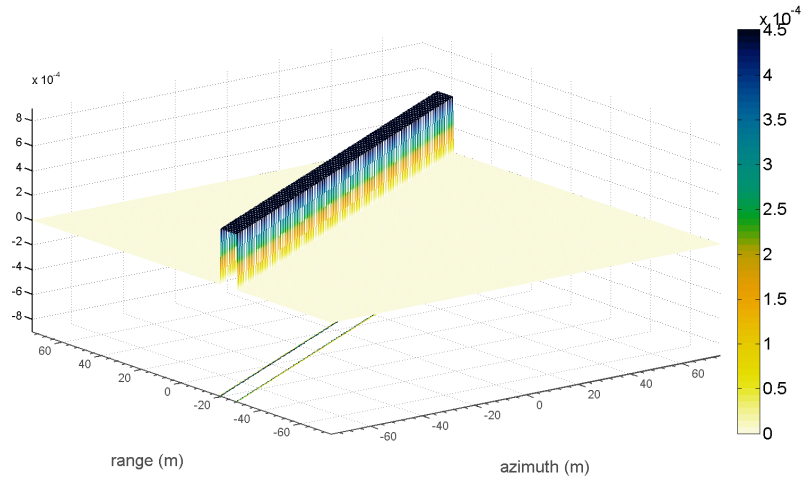

Figure 5.6: An example of a probability density function from a road that runs at thirty degrees from the flight path of the radar. This road is known as example road two. The probability is characterized by a uniform distribution as the target center is assumed to be anywhere within two lanes of traffic.

For vehicles where the micro-Doppler response is well known it should be possible to infer other information about the target from its micro-Doppler. The two sets of micro-Doppler from the pickup truck seem to be caused by wheel rotation. It appears that the separation of the two sets of micro-Doppler thus corresponds to the range component of the wheel base in the slant plane (Fig. 5.10). If the length of the wheel base is known this is sufficient information to determine the target orientation. In addition, the orientation of points on the two sets of micro-Doppler seems to correspond to the orientation of the vehicle (Fig. 5.10).

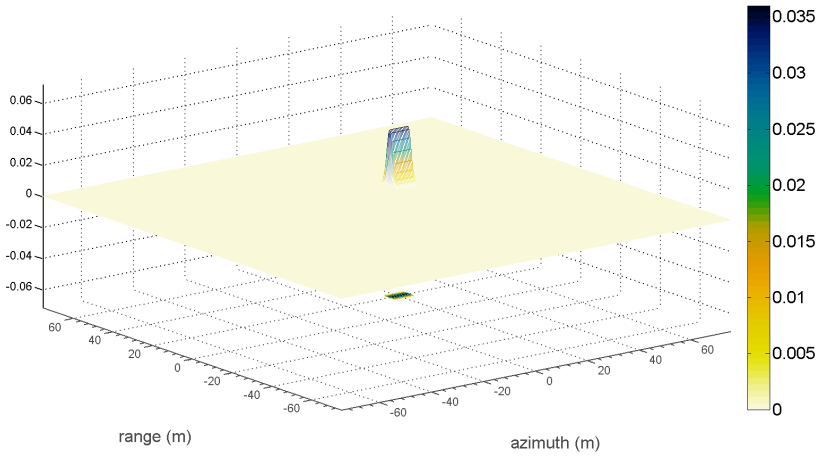

Figure 5.7: A probability density function of the position of a moving target obtained by direct sensing with a radar with *a priori* knowledge that the target is on the example road one.

5.4 A fully processed target

Here a point target is processed using knowledge that the target was traveling along a road whose centerline runs 20m away from the scene center in azimuth (Fig. 5.7). The target was simulated with motion parameters that would correspond to a target moving along this road: -1 m/s (2.2 mi/h) of azimuth velocity, 17 m/s (38 mi/h) of range velocity, and -0.05 m/s^2 (403 mi/h^2) of range acceleration. The target was placed 24m in azimuth from the scene center. The signal to clutter ratio for the entire scene is -20dB. The target was processed with the assumption that its azimuth position was 20m from the scene center. The 4m of position error combines several meters of registration error with a reasonable amount of uncertainty in vehicle placement

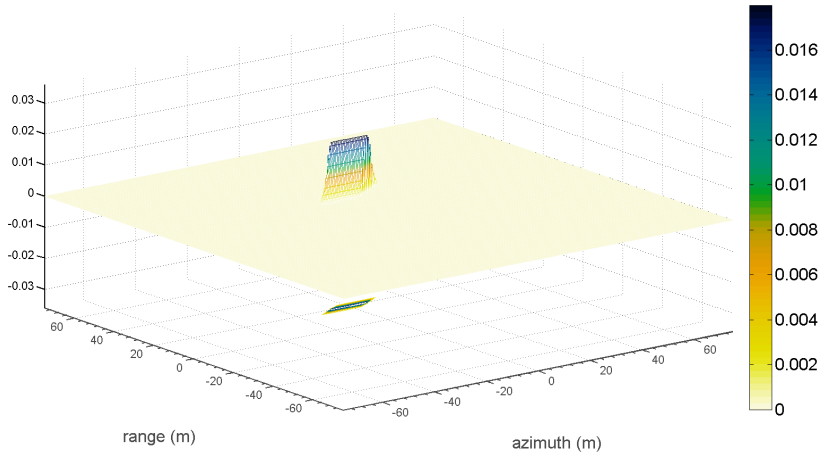

Figure 5.8: A probability density function of the position of a moving target obtained by direct sensing with a radar with *a priori* knowledge that the target is on the example road two.

on the road. This range velocity was sufficient to alias the target completely back into the endo-clutter region of the scene. The target energy is spread out in the unfocused scene to the extent that the target is not visible over the clutter (Fig. 5.11 and 5.12). However, the detection algorithm easily identifies the target (Fig. 5.13 and 5.14). The focusing algorithm determines the azimuth velocity of the moving target to be -1.473 m/s, the range velocity of the target to be 17.03 m/s, and the range acceleration to be -0.033 m/s^2. The target is successfully located and focused (Fig. 5.15 and 5.16).

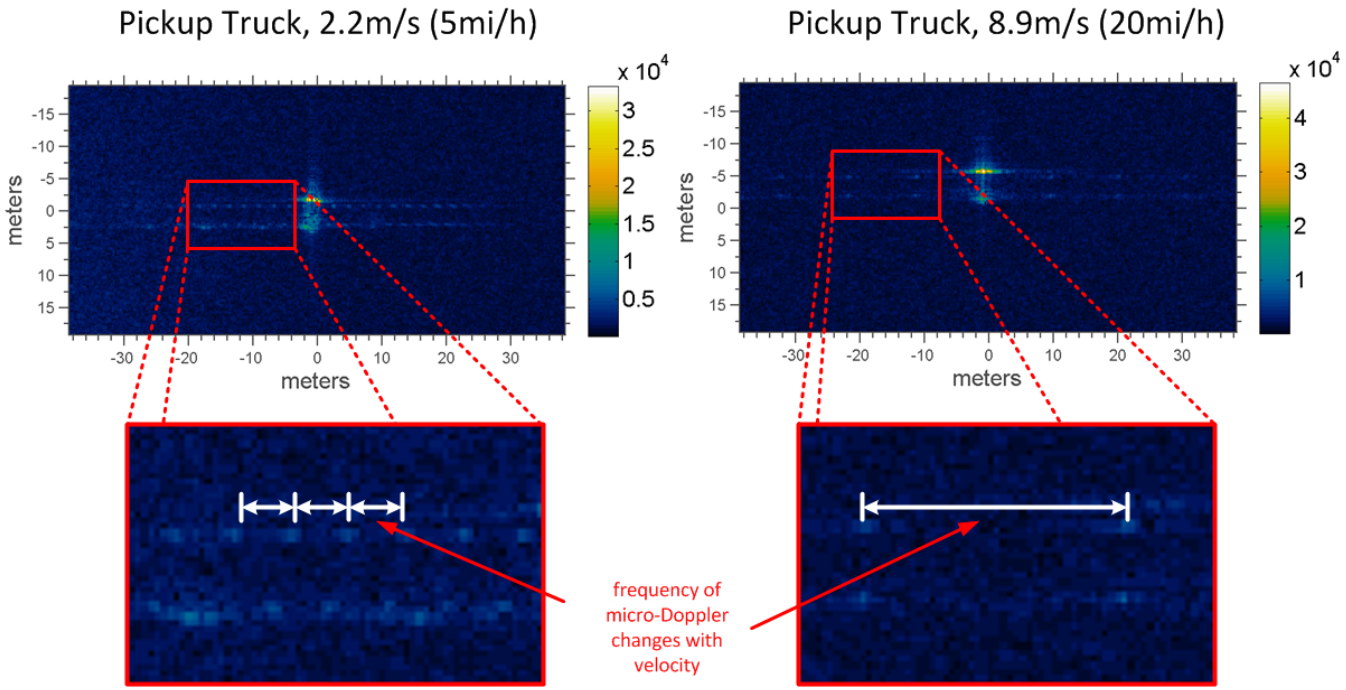

Figure 5.9: The frequency of micro-Doppler is dependent on vehicle velocity.

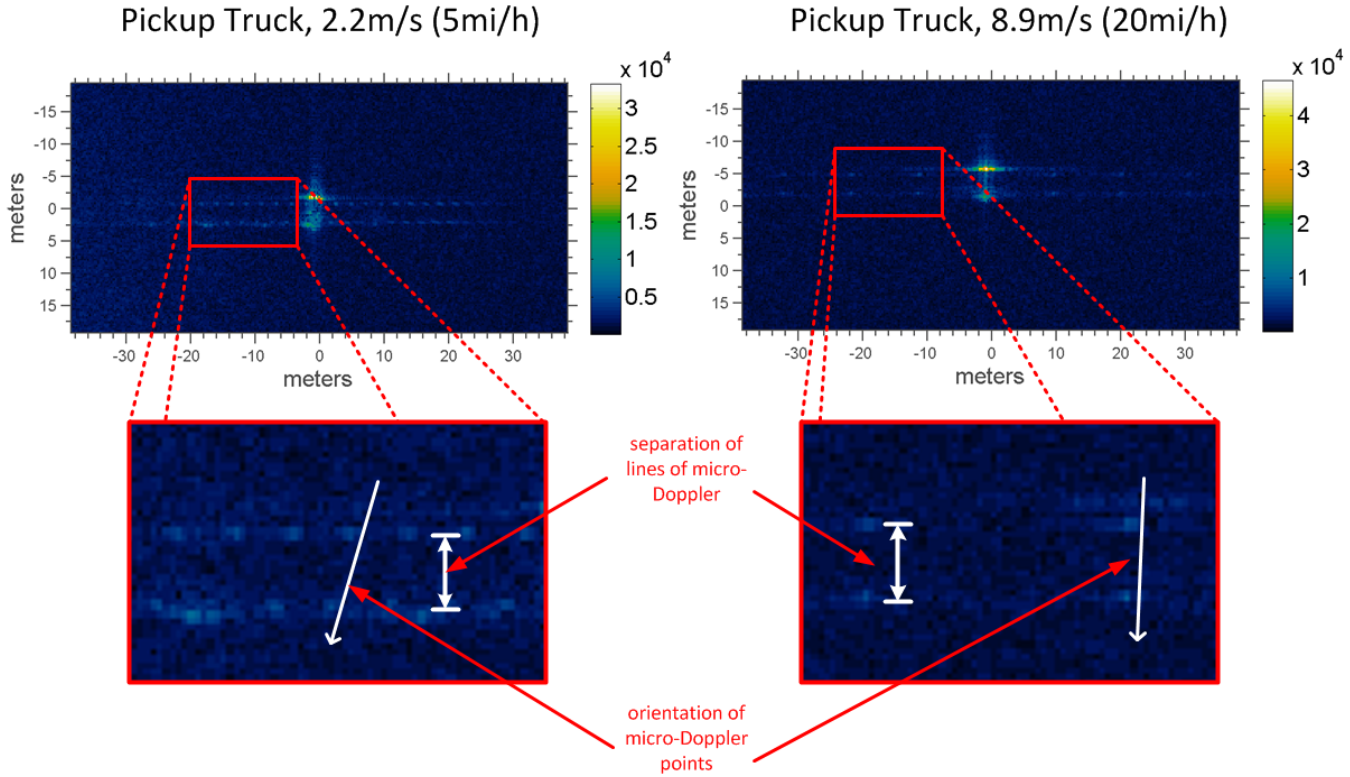

Figure 5.10: There are two sets of micro-Doppler from the truck that appear to correspond to the two axles and sets of wheels. This can be used to determine vehicle orientation.

5.5 Conclusion

This chapter reviewed using *a priori* knowledge about a SAR scene to aid in focusing. The primary focus was in using knowledge to solve the azimuth position uncertainty problem. However, knowledge about the target can also be used to aid in focusing through determining the orientation of the target. Micro-doppler was shown to be useful in providing information about target velocity and orientation, but to fully exploit the information contained in micro-Doppler requires knowledge of the target (wheel diameter, wheelbase length, etc). The shadow of a moving target can also be used to determine the true azimuth position of the target. This was not demonstrated here due to a lack of data - the SAR simulator used does simulate shadowing. The next chapter summarizes the results of this thesis and reviews future directions for research.

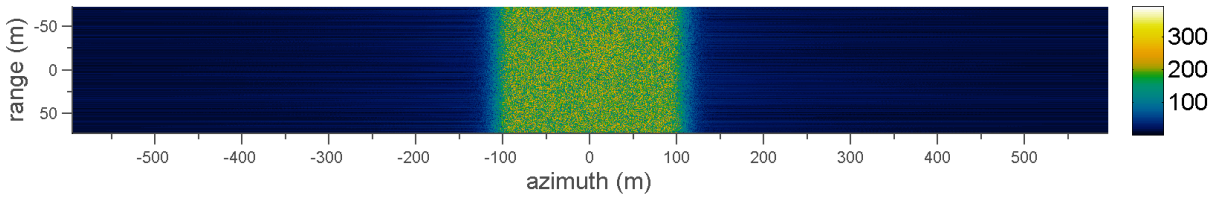

Figure 5.11: The full polar formatted SAR scene. The moving target is aliased and not visible above the clutter. The image is displayed as the square root of magnitude.

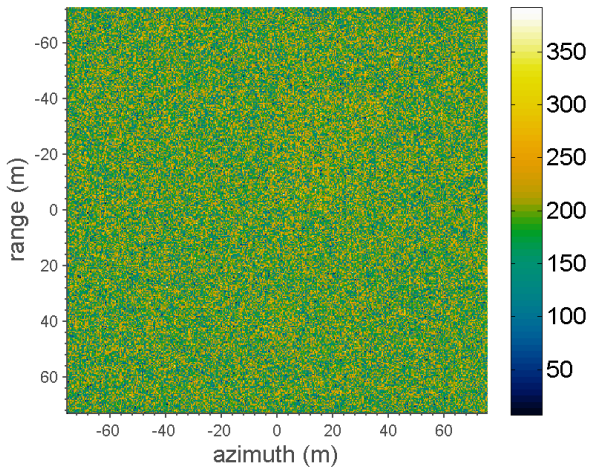

Figure 5.12: The endo-clutter region of the polar formatted SAR scene. The moving target is aliased and not visible above the clutter. The image is displayed as the square root of magnitude.

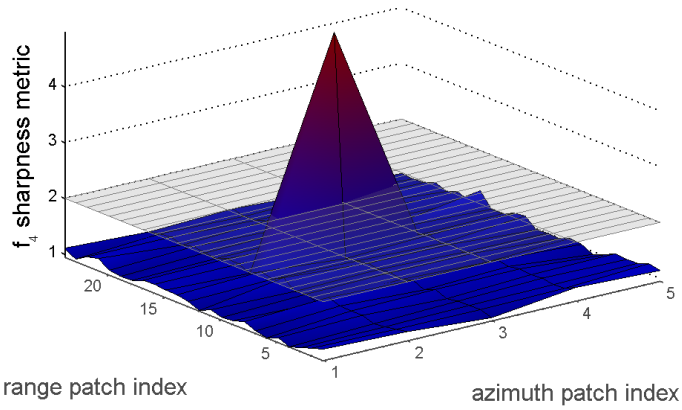

Figure 5.13: Detection results showing the detected endo-clutter target.

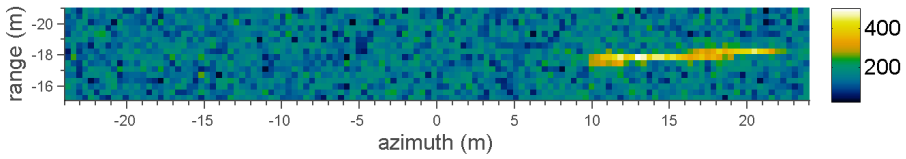

Figure 5.14: A detected moving target located 24m in range from the scene center moving at 17 m/s in range and -1 m/s in azimuth with -0.05 m/s^2 range acceleration.

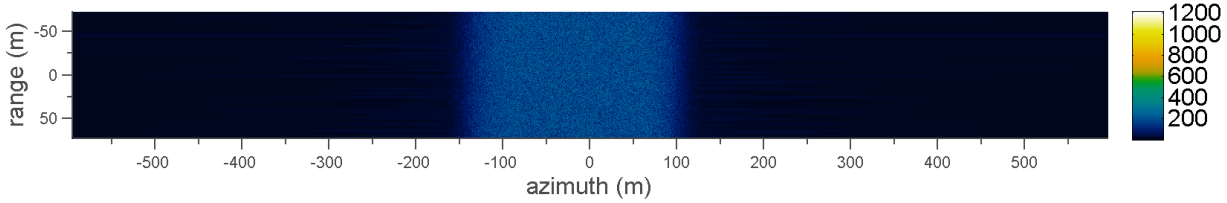

Figure 5.15: The full polar formatted SAR scene. The moving target is focused, however the clutter is now aliased. The image is displayed as the square root of magnitude.

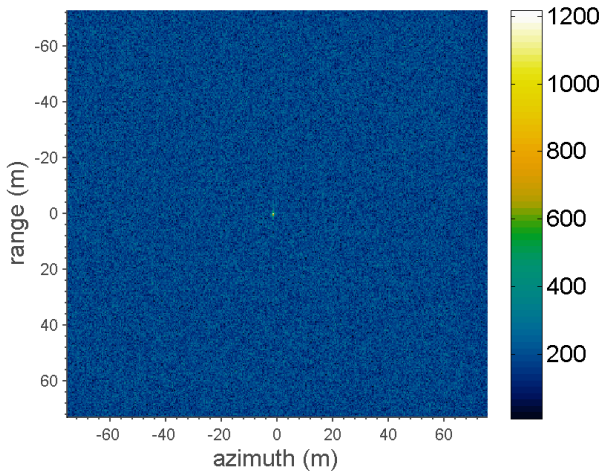

Figure 5.16: The endo-clutter region of the polar formatted SAR scene. The moving target is focused, however the clutter is now aliased. The image is displayed as the square root of magnitude.

Chapter 6

Summary and Future Work

This thesis first developed a mathematical model for motion induced errors in SAR images. Next, a novel method of processing moving targets in a SAR scene was presented, but was dependent on the use of multiple phase centers to detect and locate a moving target. A method to detect moving phase targets in a SAR image formed with data from a single phase center was presented. Finally, the use of knowledge about the scene or target to aid in target focusing was discussed.

There is a great deal more work that can be done to process moving targets in a single phase center. With multiple phase center systems clutter can be canceled using displaced phase center antenna or space time adaptive processing. While the same level of cancellation cannot be performed with data from a single phase center, it should be possible to provide some level of clutter cancellation. One possible method would be to use linear predictive coding to whiten the clutter.

The development of this method benefited greatly from access to good data. In the literature many techniques are demonstrated using synthetic data. There are a number of papers where moving targets are synthesized from sta-

tionary MSTAR targets and then embedded onto real SAR scenes. In some cases the SAR scenes are reconstructed from magnitude images with synthesized phase. While this is a testament to the resourcefulness of researchers, it is far from ideal. It is possible that the method described in chapter 3 could have been developed fully without access to data from the experimental Ka-band system, but having access to that data certainly helped. Further application and refinement of this technique on other real data sources will certainly be beneficial. A future experiment is being planned with high resolution strap down inertial measurement systems being placed on the moving targets.

Ideally, more forms of motion error should be considered. Target are not rigid bodies. Realistic targets flex and are composed of parts (suspensions and wheels among others) that may move independently. The presence of micro-Doppler in our focused images underscores this issue. For longer integration times, motion error induced by target rotation will become problematic. The real experimental Ka-band data used in this thesis was collected with the express purpose of developing algorithms to track and focus moving targets, and the duration of the coherent processing interval used was approximately 1.25 s. This is not out of line with other SAR-GMTI research - Fienup used example data covering just 0.472 seconds [18] - but testing on collections with longer integration times may prove useful in extending the technique.

One of the most exciting findings from this work is the quality of the micro-Doppler returns on the focused Ka-band targets. It would be interesting to see how micro-Doppler returns from various ground vehicles differ, and if

there are any characteristics of micro-Doppler that remain constant across vehicle types.

In chapter 3 the periodic variation in vehicle acceleration was reviewed and it was stated that this may be caused by the resonant frequency of the ground vehicle. It is hoped that this can be substantiated with further research using vehicles with strap down inertial measurements systems. The ability to remotely measure the resonant frequency of a ground vehicle would be very useful in target tracking.

Appendices

Appendix A

Return from a Point Target

SAR phase history data is composed of the summed returns from many individual scatterers. A SAR resolution cell will be composed of many elemental scatterers that each contribute to the final intensity and phase values for a pixel. Similarly, a SAR target will be composed of many elemental scatterers that contribute to its RF return. Here the return from a single point target scatterer is reviewed.

Transmitted Pulse High resolution in range requires large signal bandwidth. In SAR systems this is typically achieved through the use of a chirped pulse, and this is the case considered here. The radar transmits a linear-FM modulated chirped pulse defined as

$$w(t) = \Pi(t) \exp(j\Phi(t)) \tag{A.1}$$

where $\Pi(t)$ is the rectangular function

$$\Pi(t) = rect\left(\frac{t}{T}\right) = \begin{cases} 0, & \text{if } |t/T| > 1/2 \\ 1, & \text{if } |t/T| \leq 1/2 \end{cases} \tag{A.2}$$

And phase $\Phi(t)$

$$\Phi(t) = \omega_0 t + \frac{1}{2}\gamma t^2 + \phi \tag{A.3}$$

Received Pulse The radar return received by the radar is a scaled copy of the transmitted chirped pulse time shifted by the round trip time from the transmitter to the target and back to the receiver. In many SAR systems the transmitter and receiver are collocated. Thus, the time delay is given by $2r/c$ where r is the range to the target from the phase center of the antenna and c is the speed of light.

However, to ensure that all derivations are appropriate for situations where the transmitter and receiver are not collocated, here d is used to represent the round trip distance, and d/c to represent the round trip time delay. Thus the received signal is given by:

$$w_{rx}\left(t-\frac{d}{c}\right)=C\Pi\left(t-\frac{d}{c}\right)\exp\left[j\Phi\left(t-\frac{d}{c}\right)\right] \tag{A.4}$$

where:

$$\begin{aligned}\Phi\left(t-\frac{d}{c}\right) &= \omega_0\left(t-\frac{d}{c}\right)+\frac{1}{2}\gamma\left(t-\frac{d}{c}\right)^2+\phi\\ &= \omega_0 t-\omega_0\left(\frac{d}{c}\right)+\frac{1}{2}\left(t^2-\frac{2dt}{c}+\frac{d^2}{c^2}\right)+\phi\\ &= \left[\omega_0 t+\frac{1}{2}\gamma t^2+\phi\right]-\omega_0\frac{d}{c}-\gamma\frac{d}{c}t+\frac{1}{2}\frac{d^2}{c^2}\\ &= \Phi(t)-\frac{d}{c}\left[\omega_0+\gamma\left(t-\frac{1}{2}\frac{d}{c}\right)\right]\end{aligned} \tag{A.5}$$

When the transmitter and receiver are collocated $d=2r$ and the received phase is

$$\Phi_r\left(t-\frac{2r}{c}\right)=\Phi(t)-\frac{2r}{c}\left[\omega_0+\gamma\left(t-\frac{r}{c}\right)\right] \tag{A.6}$$

Motion Compensation to a Point For polar format processing of spotlight mode radar data, the data is often deramped by demodulating the received signal with a reference function based on the return from the scene center point. The phase of this deramped signal is then the original return minus the phase component from the scene center

$$\begin{aligned}
\Phi_{deramp}(t) &= \Phi_r(t) - \Phi_0(t) \\
&= \left[\omega_0\left(t-\frac{d}{c}\right)+\alpha\left(t-\frac{d}{c}\right)^2\right] - \left[\omega_0\left(t-\frac{d_0}{c}\right)+\alpha\left(t-\frac{d_0}{c}\right)^2\right] \\
&= -\frac{\omega_0}{c}(d-d_0) - 2\frac{\alpha t}{c}(d-d_0) + \frac{\alpha}{c^2}\left(d^2-d_0^2\right) \\
&= -\frac{1}{c}(\omega_0+2\alpha t)(d-d_0) + \frac{\alpha}{c^2}\left(d^2-d_0^2\right) \\
&= -\frac{1}{c}(\omega_0+2\alpha t)(d-d_0) + \frac{\alpha}{c^2}\left[(d-d_0)^2+2d_0(d-d_0)\right] \\
&= -\frac{1}{c}\left[\omega_0+2\alpha\left(t-\frac{2d_0}{c}\right)\right](d-d_0) + \frac{\alpha}{c^2}(d-d_0)^2 \qquad \text{(A.7)}
\end{aligned}$$

where d_0 is the round trip distance to the scene center. When the transmitter and receiver are collocated $d = 2r$ and the deramped phase is:

$$\Phi_{deramp}(t) = -\frac{2}{c}\left[\omega_0+2\alpha\left(t-\frac{2r_0}{c}\right)\right](r-r_0) + \frac{4\alpha}{c^2}(r-r_0)^2 \qquad \text{(A.8)}$$

Approximation of Motion Compensated Phase Return By letting $\Delta_d = d - d_0$ and defining the wavenumber $k = 2\omega/c$ (A.7) can be refactored conveniently as:

$$
\begin{aligned}
\Phi_{deramp}(t) &= -\frac{1}{c}\left[\omega_0 + 2\alpha\left(t - \frac{2d_0}{c}\right)\right](d - d_0) + \frac{\alpha}{c^2}(d - d_0)^2 \\
&= -\frac{1}{c}\left[\omega_0 + 2\alpha t - \frac{4\alpha d_0}{c}\right](d - d_0) + \frac{\alpha}{c^2}(d - d_0)^2 \\
&= -\frac{1}{c}\left[\omega_0 + 2\alpha t\right](d - d_0) + \frac{4\alpha d_0}{c^2} + \frac{\alpha}{c^2}(d - d_0)^2 \\
&= -k\Delta_d + \underbrace{\frac{\alpha}{c^2}\left[4d_0 + \Delta_d\right]\Delta_d}_{\text{Residual Phase Term}}
\end{aligned} \tag{A.9}
$$

As $c^2 \gg \alpha$ the residual phase term can be dropped. Similarly, $\Delta_r = r - r_0$ can be defined to refactor (A.8) as:

$$
\Phi_{deramp}(t) = -2k\Delta_r + \underbrace{\frac{4\alpha}{c^2}\left[2r_0 + \Delta_r\right]\Delta_r}_{\text{Residual Phase Term}} \tag{A.10}
$$

Two dimensional returns Target and platform motion over the course of the aperture, and thus between pulses, is significant. Thus the the position of a moving target and phase centers of the antennas vary with slow time τ. This relative motion is critical to the SAR process as it provides fine resolution in azimuth. However, the unknown motion of the target and any error in positioning information of the antenna phase center also causes errors in the final formed image. The target's 2D phase history is given as:

$$
\begin{aligned}
s(\tau, t) &= C \exp\left\{ j \left[\omega_0 \left(t - \frac{d(\tau)}{c} \right) + \gamma \left(t - \frac{d(\tau)}{c} \right)^2 \right] \right\} \qquad \text{(A.11)} \\
&= C \exp\left\{ j\omega_0 \left(t - \frac{d(\tau)}{c} \right) \right\} \exp\left\{ j\gamma \left(t - \frac{d(\tau)}{c} \right)^2 \right\}
\end{aligned}
$$

Bibliography

[1] S. Barbarossa. Detection and imaging of moving objects with synthetic aperture radar. 1. optimal detection and parameter estimation theory. *Radar and Signal Processing, IEE Proceedings F*, 139(1):79–88, 1992.

[2] S. Barbarossa and A. Farina. Detection and imaging of moving objects with synthetic aperture radar. 2. joint time-frequency analysis by Wigner-Ville distribution. *Radar and Signal Processing, IEE Proceedings F*, 139(1):89–97, 1992.

[3] S. Barbarossa and A. Farina. Space-time-frequency processing of synthetic aperture radar signals. *Aerospace and Electronic Systems, IEEE Transactions on*, 30(2):341–358, 1994.

[4] G. A. Bendor and T. W. Gedra. Single-pass fine-resolution sar autofocus. *NAECON 1983; Proceedings of the National Aerospace and Electronics Conference, Dayton, OH; United States*, pages 482–488, 1983.

[5] F. Berizzi and G. Corsini. Autofocusing of inverse synthetic aperture radar images using contrast optimization. *Aerospace and Electronic Systems, IEEE Transactions on*, 32(3):1185–1191, 1996.

[6] T.M. Calloway and G.W. Donohoe. Subaperture autofocus for synthetic aperture radar. *Aerospace and Electronic Systems, IEEE Transactions*

on, 30(2):617–621, 1994.

[7] Walter G. Carrara, Ron S. Goodman, and Ronald M. Majewski. *Spotlight Synthetic Aperture Radar: Signal Processing Algorithms*. Artech House, 1995.

[8] V.C. Chen, R. Lipps, and M. Bottoms. Radar imaging of ground moving targets. In *Radar Conference, 2001. Proceedings of the 2001 IEEE*, pages 426–431, 2001.

[9] Victor C. Chen and Hao Ling. *Time-frequency transforms for radar imaging and signal analysis*. Artech House, 2002.

[10] Leon Cohen. *Time-frequency Analysis*. Prentice Hall PTR, 1995.

[11] Ian G. Cumming and Frank H. Wong. *Digital Processing of Synthetic Aperture Radar Data*. Artech House, Massachusetts, 1st edition, 2005.

[12] J.M.B. Dias and P.A.C. Marques. Multiple moving target detection and trajectory estimation using a single SAR sensor. *Aerospace and Electronic Systems, IEEE Transactions on*, 39(2):604–624, 2003.

[13] Armin W Doerry. Clutter in the GMTI Range-Velocity map. Technical report, Sandia National Laboratories, April 2009.

[14] Armin W Doerry. Performance limits for exo-clutter ground moving target indicator (GMTI) radar. Technical report, Sandia National Laboratories, September 2009.

[15] Armin W. Doerry. Personal correspondence, October 2010.

[16] J.N. Entzminger, C.A. Fowler, and W.J. Kenneally. JointSTARS and GMTI: past, present and future. *Aerospace and Electronic Systems, IEEE Transactions on*, 35(2):748–761, 1999.

[17] J.R. Fienup. Phase error correction by shear averaging. *Signal Recovery and Synthesis III*, pages 134–137, 1989.

[18] J.R. Fienup. Detecting moving targets in SAR imagery by focusing. *Aerospace and Electronic Systems, IEEE Transactions on*, 37(3):794–809, 2001.

[19] C.A. Fowler. The standoff observation of enemy ground forces from project peek to JointSTARS-A prolusion. *Aerospace and Electronic Systems Magazine, IEEE*, 12(6):3–17, 1997.

[20] *Highway Capacity Manual 2000*, 2000.

[21] J.C. Henry. The lincoln laboratory 35 GHz airborne SAR imaging radar system. In *Telesystems Conference, 1991. Proceedings. Vol.1., NTC '91., National*, pages 353–358, 1991.

[22] IEEE standard radar definitions, 1990.

[23] Eugene F. Greneker III, Jonathan L. Geisheimer, David Asbell, Robert Trebits, and James L. Kurtz. Extraction of micro-Doppler data from

vehicle targets at x-band frequencies. In *Radar Sensor Technology VI*, volume 4374, pages 1–9, Orlando, FL, USA, 2001. SPIE.

[24] D.L. Jones and T.W. Parks. A resolution comparison of several time-frequency representations. In *Acoustics, Speech, and Signal Processing, 1989. ICASSP-89., 1989 International Conference on*, pages 2222–2225 vol.4, 1989.

[25] Steven M. Kay. *Fundamentals of statistical signal processing.* PTR Prentice-Hall, 1993.

[26] M. Kirscht. Detection and imaging of arbitrarily moving targets with single-channel SAR. *Radar, Sonar and Navigation, IEE Proceedings* -, 150(1):7–11, 2003.

[27] Nadav Levanon. *Radar Principles.* John Wiley & Sons, New York, 1st edition, 1988.

[28] Paulo A. C Marques, Jose M. B Dias, and R. Conselheiro Emdio Navarro. Optimal detection and imaging of moving objects with unknown velocity. *In Proc. of the 3rd European Conference on Synthetic Aperture Radar, EUSAR 2000*, 2000:561—564, 2000.

[29] M. J. Minardi. Ground moving target detection and tracking based on generalized SAR processing and change detection (Invited paper). In *Proceedings of SPIE*, pages 156–165, Orlando, FL, USA, 2005.

[30] Daniel P. Morrison, Jr. Eckert, and Frank J. Shields. Studies of advanced detection technology sensor (ADTS) data. In Dominick A. Giglio, editor, *Algorithms for Synthetic Aperture Radar Imagery*, volume 2230, pages 370–378, Orlando, FL, USA, June 1994. SPIE.

[31] Richard A. Muller and Andrew Buffington. Real-time correction of atmospherically degraded telescope images through image sharpening. *Journal of the Optical Society of America*, 64(9):1200, 1974.

[32] G. Palubinskas and H. Runge. Radar signatures of a passenger car. *Geoscience and Remote Sensing Letters, IEEE*, 4(4):644–648, 2007.

[33] G. Palubinskas, H. Runge, and P. Reinartz. Radar signatures of road vehicles. In *Geoscience and Remote Sensing Symposium, 2004. IGARSS '04. Proceedings. 2004 IEEE International*, volume 2, pages 1498–1501 vol.2, 2004.

[34] R.P. Perry, R.C. DiPietro, and R.L. Fante. SAR imaging of moving targets. *Aerospace and Electronic Systems, IEEE Transactions on*, 35(1):188–200, 1999.

[35] R.K. Raney. Synthetic aperture imaging radar and moving targets. *Aerospace and Electronic Systems, IEEE Transactions on*, AES-7(3):499–505, 1971.

[36] M. Ruegg, M. Hagelen, E. Meier, and D. Nuesch. Moving target indication with dual frequency millimeter wave SAR. In *Radar, 2006 IEEE*

Conference on, page 8 pp., 2006.

[37] P. K. Sanyal, D. M. Zasada, and R. P. Perry. Detecting and georegistering moving ground targets in airborne quick SAR via keystoning and multiple-phase center interferometry. *EURASIP J. Adv. Signal Process*, 2008:1–11, 2008.

[38] Samuel M. Sherman. *Monopulse principles and techniques*. Artech House, December 1984.

[39] M. Soumekh. Reconnaissance with ultra wideband UHF synthetic aperture radar. *Signal Processing Magazine, IEEE*, 12(4):21–40, 1995.

[40] M. Soumekh. Moving target detection and imaging using an x band along-track monopulse SAR. *Aerospace and Electronic Systems, IEEE Transactions on*, 38(1):315–333, 2002.

[41] Mehrdad Soumekh. *Fourier Array Imaging*. PTR Prentice-Hall, 1994.

[42] Mehrdad Soumekh. *Synthetic Aperture Radar Signal Processing with MATLAB Algorithms*. J. Wiley, 1999.

[43] B.D. Steinberg. Microwave imaging of aircraft. *Proceedings of the IEEE*, 76(12):1578–1592, 1988.

[44] P. Swerling. Probability of detection for fluctuating targets. *Information Theory, IRE Transactions on*, 6(2):269–308, 1960.

[45] Peter Swerling. Probability of detection for flucuating targets. Technical report, The Rand Corporation, Santa Monica, California, 1954.

[46] Peter Swerling. More on detection of fluctuating targets. Technical report, The Rand Corporation, Santa Monica, California, 1965.

[47] Paul Thompson, Daniel E. Wahl, Paul H. Eichel, Dennis C. Ghiglia, and Charles V. Jakowatz. *Spotlight-Mode Synthetic Aperture Radar: A Signal Processing Approach*. Kluwer Academic Publishers, 1996.

[48] S. I. Tsunoda, F. Pace, J. Stence, M. Woodring, W. H. Hensley, A. W. Doerry, and B. C. Walker. *Lynx: A high-resolution synthetic aperture radar*. General Atomics and Sandia National Laboratories. Available as `http://www.sandia.gov/RADAR/files/spie_lynx.pdf`.

[49] D.E. Wahl, P.H. Eichel, D.C. Ghiglia, and C.V. Jakowatz. Phase gradient autofocus-a robust tool for high resolution SAR phase correction. *Aerospace and Electronic Systems, IEEE Transactions on*, 30(3):827–835, 1994.

[50] S.A. Werness, M.A. Stuff, and J.R. Fienup. Two-dimensional imaging of moving targets in SAR data. In *Signals, Systems and Computers, 1990. 1990 Conference Record Twenty-Fourth Asilomar Conference on*, volume 1, page 16, 1990.

[51] S.A.S. Werness, W.G. Carrara, L.S. Joyce, and D.B. Franczak. Moving target imaging algorithm for SAR data. *Aerospace and Electronic*

Systems, IEEE Transactions on, 26(1):57–67, 1990.

[52] R. Williams. Automotive active suspensions part 1: basic principles. *Proceedings of the Institution of Mechanical Engineers, Part D: Journal of Automobile Engineering*, 211(6):415–426, 1997.

[53] Li Xi, Liu Guosui, and Jinlin Ni. Autofocusing of ISAR images based on entropy minimization. *Aerospace and Electronic Systems, IEEE Transactions on*, 35(4):1240–1252, 1999.

[54] H. Yang and M. Soumekh. Motion estimation and compensation in SAR/ISAR imaging. In *Acoustics, Speech, and Signal Processing, 1992. ICASSP-92., 1992 IEEE International Conference on*, volume 3, pages 17–20 vol.3, 1992.

[55] Jijie Zhu. Calculation of geometric dilution of precision. *Aerospace and Electronic Systems, IEEE Transactions on*, 28(3):893–895, 1992.

Vita

Richard Maxwell Naething was born in Oklahoma, but as the son of a career military officer spent his childhood living in numerous cities across three continents. He graduated with a Bachelor of Science degree from Rensselaer Polytechnic Institute in Troy, NY in May 2004. In the fall of 2004 he started his graduate studies in the Electrical Engineering department of The University of Texas at Austin, receiving the Masters of Science in Engineering degree in Electrical Engineering in May 2006. He is a senior member of the technical staff works at Sandia National Laboratories. Richard lives with his wife and their dog in Albuquerque, NM.

Permanent address: richard.naething@sandia.gov

This dissertation was typeset with LaTeX[†] by the author.

[†]LaTeX is a document preparation system developed by Leslie Lamport as a special version of Donald Knuth's TeX Program.